

MEASUREMENT OF THE RATIO OF BRANCHING RATIOS $\frac{\mathcal{B}(B^+ \rightarrow J/\psi\pi^+)}{\mathcal{B}(B^+ \rightarrow J/\psi K^+)}$ AND

SEARCH FOR B_C^+

Scott D. Metzler

A DISSERTATION

in

PHYSICS AND ASTRONOMY

Presented to the Graduate Faculty of the University of Pennsylvania in Partial

Fulfillment of the Requirements for the Degree of Doctor of Philosophy

1996

Ron J. Hellebust
Supervisor of Dissertation

Ron J. Hellebust
Graduate Group Chairman

Y1996-00001
AUGUST 1996
2000 AD

MATH PHYSICS | QC 001 | 1996 | KCL LIBS

ACKNOWLEDGMENTS

In the process of completing a long endeavor, there are many to thank for their contributions. All cannot be recognized, but I will attempt to address those most significant.

First, I would like to thank Professor Nigel Lockyer for his guidance and availability. His direct involvement and supervision greatly speeded progress and improved both the quality of work and the work environment. As a mentor, naturally, he was most effective when coffee was involved.

I would like to thank my advisor, Professor Robert Hollebeek. His support and guidance have been valuable assets. My interest in and experience with high performance computing have been a direct result of his expertise in the field.

Two postdocs were very helpful during the course of this work. I thank Dr. Joel Heinrich and Dr. Fumi Ukegawa. Both were eager to help, explain, discuss and critique ideas and papers.

I would like to thank my fellow CDF graduate students for their friendship, professional assistance and the fond memories. Thanks Julio González, Farrukh Azfar, Rick Wilkinson, Chris Holck, Owen Long and Gary Houk.

A separate category is reserved for fellow student and CDF colleague Brendan Bevensee, who has been a wonderful friend during the past several years. Most of the fond memories of graduate school will undoubtedly be connected with him. Thank

you for your encouragement and amusing antics.

The most influential and supportive person during the course of this graduate program has been my wife, Dianna. Thank you for your encouragement and understanding during the difficult times. I especially appreciate the many little things you have done to make my life easier and the balance you have brought.

I also wish to thank my parents, Charles and Barbara, and my sister, Kimberly. Thank you for the many meals and the other physical and emotional support during these years. It was nice to be near home during some of this time. Thank you for support and help through the years.

I thank God for the good friends I have made and the good times I have had during the completion of my degree.

ABSTRACT

MEASUREMENT OF THE RATIO OF BRANCHING RATIOS $\frac{\mathcal{B}(B^+ \rightarrow J/\psi\pi^+)}{\mathcal{B}(B^+ \rightarrow J/\psi K^+)}$ AND
SEARCH FOR B_c^+

Scott D. Metzler

Robert Hollebeek

This thesis reports on a measurement of the branching ratio of the Cabibbo-suppressed decay $B_u^+ \rightarrow J/\psi\pi^+$, where $J/\psi \rightarrow \mu^+\mu^-$. The data were collected by the Collider Detector at Fermilab during 1992-1995 and correspond to an integrated luminosity of 110 pb^{-1} in $\bar{p}p$ collisions at $\sqrt{s} = 1.8 \text{ TeV}$. A signal of 28^{+10}_{-9} events is observed and we determine the ratio of branching ratios $\mathcal{B}(B_u^+ \rightarrow J/\psi\pi^+)/\mathcal{B}(B_u^+ \rightarrow J/\psi K^+)$ to be $(5.0^{+1.9}_{-1.7} \pm 0.1)\%$, where the first uncertainties are statistical and the second are systematic. Using the world average value for $\mathcal{B}(B_u^+ \rightarrow J/\psi K^+)$, we calculate the branching ratio $\mathcal{B}(B_u^+ \rightarrow J/\psi\pi^+)$ to be $(5.0^{+2.1}_{-1.9}) \times 10^{-5}$. We also search for the decay $B_c^+ \rightarrow J/\psi\pi^+$ and report a 95% confidence level limit on $\sigma(B_c^+) \cdot \mathcal{B}(B_c^+ \rightarrow J/\psi\pi^+)/\sigma(B_u^+) \cdot \mathcal{B}(B_u^+ \rightarrow J/\psi K^+)$ as a function of the B_c^+ lifetime.

Contents

1	Introduction	1
1.1	Overview	1
1.2	B Production	2
1.3	B Decays	3
1.4	The CKM Matrix	5
1.5	Cabibbo-Suppressed Decay Modes	9
1.6	Factorization Hypothesis	11
1.7	B_c^+ Physics	15
1.8	Summary	17
2	Experimental Setup	18
2.1	Generation of Colliding Beams	18
2.2	Acceleration Procedure	19
2.3	The Collider Detector at Fermilab (CDF)	20
2.4	The Central Tracking Chamber (CTC)	20

2.5	Vertex Time Projection Chamber (VTX)	21
2.6	Silicon Vertex Detector (SVX and SVX')	21
2.7	Muon Chambers	26
2.7.1	Central Muon System (CMU)	29
2.7.2	Central Muon Upgrade (CMP)	29
2.7.3	Central Muon Extension (CMX)	31
2.7.4	Forward Muon System (FMU)	31
3	Data Sample	33
3.1	J/ψ Trigger	33
3.2	Offline Production	35
4	Tracking	36
4.1	CTC Tracking	36
4.2	SVX Tracking	37
5	J/ψ Reconstruction	39
5.1	Muon Identification and Selection	39
5.2	J/ψ Reconstruction	40
5.3	Mass Error Scale Factor	41
6	B Meson Reconstruction	43
6.1	Track Selection	43

6.2	B Selection	44
6.3	Mass Distributions	46
7	Measurement of the Ratio of Branching Ratios	49
7.1	Ratio of Branching Ratios Calculation	49
7.2	Maximum Likelihood Fit	50
7.3	Fitting Region	51
7.4	Likelihood Function	51
7.5	Fit Testing	53
7.6	Fit Results	56
7.7	Cross Checks	56
7.8	Relative Efficiency Determination	61
7.9	Decay-in-Flight	65
7.10	Ratio of Ratios Calculation	68
8	B_c^+ Reconstruction	71
8.1	Backgrounds	71
8.2	Techniques	72
8.3	$\pi^+ - \mu^+$ Angular Correlations	72
8.3.1	$B_c^+ \rightarrow J/\psi \pi^+$ Decay	72
8.3.2	J/ψ Decay	74

8.3.3	Optimization of Helicity Angle Selection	77
8.4	Standard Cuts	79
8.5	Associated K_s^0 Events	80
8.6	Limit Formulation	84
8.7	B_c^+ Width	86
8.8	B_c^+ Search Region	87
8.9	$B_u^+ \rightarrow J/\psi K^+$ Reference Signal	87
8.10	Relative Efficiency	88
8.11	Decay-in-Flight Correction	93
8.12	Limit Determination	93
9	Systematics	95
9.1	Systematics on r_{obs}	95
9.1.1	Cabibbo-suppressed Analysis	95
9.1.2	B_c^+ Search	97
9.2	Systematics on ϵ_{rel}	99
9.2.1	Cabibbo-suppressed Analysis	99
9.2.2	B_c^+ Search	100
9.3	Systematics on \mathcal{D} , the decay-in-flight correction	100
9.4	Total Systematic	101
9.5	Recalculation of the B_c^+ Limit	102

10 Conclusions	105
A Decay-in-Flight Correction Limits	107
B Asymmetric Fitting	114
C $\frac{dM_{J/\psi\pi^+}}{dM_{J/\psi K^+}}$ Determination	119
D Angular Correlation of π^+ and μ^+ from $B_c^+ \rightarrow J/\psi\pi^+$, $J/\psi \rightarrow \mu^+\mu^-$	121
Bibliography	126

List of Tables

1.1	B_c^+ width and lifetime predictions.	16
2.1	CTC wire configuration	22
2.2	Characteristics of the SVX and SVX' detectors.	26
4.1	SVX selection efficiency	38
7.1	Results of Monte Carlo testing.	54
7.2	Fit results.	56
7.3	Relative efficiency for B_c^+ .	64
7.4	Decay-in-flight correction vs. run number.	66
7.5	Decay-in-flight correction vs. $P_T(B)$.	67
8.1	Efficiencies for B_c^+ and B_u^+ .	90
9.1	Parabolic background fitting results.	96
9.2	Effect of mass uncertainty ratio error.	98
9.3	Data runs for decay-in-flight.	101

9.4 Summary of systematic errors.	102
---	-----

List of Figures

1.1	Feynmann graph of $\bar{b}b$ production from quark annihilation.	3
1.2	Feynmann graph of $\bar{b}b$ production from gluon interactions.	4
1.3	External W diagram.	5
1.4	Internal W diagram.	6
1.5	$B_u^+ \rightarrow J/\psi K^+$ Feynmann diagram.	7
1.6	$B_c^+ \rightarrow J/\psi \pi^+$ Feynmann diagram.	7
1.7	W^\pm intermediate vector boson coupling of quarks.	10
1.8	Fenmann diagram of $B_u^+ \rightarrow J/\psi K^+, J/\psi \pi^+$	11
1.9	B_u^+ two-body decay.	13
2.1	CTC view from endplate	23
2.2	SVX location within CDF detector.	24
2.3	Sketch of one of two SVX barrels.	25
2.4	Sketch of an SVX ladder.	27
2.5	Diagram of muon detector locations	28
2.6	CMU layout.	30

2.7	Cross-section of muon module.	31
5.1	Invariant mass distribution for dimuons.	41
5.2	Normalized mass distributions for dimuon events.	42
6.1	Two-dimensional diagram of the B meson's primary and secondary vertices	45
6.2	The $J/\psi K^+$ invariant mass distribution.	47
6.3	The $J/\psi \pi^+$ invariant mass distribution.	48
7.1	Results of Monte Carlo testing.	55
7.2	Fitted $J/\psi K^+$ mass distribution.	57
7.3	Scatter plot of $M_{J/\psi K^+}$ vs. $M_{J/\psi \pi^+}$	59
7.4	The $J/\psi \pi^+$ mass distribution with superimposed Monte Carlo.	60
7.5	Scatter plot of $J/\psi \pi^+$ mass vs. the third track's invariant mass.	62
7.6	Overall decay-in-flight correction for $J/\psi K^+$	69
7.7	Overall decay-in-flight correction for $J/\psi \pi^+$	70
8.1	$B_c^+ \rightarrow J/\psi \pi^+$ decay.	73
8.2	The $B_c^+ \rightarrow J/\psi \pi^+$ decay in the rest frame of the J/ψ	74
8.3	Feynmann diagram of $\bar{c}c$ QED annihilation.	75
8.4	The $J/\psi \pi^+$ invariant mass distribution for zero lifetime cuts.	81
8.5	The $J/\psi \pi^+$ invariant mass distribution for long-lived cuts.	82

8.6	The $\pi^+\pi^-$ invariant mass distribution.	83
8.7	The $J/\psi\pi^+$ invariant mass distribution with K_s^0 candidates.	84
8.8	The $B_u^+ \rightarrow J/\psi K^+$ mass distribution for reference events.	88
8.9	The 95% confidence level limit for B_c^+ production	94
9.1	The 95% confidence level limit on B_c^+ production with systematic uncertainties.	104
A.1	Two-dimensional view of track in CTC.	109
A.2	View of $x - z$ plane in CTC.	110
B.1	Asymmetric likelihood function.	118

Chapter 1

Introduction

1.1 Overview

The discovery of the $\Upsilon(1S)$ meson in 1977[1] has opened a fascinating frontier of particle physics. The $\Upsilon(1S)$ meson, the lowest bound state of a b -quark and a \bar{b} -quark, was first observed at Fermilab by the Columbia-Fermilab-Stony Brook Collaboration (CFS). CFS then found the next member of the Υ family, $\Upsilon(2S)$ [2]. The results were later confirmed at DORIS[3, 4, 5, 6] and CESR[7, 8].

The mass spectrum of the Υ family has been studied, revealing many resonances. The $\Upsilon(4S)$ resonance is the lowest-lying state above the $B\bar{B}$ -threshold, yielding upon decay two mesons with one b -quark or \bar{b} -quark each. The $\Upsilon(4S) \rightarrow B\bar{B}$ decay was first confirmed at CESR in 1983[9]. It has been a great source of B meson study.

Many properties of B mesons have been studied to check for consistency with the Standard Model. The charge, lifetime and weak coupling have been measured, along with other characteristics. Testing of B mesons continues, but at the present time

the Standard Model completely describes observations.

The future study of B physics is expected to shed light on some of the most fundamental questions of particle physics. The observation of charge-parity (CP) violation is expected in the B system. This is, perhaps, the most sought after discovery in particle physics today. The study of flavor mixing in neutral B mesons is one area to search for CP violation. In addition, B physics will provide an arena to improve the understanding of the quark potential model. The large mass of the b -quark makes non-relativistic quantum mechanics more accurate, particularly when more than one heavy quark is involved, such as the Υ and B_c^+ families. From these families accurate tests of the potential model can be made.

1.2 B Production

B mesons are produced in the hadronization of “bare” b -quarks. When a “bare” b -quark is produced, a quark-antiquark pair will materialize out of the background “sea” quarks to form a B meson, $b\bar{q}$, and another “bare” quark, q . This will continue until all quarks and antiquarks are “dressed” in a colorless quark-antiquark or three quark (antiquark) combination.

The b -quarks themselves are produced in $\bar{p}p$ collisions in two ways. Figure 1.1 shows the lowest-order strong annihilation of $\bar{q}q$, resulting in $\bar{b}b$ production. Figure 1.2 shows the leading order b -production from gluon interactions[10].

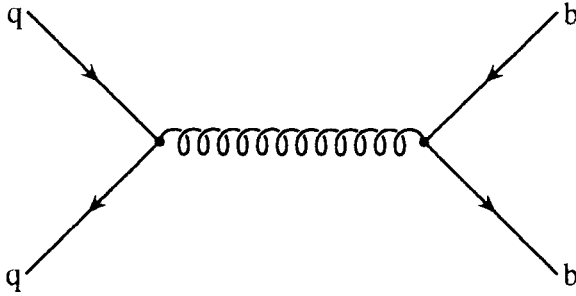


Figure 1.1: A Feynmann graph of $\bar{b}b$ production from quark annihilation.

1.3 B Decays

B mesons decay weakly to hadronic and semileptonic final states. B mesons typically have a long lifetime of ~ 1.5 ps due to the suppression of b -quark decays from the CKM matrix. A b -quark decays to a c -quark and, more rarely, a u -quark, along with a virtual W boson.

Weak decays can be categorized into external and internal diagrams. External diagrams describe some decays in which the virtual W boson is outside the weak decay vertex and the spectator quark as in Figure 1.3. In these decays, the final state particles from the W do not hadronize with the spectator quark. Internal diagrams are always hadronic. The final state particles from an internal W hadronize with the spectator quark as shown in Figure 1.4. Internal diagrams are color-suppressed since the antiquark from the virtual W^+ (q_1 in Figure 1.3) must have the anti-color of the c -quark. The c -quark and the \bar{q}_1 -quark must form a “colorless” final state.

Both external and internal processes have been observed experimentally and phe-

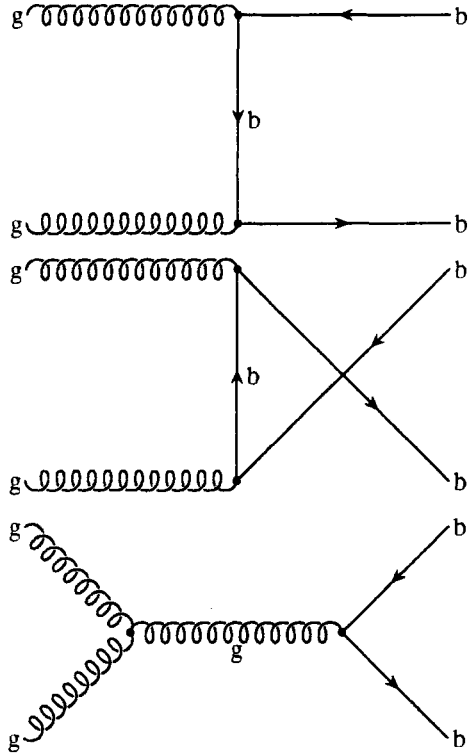


Figure 1.2: A Feynmann graph showing $\bar{b}b$ production from gluon interactions.

nomenological models such as factorization are attempting to explain experimental results. Factorization is presently more successful with the simpler case of external diagrams. Internal diagrams are more complex because of hadronization effects. These effects are typically accounted for by form factors.

The B_u^+ meson decays to $J/\psi K^+$ through an internal diagram. The \bar{b} -quark decays to a \bar{c} -quark and a virtual W^+ . The W^+ is internal and hadronizes as a c -quark and \bar{s} -quark. Figure 1.5 shows the tree level decay.

The B_c^+ meson decays to $J/\psi \pi^+$ through an external diagram. The \bar{c} -quark from the \bar{b} -decay forms a J/ψ with the spectator c -quark. The W^+ hadronizes as π^+ .

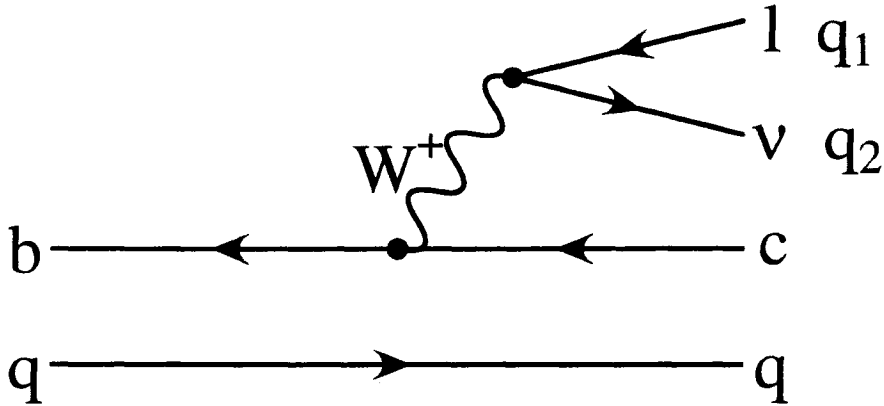


Figure 1.3: A Feynmann graph of B meson decay with an external W boson.

Figure 1.6 shows the decay.

1.4 The CKM Matrix

The weak force's coupling to matter exhibits $SU_{weak}(2)$ isospin symmetry for both leptons and quarks. Leptons of the same generation may be coupled by a W^+, W^- or Z^0 . The weak force does not couple leptons of different generations because lepton family number is conserved. However, the weak force couples leptons of the same weak-isospin doublet, as shown in equation (1.1) below.

$$\begin{pmatrix} e^- \\ \nu_e \end{pmatrix} \quad \begin{pmatrix} \mu^- \\ \nu_\mu \end{pmatrix} \quad \begin{pmatrix} \tau^- \\ \nu_\tau \end{pmatrix} \quad (1.1)$$

The symmetry is broken for quarks since quarks of different generations can be coupled by the weak bosons (W^+, W^- or Z^0).

The $SU_{weak}(2)$ symmetry is restored to quarks by permitting the quark generations

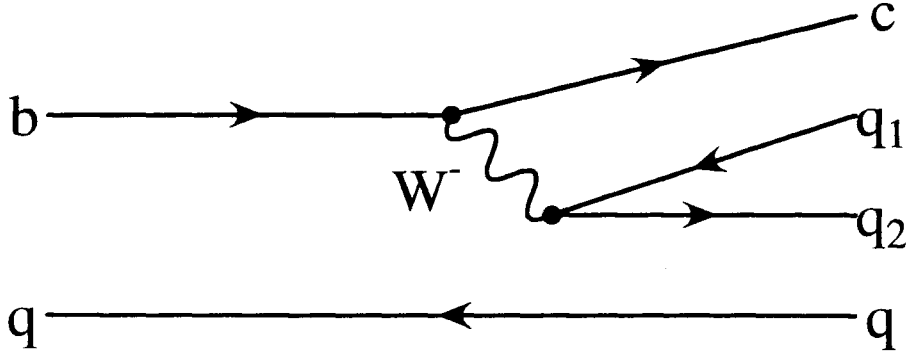


Figure 1.4: A Feynmann graph of B meson decay with an internal W boson. The c -quark and the \bar{q} -quark, one quark from each end of the W propagator, hadronize into the same final state particle. That final state particle must be “colorless.”

to be redefined as linear combinations of quarks. The generations of known quarks are

$$\begin{pmatrix} u \\ d \end{pmatrix} \quad \begin{pmatrix} c \\ s \end{pmatrix} \quad \begin{pmatrix} t \\ b \end{pmatrix}. \quad (1.2)$$

The linear combination of quarks which explains experimental observations is

$$\begin{pmatrix} u' \\ d' \end{pmatrix} \quad \begin{pmatrix} c' \\ s' \end{pmatrix} \quad \begin{pmatrix} t' \\ b' \end{pmatrix}. \quad (1.3)$$

There is enough freedom to define the $I_3 = +\frac{1}{2}$ elements of the weak isospin doublet to be identical to the corresponding elements of the generational doublets of equation (1.2). Namely,

$$u' = u, \quad c' = c, \quad t' = t. \quad (1.4)$$

The $I_3 = -\frac{1}{2}$ elements are related to the actual quarks by the Cabibbo-Kobayashi-

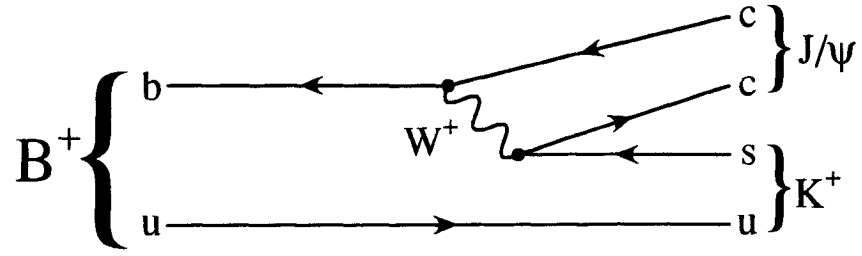


Figure 1.5: The figure shows the Feynmann diagram for the $B_u^+ \rightarrow J/\psi K^+$ decay mode.

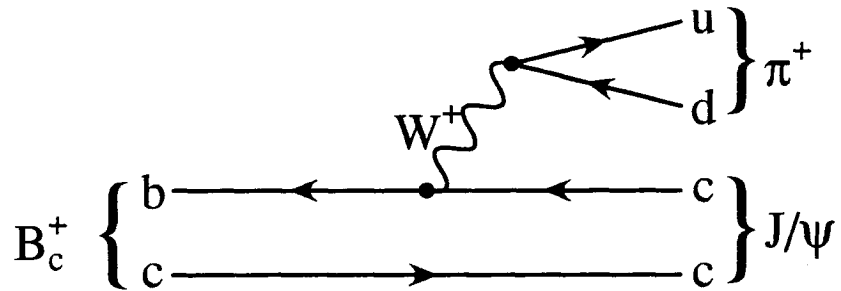


Figure 1.6: The figure shows the Feynmann graph for the $B_c^+ \rightarrow J/\psi \pi^+$ decay mode.

Maskawa (CKM) matrix[11, 12]

$$\begin{pmatrix} d' \\ s' \\ b' \end{pmatrix} = U_{\text{CKM}} \begin{pmatrix} d \\ s \\ b \end{pmatrix}, \quad (1.5)$$

where U_{CKM} is the CKM matrix given by

$$U_{\text{CKM}} = \begin{pmatrix} V_{ud} & V_{us} & V_{ub} \\ V_{cd} & V_{cs} & V_{cb} \\ V_{td} & V_{ts} & V_{tb} \end{pmatrix}. \quad (1.6)$$

The complex coupling strength of quark i , with charge $Q_i = \frac{2}{3}$, to quark j , with charge $Q_j = -\frac{1}{3}$, is V_{ij} .

The parameterization suggested by Chau and Keung[13] for the matrix in terms of four angles is given by

$$U_{\text{CKM}} = \begin{pmatrix} c\theta_{12}c\theta_{13} & s\theta_{12}c\theta_{13} & s\theta_{13}e^{-i\delta_{13}} \\ -s\theta_{12}c\theta_{23} - c\theta_{12}s\theta_{23}s\theta_{13}e^{i\delta_{13}} & c\theta_{12}c\theta_{23} - s\theta_{12}s\theta_{23}s\theta_{13}e^{i\delta_{13}} & s\theta_{23}c\theta_{13} \\ s\theta_{12}c\theta_{23} - c\theta_{12}s\theta_{23}s\theta_{13}e^{i\delta_{13}} & -c\theta_{12}s\theta_{23} - s\theta_{12}c\theta_{23}s\theta_{13}e^{i\delta_{13}} & c\theta_{23}c\theta_{13} \end{pmatrix}, \quad (1.7)$$

where $s\theta_{ij}$ is the sine of angle θ_{ij} and $c\theta_{ij}$ is the cosine of angle θ_{ij} . The subscripts, i and j , label the generations $\{i, j = 1, 2, 3\}$. The angle δ_{13} introduces the phase which makes the matrix complex. In the case of $\theta_{13} = \theta_{23} = 0$, the CKM matrix reduces to the Cabibbo matrix, with θ_{12} identified as the Cabibbo angle.

The presently published experimental values, at the 90% confidence level, from the Particle Data Group[14] are

$$U_{\text{CKM}} = \begin{pmatrix} 0.9745 - 0.9757 & 0.219 - 0.224 & 0.002 - 0.005 \\ 0.218 - 0.224 & 0.9736 - 0.9750 & 0.036 - 0.046 \\ 0.004 - 0.014 & 0.034 - 0.046 & 0.9989 - 0.9993 \end{pmatrix}, \quad (1.8)$$

with corresponding 90% confidence level measurements on the angles of

$$\begin{aligned}\theta_{12} &= 0.221 - 0.225 \\ \theta_{13} &= 0.036 - 0.046 \\ \theta_{23} &= 0.002 - 0.005.\end{aligned}\tag{1.9}$$

The above parameters can be determined from weak decays of the relevant quarks. In the case of elements involving the top quark, results are derived from theoretical considerations of mixing and penguin decays.

1.5 Cabibbo-Suppressed Decay Modes

Cabibbo-suppressed modes may arise when a W^+ or W^- couples quarks of different generations. A vertex with a W^\pm and two quarks is Cabibbo-preferred if q_1 and q_2 are from the same generation. If the quark generations differ by one, the vertex is Cabibbo-suppressed. A decay mode, however, may exhibit one or more Cabibbo-suppressed vertices and still be preferred due to kinematics. For example, B hadrons may decay by the b -quark's decay to a c -quark. Historically, this would be considered a Cabibbo-suppressed decay. However, we consider in this thesis the first kinematically allowed mode to be Cabibbo-favored. Therefore, a b -quark's decay to a c -quark is not a Cabibbo-suppressed decay since the bottom quark can not decay to a heavier t -quark. A decay mode is Cabibbo-suppressed if it exhibits coupling of quarks from generations further than kinematically necessary. For n quark generations, a decay

can be at most $(2n - 2)$ -fold Cabibbo-suppressed¹. The relative rate of a suppressed

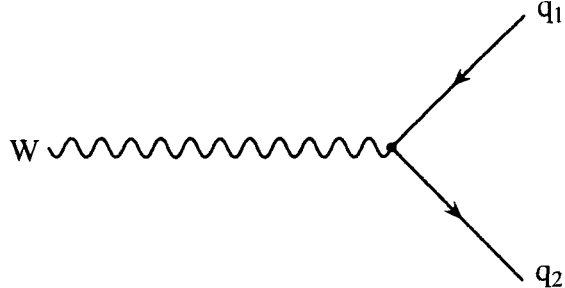


Figure 1.7: The figure shows quarks q_1 and q_2 coupled by a W^\pm intermediate vector boson.

decay in comparison to a favored decay is given by eq. (1.10).

$$\frac{\mathcal{B}(\text{suppressed})}{\mathcal{B}(\text{favored})} = \frac{|V_{ij}|^2 f_1}{|V_{ik}|^2 f_2}, \quad (1.10)$$

where f_1 and f_2 are form factors for the final hadronic state of the suppressed and favored quark, respectively, and V_{ij} and V_{ik} are different elements of the CKM matrix.

Both elements are from the same row or column.

Figure 1.8 shows a Feynmann diagram for a simple Cabibbo-suppressed mode in comparison to the favored mode. The Cabibbo-favored mode is $B_u^+ \rightarrow J/\psi K^+$ since the c -quark and \bar{s} -quark are both from the second generation. $B_u^+ \rightarrow J/\psi \pi^+$ is Cabibbo-suppressed since the \bar{d} -quark is from the first generation. The W^+ meson is also coupled to a \bar{b} -quark and a \bar{c} -quark. This is a Cabibbo-suppressed vertex, but not

¹The maximum suppression comes from a decay in which the heaviest quark decays into a W^\pm and a first generation quark, followed by the W^\pm hadronizing as the heaviest quark's weak-isospin partner and a first generation quark. Both parts are $(n - 1)$ -fold suppressed, giving a total of $(2n - 2)$ -fold suppression.

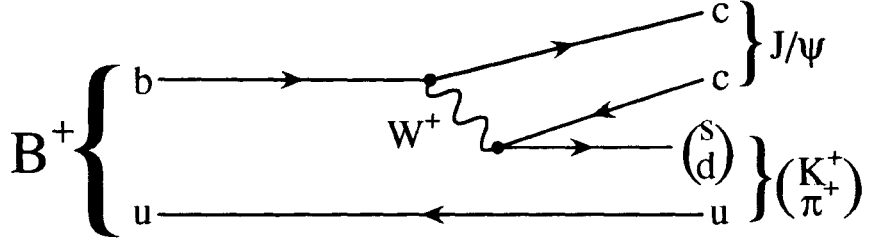


Figure 1.8: The figure shows the Cabibbo-favored $B_u^+ \rightarrow J/\psi K^+$ and the Cabibbo-suppressed $B_u^+ \rightarrow J/\psi \pi^+$ modes.

a Cabibbo-suppressed mode because the decay $\bar{b} \rightarrow \bar{t}W^+$ is kinematically forbidden.

Until recently, Cabibbo-suppressed couplings had only been observed for strange and charm quarks. With large numbers of fully reconstructed b -hadrons at modern colliders, Cabibbo-suppressed B -decays are becoming distinguishable.

1.6 Factorization Hypothesis

The factorization hypothesis is based on the assumption that the weak current can be separated into components. For B meson decay to a charmonium final state, for instance, the interaction Hamiltonian is factored as [15]

$$\langle \bar{c}c + \bar{s}q | T | \bar{b}q \rangle \propto \langle \bar{c}c | J^\mu | 0 \rangle \langle \bar{s}q | J_\mu | B \rangle . \quad (1.11)$$

This method is believed to be more reliable for external diagrams, such as semileptonic decays, than internal decays, such as $B_u^+ \rightarrow J/\psi K^+$. The factorization hypothesis has worked well for external diagrams. We will test the factorization hypothesis

for internal decays in this thesis.

The matrix element[16] in the factorization hypothesis for $B_u^+ \rightarrow J/\psi K^+$ is

$$M(B_u^+ \rightarrow J/\psi K^+) = i \frac{G_w}{2} |V_{bc}^*| |V_{cs}| f_K(m_B^2 - m_\psi^2), \quad (1.12)$$

where V_{bc}^* and V_{cs} are CKM matrix elements, G_w is the weak coupling constant, f_K is the kaon's form factor and m_B and m_ψ are the mass of the B_u^+ and J/ψ , respectively.

By simple transformations, the matrix element for $B_u^+ \rightarrow J/\psi \pi^+$ is

$$M(B_u^+ \rightarrow J/\psi \pi^+) = i \frac{G_w}{2} |V_{bc}^*| |V_{cd}| f_\pi(m_B^2 - m_\psi^2). \quad (1.13)$$

Since we are interested in the ratio of branching ratios to reduce systematic uncertainties in the experiment and theory, we find the theoretical ratio

$$\frac{\mathcal{B}(B_u^+ \rightarrow J/\psi \pi^+)}{\mathcal{B}(B_u^+ \rightarrow J/\psi K^+)} = \frac{\Gamma(B_u^+ \rightarrow J/\psi \pi^+)/\Gamma_{\text{TOT}}}{\Gamma(B_u^+ \rightarrow J/\psi K^+)/\Gamma_{\text{TOT}}}. \quad (1.14)$$

Inserting,

$$\Gamma = \frac{P_{\text{cm}}}{8\pi m_B^2} |M|^2, \quad (1.15)$$

where P_{cm} is the momentum of the final state particles in the B_u^+ meson's rest frame, we find

$$\frac{\mathcal{B}(B_u^+ \rightarrow J/\psi \pi^+)}{\mathcal{B}(B_u^+ \rightarrow J/\psi K^+)} = \frac{|M(B_u^+ \rightarrow J/\psi \pi^+)|^2}{|M(B_u^+ \rightarrow J/\psi K^+)|^2} \frac{P_{\text{cm}}^{\psi \pi^+}}{P_{\text{cm}}^{\psi K^+}}$$

$$= \frac{|V_{cd}|^2}{|V_{cs}|^2} \frac{f_\pi^2}{f_K^2} \frac{P_{\text{cm}}^{\psi\pi^+}}{P_{\text{cm}}^{\psi K^+}} \quad (1.16)$$

$$= \tan^2 \theta_c \frac{f_\pi^2}{f_K^2} \frac{P_{\text{cm}}^{\psi\pi^+}}{P_{\text{cm}}^{\psi K^+}}, \quad (1.17)$$

where θ_c is the Cabibbo angle in the approximation that the first and third generations decouple.

The center-of-mass momentum is easily calculated by considering the two-body decay shown in Figure 1.9.

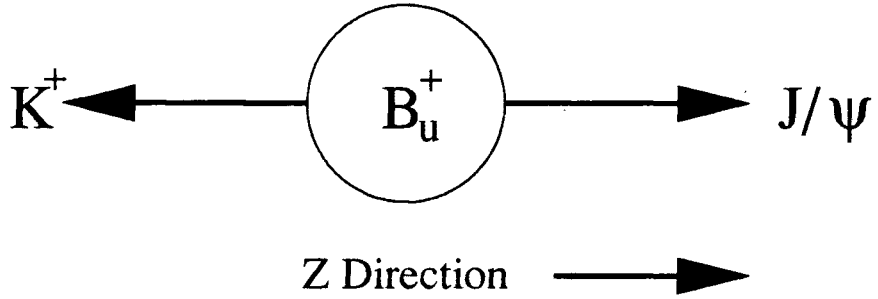


Figure 1.9: A B_u^+ decays into two particles, J/ψ and K^+ , which have momentum $\pm P$ along the z-axis.

$$\begin{bmatrix} m_B \\ 0 \\ 0 \\ 0 \end{bmatrix} = \begin{bmatrix} \sqrt{P^2 + m_{J/\psi}^2} \\ 0 \\ 0 \\ P \end{bmatrix} + \begin{bmatrix} \sqrt{P^2 + m_K^2} \\ 0 \\ 0 \\ -P \end{bmatrix} = \begin{bmatrix} \sqrt{P^2 + m_{J/\psi}^2} + \sqrt{P^2 + m_K^2} \\ 0 \\ 0 \\ 0 \end{bmatrix}, \quad (1.18)$$

where P is the magnitude of the momentum for the J/ψ or K^+ in the B_u^+ meson's rest frame.

This yields a center-of-mass momentum for the $J/\psi K^+$ case of

$$P_{\text{cm}}^{\psi K} = \frac{\left[M_B^4 + M_{J/\psi}^4 + M_K^4 - 2M_B^2 M_{J/\psi}^2 - 2M_B^2 M_K^2 - 2M_{J/\psi}^2 M_K^2 \right]^{\frac{1}{2}}}{2M_B} \quad (1.19)$$

$$= 1.683 \text{ GeV}/c. \quad (1.20)$$

By replacing M_K with M_π ,

$$P_{\text{cm}}^{\psi\pi} = \frac{\left[M_B^4 + M_{J/\psi}^4 + M_\pi^4 - 2M_B^2 M_{J/\psi}^2 - 2M_B^2 M_\pi^2 - 2M_{J/\psi}^2 M_\pi^2 \right]^{\frac{1}{2}}}{2M_B} \quad (1.21)$$

$$= 1.727 \text{ GeV}/c. \quad (1.22)$$

Using values for the form factors of $f_k = 162 \text{ MeV}/c$ and $f_\pi = 132 \text{ MeV}/c$ [17] and $\tan \theta_c = 0.227$ [14], we find the theoretical ratio of branching ratios in the factorization hypothesis to be

$$\frac{\mathcal{B}(B_u^+ \rightarrow J/\psi \pi^+)}{\mathcal{B}(B_u^+ \rightarrow J/\psi K^+)} = (0.227)^2 \left(\frac{132}{162} \right)^2 \left(\frac{1.727}{1.683} \right) = 3.5\%. \quad (1.23)$$

The CLEO Collaboration has reported a measurement of this ratio based on 4.2 signal events. They calculate a ratio of $(4.3 \pm 2.3)\%$ [18]. This thesis reports on our measurement of this ratio.

1.7 B_c^+ Physics

The B_c^+ meson is of great theoretical interest because it is the intermediate state between charmonium and bottomonium, which are described well by present potential models. It is also of great experimental interest since it would be the first particle discovered with two different heavy quarks. Since it does have two heavy quarks, the non-relativistic approximation can be used more reliably to characterize the spectroscopy. The B_c^+ meson can also test the spectator model since both the b -quark and c -quark can decay.

Using four different potential models that parameterize the data well for ψ and Υ , Eichten and Quigg [19] calculate

$$M_{B_c} = 6.258 \pm 0.020 \text{ GeV}/c. \quad (1.24)$$

The lifetime prediction varies greatly from 0.4 ps [21] to 1.44 ps [22]. The variations depend on the amount of suppression for b -quark and c -quark decays due to binding. The lifetime is given by

$$\frac{1}{\tau_{B_c}} = \Gamma_b + \Gamma_c + \Gamma_{\text{anni}}, \quad (1.25)$$

where Γ_b is the partial width of b -quark decay, Γ_c is the partial width of c -quark decay and Γ_{anni} is the partial width for annihilation.

Quantity	Chang[21]	Quigg[22]
$\Gamma_b (10^{11} s^{-1})$	6.7	3.9
$\Gamma_c (10^{11} s^{-1})$	14.5	0.7
$\Gamma_{\text{anni}} (10^{11} s^{-1})$	3.8	2.2
τ_{B_c} (ps)	0.40	1.44
$\Gamma_b/\Gamma_{\text{TOT}}$	27%	57%

Table 1.1: Shown are the differences in predicted widths and lifetimes for B_c^+ under two sets of different assumptions regarding inter-quark binding.

The amount of suppression attributed to each partial width not only affects the lifetime, but the branching ratio to $J/\psi\pi^+$, the mode of interest.

$$\mathcal{B}(B_c^+ \rightarrow J/\psi\pi^+) \propto \frac{\Gamma_b}{\Gamma_{tot}}, \quad (1.26)$$

where Γ_{tot} is the total width for B_c^+ decay. The last line of Table 1.1 shows that there is a two-fold difference in branching ratio predictions for $B_c^+ \rightarrow J/\psi\pi^+$.

Perturbative QCD calculations indicate that spectator $\bar{c}c$ production is highly suppressed in b -quark hadronization due to the heavy charm quark mass. The fraction of b -quarks that hadronize to produce B_c^+ mesons is estimated to be $\sim 1.5 \times 10^{-3}$ [20] from cross section calculations. Based on an estimated branching ratio $\mathcal{B}(B_c^+ \rightarrow J/\psi\pi^+) = 0.2\%$ [21] and the assumption that 40% of b -quarks hadronize as B_u^+ mesons,

we calculate the expected ratio of $B_u^+ \rightarrow J/\psi\pi^+$ events to $B_c^+ \rightarrow J/\psi\pi^+$ events

$$\frac{\#B_u^+ \rightarrow J/\psi\pi^+}{\#B_c^+ \rightarrow J/\psi\pi^+} \sim \frac{0.05 \times 0.40}{1.5 \times 10^{-3}} \cdot \frac{0.1\%}{0.2\%} = 7. \quad (1.27)$$

1.8 Summary

The field of B physics is a rich testing ground of the Standard Model. By continuing to perform precision measurements, we can constrain the parameters that characterize the Standard Model, searching for the first evidence for physics that is unexplainable by our present understanding. The heavy nature of the b -quark makes theoretical predictions more precise. In this thesis, we explore two predictions of the Standard Model: the relative rate of the Cabibbo-suppressed $B_u^+ \rightarrow J/\psi\pi^+$ decay mode compared with $B_u^+ \rightarrow J/\psi K^+$ and the existence of the B_c^+ .

Chapter 2

Experimental Setup

The experimental data of 35 million events were recorded during the 1992 - 1995 Fermilab Tevatron Runs 1a and 1b at the Collider Detector at Fermilab (CDF). These runs were conducted in colliding beam mode at $\sqrt{s} = 1.8$ TeV. The detector for CDF is located at B0, one of six collision points on the Tevatron ring. This chapter will discuss the acceleration process and detecting facility.

2.1 Generation of Colliding Beams

Protons and their antiparticles, antiprotons, undergo several steps to prepare them for data-production at $\sqrt{s} = 1.8$ TeV. One step in this process is the production of antiprotons. After production, antiprotons are accelerated similarly to protons.

Fermilab produces antiprotons from high energy collisions of protons with a target. The protons are first accelerated to an energy of 120 GeV in the Main Ring (see below). The protons are extracted and transported to a target area. When the protons strike the target, the collisions produce many particles including antiprotons.

2.2 Acceleration Procedure

The acceleration process begins at the Cockcroft-Walton. Here, negatively charged hydrogen ions are produced when electrons are bound to hydrogen atoms. The ions are accelerated by an electric field to an energy of 750 KeV.

The second stage of the acceleration process utilizes the linear accelerator, referred to as LINAC. The 500-foot long accelerator furnishes 400 MeV protons for the next stage.

The booster accepts the 400 MeV protons and accelerates them to 8 GeV during approximately 20,000 revolutions through this synchrotron. The booster is a 500-foot diameter ring located 20 feet below ground. The booster then permits injection of the bunches into the Main Ring.

The Main Ring is another proton synchrotron that is approximately 4 miles in circumference. A toroidal tunnel holds the one thousand copper-coiled magnets which accelerate the protons in a circle to 150 GeV.

The Tevatron, named for its near 1 TeV capability per beam, is located in the same tunnel as the main ring. One thousand superconducting magnets comprise the Tevatron which accepts 150 GeV protons and antiprotons from the Main Ring and accelerates them to 900 GeV. The protons and antiprotons travel in bunches, six for each type, and may collide in six fixed locations along the ring. CDF is located at one of the two sites that house major detectors.

2.3 The Collider Detector at Fermilab (CDF)

The CDF experiment, located at the B0 collision point of Fermilab's Tevatron, is a cylindrically symmetric detector designed to observe a wide variety of physics results. The detector, which was basically completed in 1987, the year of its first physics run, is a 5,000 ton machine comprised of many systems[23]. The detector components relevant to this analysis are described below.

2.4 The Central Tracking Chamber (CTC)

The Central Tracking Chamber (CTC), located inside the 1.41 T solenoid, is a wire chamber that measures the momentum vectors of individual charged particles. This complements the calorimetry, which provides information about jets. Precision measurement of individual charged particles is essential for identifying narrow B resonances. In particular, separation of $B_u^+ \rightarrow J/\psi\pi^+$ decays from $B_u^+ \rightarrow J/\psi K^+$ decays is nearly impossible without accurate momentum measurement.

The CTC is a cylinder of diameter 276.00 cm and length 320.13 cm, including the endplates which are 2.00 inch thick aluminum disks terminating the drift wires[24]. Nine “superlayers” group the wires by type, either axial or stereo. The even superlayers (0,2,4,6,8) are axial and contain twelve sense wire layers. Separating the axial superlayers are the four odd superlayers with stereo wires alternating between $\pm 3^\circ$ with respect to the axial direction. A superlayer is divided into cells, each of which

contains one set of drift wires. Table 2.1 describes the layout of the sense wires in the chamber and Figure 2.1 shows the endplate view.

The z -resolution of a stereo wire is approximately 4 mm. In addition, the axial layers give a momentum resolution of

$$\frac{\delta P_T}{P_T} = 0.001 P_T \quad (2.1)$$

when the particle is constrained to come from the beam. Together the axial and stereo superlayers give a good measurement of the track's momentum.

2.5 Vertex Time Projection Chamber (VTX)

The vertex time projection chamber (VTX), which was installed in 1992 for Run 1, precisely measures the z -component of the primary vertex. Eight time projection modules comprise the 2.8 m long VTX system. The 3072 sense wires measure $r - z$ hits and 3072 pads measure $r - \phi$, for radii between 6.8 cm and 21 cm[23]. The VTX attempts to minimize the presence of material which causes multiple scattering before the CTC has a chance to make a measurement.

2.6 Silicon Vertex Detector (SVX and SVX')

The Silicon Vertex Detector (SVX and SVX') precisely measures displaced vertices and impact parameters. The SVX detector was an upgrade for Run 1a to the original

Superlayer	Stereo Angle	# of super cells	# of sense wires/layer	sense wires
0	0°	30	12	360
1	$+3^\circ$	42	6	252
2	0°	48	12	576
3	-3°	60	6	360
4	0°	72	12	864
5	$+3^\circ$	84	6	504
6	0°	96	12	1152
7	-3°	108	6	648
8	0°	120	12	1440
6156				

Table 2.1: This table shows the orientation and the number of wires in each superlayer of the CTC.

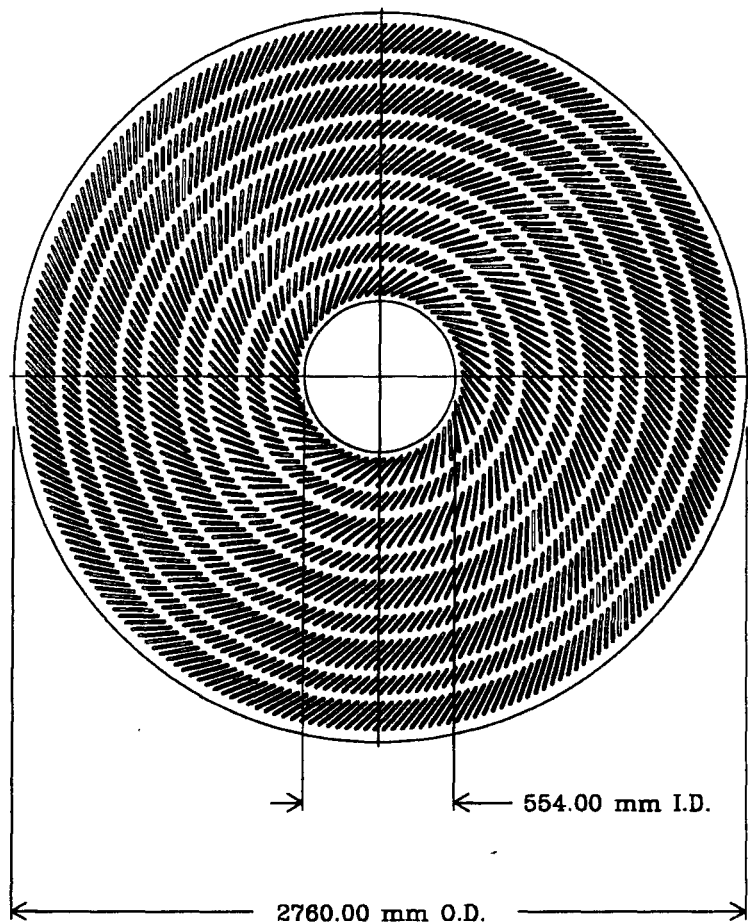


Figure 2.1: The figure shows the view of the CTC from the endplate. There are 6156 sense wires in the CTC.

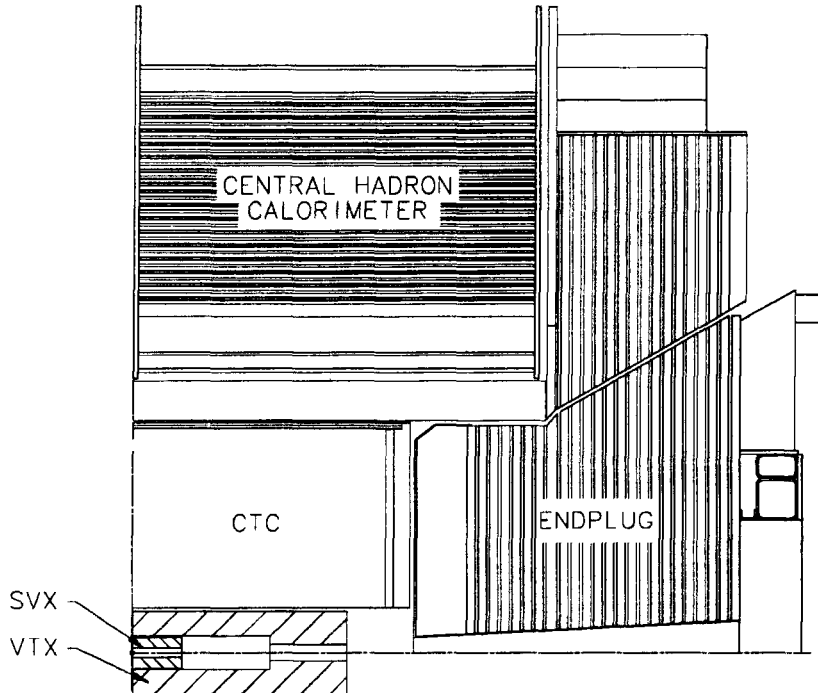


Figure 2.2: A diagram of the location of the SVX within the CDF detector.

CDF detector and fits inside the VTX as shown in Figure 2.2. This allowed for the identification of displaced vertices from B hadrons, which are produced in $b\bar{b}$ pairs and are also decay products of top quarks. The SVX played a critical role in the discovery of the top quark in 1994 [25] by “tagging” b -jets.

The SVX detector, the first silicon vertex detector to be successfully operated in a hadron environment[26], suffered radiation damage during Run 1a and was replaced for Run 1b by the SVX' detector with radiation-hard electronics.

Both detector systems were composed of two separate, identical barrels that were

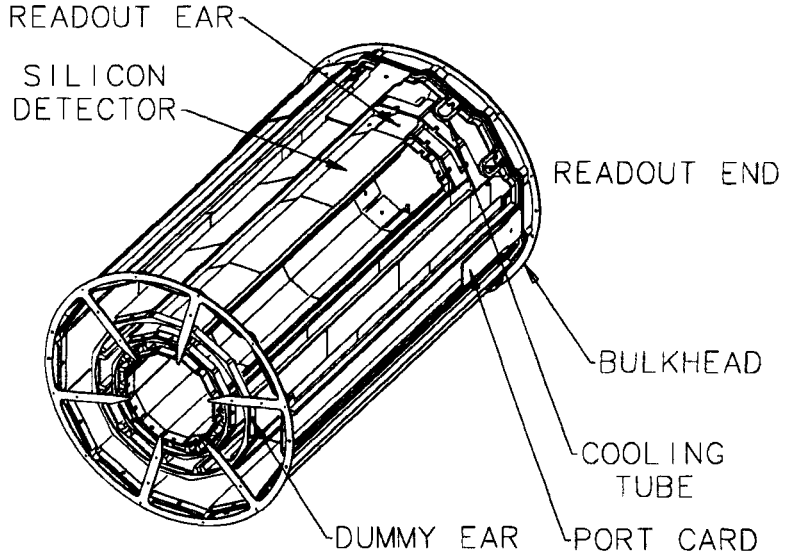


Figure 2.3: A sketch of one of two SVX barrels.

25.5 cm long, separated by a 2.15 cm gap [27]. A barrel is shown in Figure 2.3. The total 51.0 cm length of the detectors covers approximately 60% of collisions since the beam interaction area has a normal distribution with a standard deviation of ~ 30 cm.

The geometries of these two detectors are nearly identical. Both are designed with four layers of single-sided, axial silicon strips which measure the $r - \phi$ coordinate. The major difference is the radius of the innermost layer. Each layer is constructed from twelve ladders, each of which is flat, to form a twelve-sided geometry.

A ladder has three silicon detectors bonded together and attached to electronic readouts, as shown in Figure 2.4. The ladders for each layer have different widths,

Characteristic	SVX	SVX'
channels	46080	
z coverage	51.0 cm	
gap at $z = 0$	2.15 cm	
radius L0	3.0049 cm	2.8612 cm
radius L1		4.2560 cm
radius L2		5.6872 cm
radius L3		7.8658 cm

Table 2.2: This table summarizes some of the characteristics of the SVX and SVX' detectors.

due to different radii, but they all have the same length. Table 2.2 summarizes some characteristics of the two devices.

2.7 Muon Chambers

There are four separate muon systems, which can be identified in Figure 2.5 in the CDF detector. The Central Muon System (CMU) covers pseudorapidity $|\eta| < 0.6$, where pseudorapidity is defined as $\eta = -\ln[\tan \frac{\theta}{2}]$. The Central Muon Upgrade (CMP) covers a similar region, but reduces punch-through contamination. In addition, the Forward Muon System (FMU) covers $2.0 < |\eta| < 3.6$. Furthermore, the

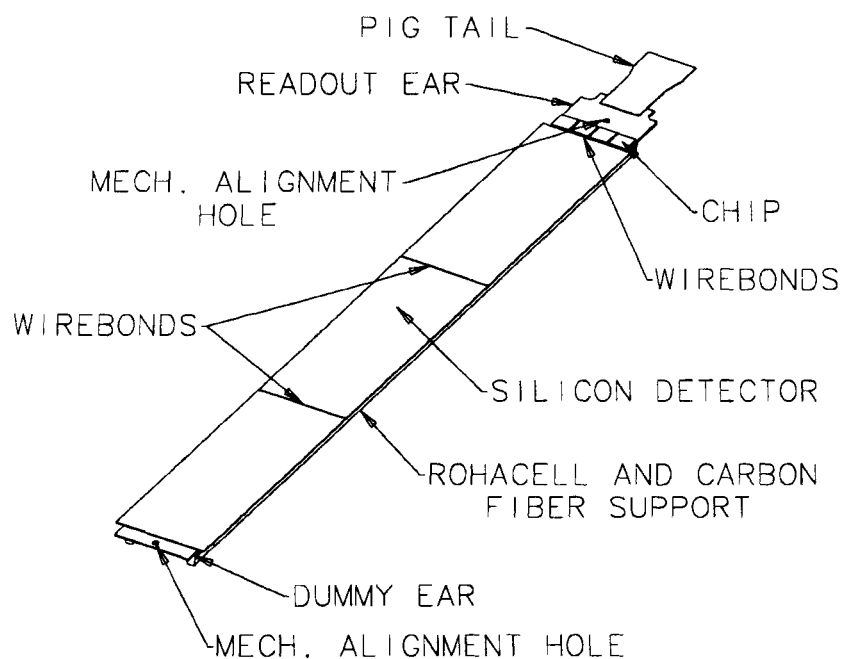


Figure 2.4: A sketch of an SVX ladder.

muon detection capability was enhanced in 1992 by the insertion of the Central Muon Extension (CMX), which covers $0.6 < |\eta| < 1.0$.

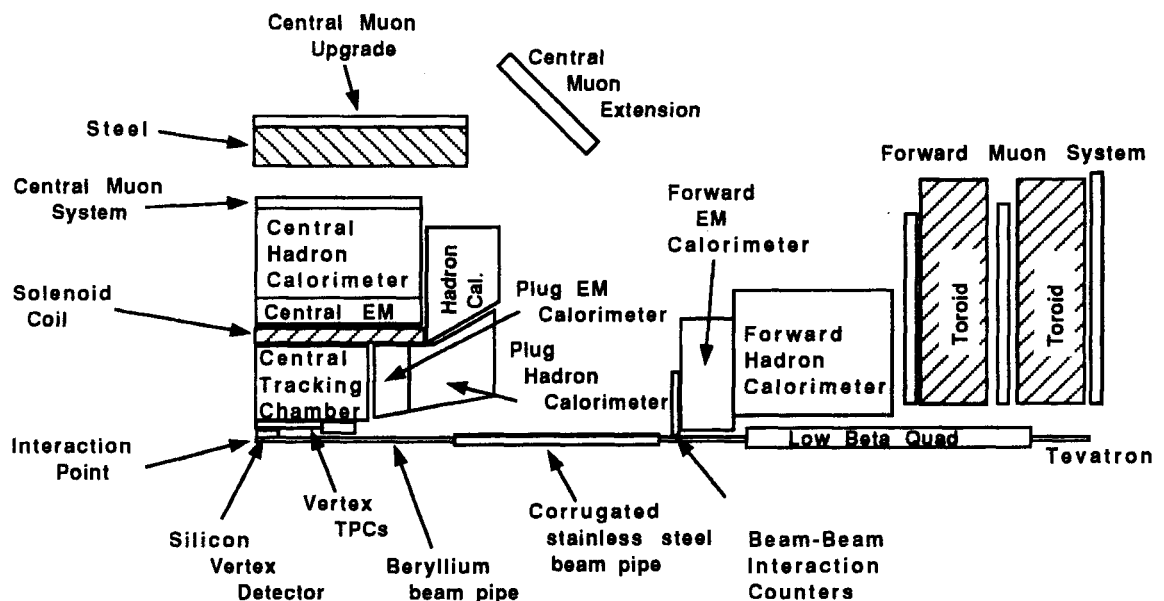


Figure 2.5: This figure shows the location of the four muon detection systems, the Central Muon System, Central Muon Upgrade, Forward Muon System and Central Muon Extension.

2.7.1 Central Muon System (CMU)

The CMU system is located at the outer part of the central calorimeter as show in Figure 2.6, 3.47 m from the beam axis[28]. The muon chamber covers 12.6° of each 15° calorimeter wedge. Each chamber is three modules, which consist of four layers of four rectangular drift cells.

Figure 2.7 shows a single module. By determining the difference in drift time for two different layers, an approximate P_T measurement can be made. The higher the P_T of the muon, the smaller the time difference. This permits a convenient hardware trigger on muons by selecting only events with a small enough drift time.

Only muons with $P_T > 1.4 \text{ GeV}/c$ traverse the detector, including the calorimeter wedges and hit the CMU detector. A trigger on this event may occur if there is a match between the hit in the muon chamber and the track in the CTC.

2.7.2 Central Muon Upgrade (CMP)

The Central Muon Upgrade (CMP) is located behind steel shielding, which reduces the punch-through contamination, but only allows muons with $P_T > 2.5 \text{ GeV}/c$. The region of coverage extends the central muon capability slightly beyond the CMU.

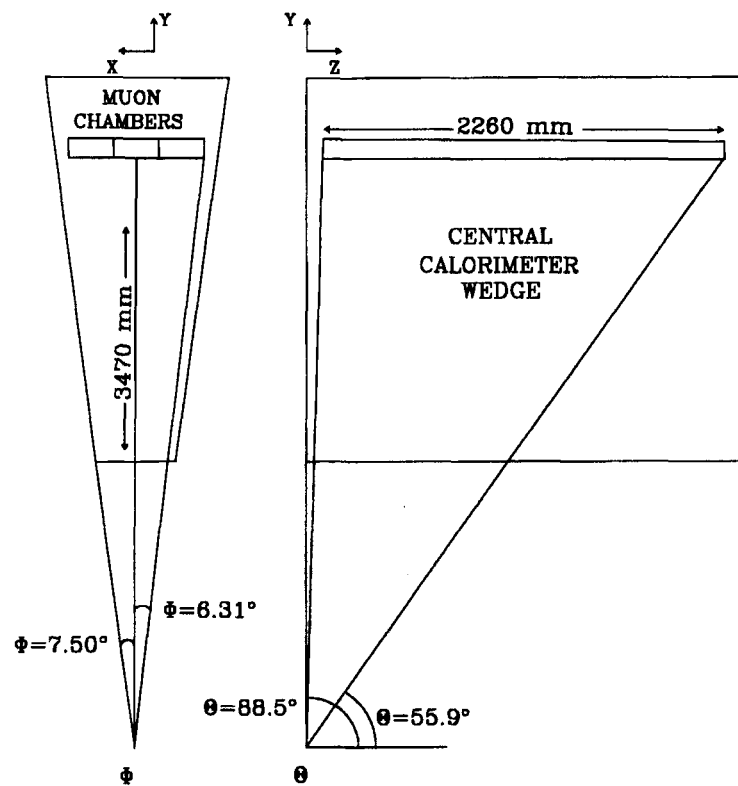


Figure 2.6: The figure shows the layout of the CMU within the Central Calorimeter.

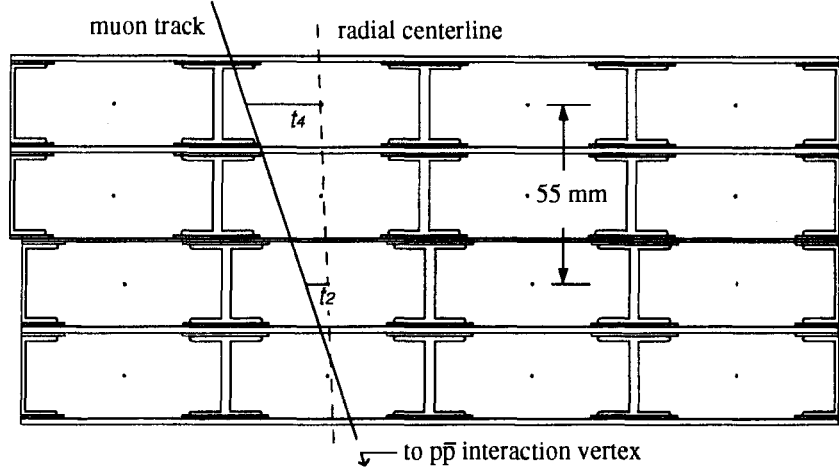


Figure 2.7: The figure shows the cross-section of a single muon module. The difference in drift time is related to the P_T of the track since the slope of the track in the $x - y$ plane depends on the track's curvature in the magnetic field.

2.7.3 Central Muon Extension (CMX)

The Central Muon Extension (CMX) furthers the region of coverage for central muons by covering the region from $0.6 < |\eta| < 1.0$. There is a small overlap between this detector and the CMU.

2.7.4 Forward Muon System (FMU)

The Forward Muon System (FMU) measures muon positions and momentum for polar angles between 3° and 16° and between 164° and 177° [29]. This coverage corresponds to $2.0 < |\eta| < 3.6$. The FMU consist of a pair of magnetized iron toroids. The detector

has three sets of drift chambers and two planes of scintillation trigger counters which are used to measure muons passing through the system.

Chapter 3

Data Sample

The data were collected by CDF during the 1992-1993 Run 1a and 1994-1995 Run 1b Tevatron runs at $\sqrt{s} = 1.8$ TeV. The sample of approximately 35 million events corresponds to a total integrated luminosity of 110 pb^{-1} . The data sample for this thesis was obtained by triggering on J/ψ candidates. We reconstruct $402\,500 \pm 700$ J/ψ candidate mesons.

3.1 J/ψ Trigger

The J/ψ trigger is used to select events with a J/ψ from an enormous background of less interesting events. The multi-level triggering scheme at CDF utilizes various pieces of hardware.

The Level-1 trigger searches for muons above a P_T threshold determined by the difference in drift time measured by alternating drift layers, as described in Section 2.7.1. A calorimeter tower will trigger if any of the three muon modules observe a particle with large enough P_T .

The Level-2 trigger attempts to match triggered muon towers to central fast tracks (CFT), tracks reconstructed quickly using dedicated hardware with a fast algorithm. If the track extrapolates to a muon chamber which triggered at Level-1, the associated calorimeter wedge is labeled as a gold muon[30].

Various triggers exist at Level-2. Most require two gold muons. The triggers are described below.

TWO_CMU_TWO_CFT: Requires two Level-2 clusters in CMU. There must be a TWO_CMU_3PT3 trigger at Level-1 and a one wedge separation in ϕ .

CMX_CMU_TWO_CFT: Requires one Level-2 cluster in the CMU and one in the CMX. There must be a TWO_CMU_3PT3 trigger at Level-1.

CMX_CFT_CMUP_CFT: Requires one Level-2 cluster in the CMX and one in the CMUP. There must be a TWO_CMU_3PT3 trigger at Level-1.

TWO_CMX_TWO_CFT: Requires two Level-2 clusters in CMX. There must be a TWO_CMU_CMX_3PT3 trigger at Level-1 and a one wedge separation in ϕ .

TWO_CMU_CMX_ONE_CFT: Requires one Level-2 cluster in CMU. There must also be a second Level-1 stub in CMU or CMX.

TWO_CMU_ONE_CFT_6TOW: Requires one Level-2 cluster in CMU. The highest P_T muon cluster must have six or more towers. There must also be a TWO_CMU_3PT3 trigger at Level-1.

Level-3 does a more thorough physics analysis with the muons. The invariant mass of the muons is calculated and required to be within $300 \text{ MeV}/c^2$ of the J/ψ world average mass[14]. Events passing the criteria are written to tape for offline analysis.

3.2 Offline Production

Events written to tape are processed by the CDF production farm, a network of computers that convert the raw data into more convenient groupings and do some reconstruction. A more detailed tracking algorithm is applied and the events are split into different data sets based on their trigger type.

Chapter 4

Tracking

The separation of $B_u^+ \rightarrow J/\psi\pi^+$ from $B_u^+ \rightarrow J/\psi K^+$ depends heavily on the quality of the charged particle tracking. Since the two decay modes are so similar, each having three final state tracks with nearly identical corresponding momenta distributions, only well measured tracks, which yield a narrow B peak, will permit success.

There are two different reconstructed track types at CDF:

1. CTC - a three dimensional track fit from observed charge deposits in the CTC.
2. SVX - the same three dimensional CTC track with additional two-dimensional SVX information.

4.1 CTC Tracking

The charged tracks used in this analysis are all measured by the CTC (see Section 2.4). The nine superlayers of the CTC are used to reconstruct the three-dimensional track in stages. First, a two-dimensional fit is done to the observed hits in the five even-

numbered axial superlayers. These two-dimensional tracks are then used as seeds to look for hits in the four odd-numbered stereo superlayers.

Charged tracks traverse a helical path due to the axial magnetic field. The parameters typically used by CDF are:

c - the half-curvature.

ϕ_0 - the initial ϕ of the track.

$\cot \theta$ - the cotangent of the polar angle θ , measured with respect to the z -axis.

d_0 - the two-dimensional impact parameter with respect to the CDF z -axis.

z_0 - the z -position of the helix, where the helix is nearest the z -axis.

4.2 SVX Tracking

The SVX is used to supplement the measurement of a track made by the CTC. After a CTC track has been found, an attempt is made to identify corresponding hits in the SVX. If no SVX hits are found or the information is sub-standard, only the CTC information is used.

The SVX provides only two-dimensional information, but has excellent spatial resolution. This resolution greatly improves the measurement of ϕ_0 and d_0 . When this information is used in a vertex-constrained fit, the mass resolution is significantly improved as seen in Chapter 5.

Track Type	% passing SVX cuts
muons	62
pions and kaons	82

Table 4.1: The table shows the fraction of events in the B_u^+ mass region ($5.0 \text{ GeV}/c^2 < M_{J/\psi K^+} < 5.5 \text{ GeV}/c^2$) passing the SVX selection criteria outlined above.

We require the following for a track's SVX information to be used:

1. Good hits in at least three of the four layers.
2. $P(\chi^2, \text{ndof}) > 1\%$, where P is the probability of the fit being better than the fit from random, unassociated tracks. χ^2 is the observed residual of the fit with ndof degrees of freedom.

We observe that many of the tracks used in the J/ψ sample have good SVX information. Table 4.1 shows the fraction passing the SVX selection cuts.

Chapter 5

J/ψ Reconstruction

J/ψ mesons are a convenient decay product to search for in reconstructing B mesons. A J/ψ event is triggered on in CDF by searching for $\mu^+\mu^-$ pairs with invariant mass near the J/ψ mass of $3.09688 \text{ GeV}/c^2$ [14]. The branching ratio for this decay mode is

$$\mathcal{B}(J/\psi \rightarrow \mu^+\mu^-) = 6.01\% \text{ [14]}. \quad (5.1)$$

5.1 Muon Identification and Selection

The easy identification of muons makes the $J/\psi \rightarrow \mu^+\mu^-$ mode a good trigger. Muons traverse the calorimeter and strike the muon chamber which initiates a trigger based on a rough P_T measurement (see Section 2.7.1).

There are two major backgrounds to muons from the decay vertex. Some particles (notably kaons and pions) will decay into a muon and other particles within the fiducial volume of the detector. The daughter muon often will have a momentum

similar to its parent and generate hits in the detector consistent with the parent track before striking the muon chamber. In addition, highly energetic non-muons can “punch-through” the calorimeter to the muon chamber.

Selection cuts are placed on the muons to minimize backgrounds. These cuts are listed below.

1. $\chi^2(xy - \text{matching}) < 9$
2. $\chi^2(z - \text{matching}) < 12$, for muons with hits in the CMU.

The matching cuts between hits in the muon detectors and central fast tracks, reduce backgrounds from tracks that decay after exiting the tracking chamber.

5.2 J/ψ Reconstruction

The J/ψ is easily reconstructed by adding the muon four-vectors.

$$P_{J/\psi} = P_{\mu^+} + P_{\mu^-} \quad (5.2)$$

In performing this addition, the muons are constrained to come from the same vertex.

The invariant mass is calculated by taking the modulus of the J/ψ four-vector.

$$M_{J/\psi} = \sqrt{P_{J/\psi}^2} = \sqrt{E_{J/\psi}^2 - \vec{P}_{J/\psi}^2} = \sqrt{(E_{\mu^+} + E_{\mu^-})^2 - (\vec{P}_{\mu^+} + \vec{P}_{\mu^-})^2} \quad (5.3)$$

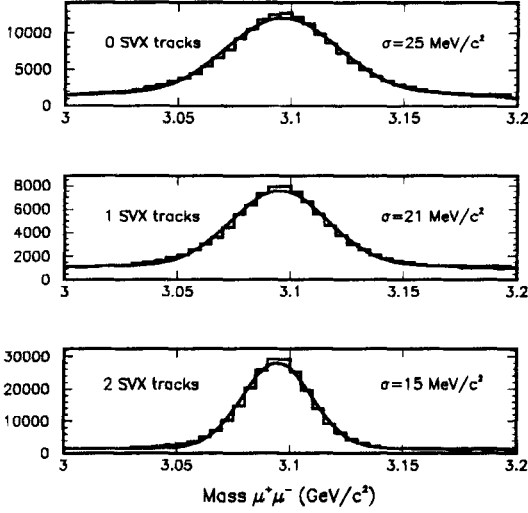


Figure 5.1: The plot shows the invariant mass distribution for dimuons in the J/ψ signal region. There are $402\,500 \pm 700$ signal events. The plots also show that SVX information reduces the mass measurement uncertainty.

Figure 5.1 shows that there are approximately $402\,500 \pm 700$ events in the Run 1a and 1b data samples, after selection criteria have been applied. These plots additionally show the effect of SVX information on the mass resolution.

5.3 Mass Error Scale Factor

Due to difficulties in properly accounting for errors on the track parameters by the pattern recognition program, the error on the mass is not calculated correctly. Fig-

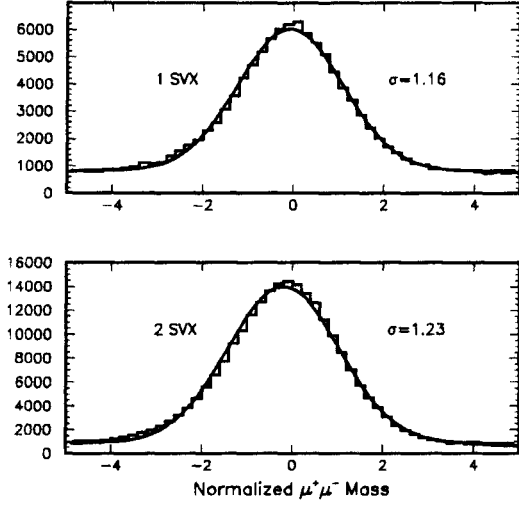


Figure 5.2: The figure shows the normalized mass distributions for dimuon events near the J/ψ mass. The width of the normalized mass distribution is 1.16 for 1 SVX J/ψ candidates and 1.23 for 2 SVX J/ψ candidates.

Figure 5.2 shows the normalized mass plots for 1 and 2 SVX track J/ψ candidates. The widths of the Gaussians are 1.16 for 1 SVX J/ψ candidates and 1.23 for 2 SVX J/ψ candidates. The expected width for correctly calculated uncertainties is 1. These scale factors will be used to select J/ψ mesons for B reconstruction.

Chapter 6

***B* Meson Reconstruction**

B meson reconstruction is founded on the successful reconstruction of J/ψ mesons.

The *B* mesons of interest for this analysis are found through two decays, $J/\psi K^+$ and $J/\psi \pi^+$. The J/ψ mesons are reconstructed from oppositely charged muon pairs (see Chapter 5). Since CDF does not have particle identification in our momentum range, we consider all other charged tracks to be kaons for $J/\psi K^+$ reconstruction and pions for $J/\psi \pi^+$ reconstruction, yielding two invariant masses per three-track combination. Because the detector measures the track's momentum, the only difference between the two above reconstructions is the particle's assumed mass. This affects the track's energy, which is used to determine the three-track invariant mass.

6.1 Track Selection

Charged tracks are identified by the CDF offline pattern recognition code. There are many charged tracks per event, most of which originate at the primary vertex, the point at which the proton and antiproton interact. In order to reduce combinatorics

from low transverse momentum tracks originating at the primary vertex, we apply the following selection criteria to the charged tracks:

- $P_T(K^+, \pi^+) > 1.25 \text{ GeV}/c$
- $\left| \frac{\delta}{\sigma(\delta)} \right| > 1.0 ,$

where P_T is the transverse momentum of the charged track and δ is the signed two-dimensional impact parameter of the track with respect to the measured primary vertex, which has been estimated by the average beam position.

At least two of the three tracks are required to have associated SVX information (see Section 4.2). The first reason for this is to improve mass resolution, which is very important for separating $B_u^+ \rightarrow J/\psi \pi^+$ from $B_u^+ \rightarrow J/\psi K^+$ events. The second reason is to have good information about the location of the secondary vertex, the point at which the B_u^+ decays.

6.2 B Selection

Several requirements are placed on the three-track combination, which is a B meson candidate. These cuts are imposed to enhance the statistical significance of the signal compared with the background, mostly composed of prompt J/ψ mesons and J/ψ mesons from B decays. The cuts take advantage of two natural differences between actual B mesons and backgrounds. The first difference which we exploit is the “harder”

production of B mesons. B mesons tend to have larger transverse momentum than backgrounds. We therefore require

- $P_T(B_u^+) > 5 \text{ GeV}/c$.

The second difference we exploit is the long lifetime ($\sim 1.5 \text{ ps}$) of the B_u^+ relative to the mostly prompt (short-lived) background. We take advantage of this by requiring that the two-dimensional displacement between the primary and secondary vertices, projected along the B_u^+ meson's momentum, L_{xy} , be larger than $150 \mu\text{m}$.

- $L_{xy} > 150 \mu\text{m}$

See Figure 6.1.

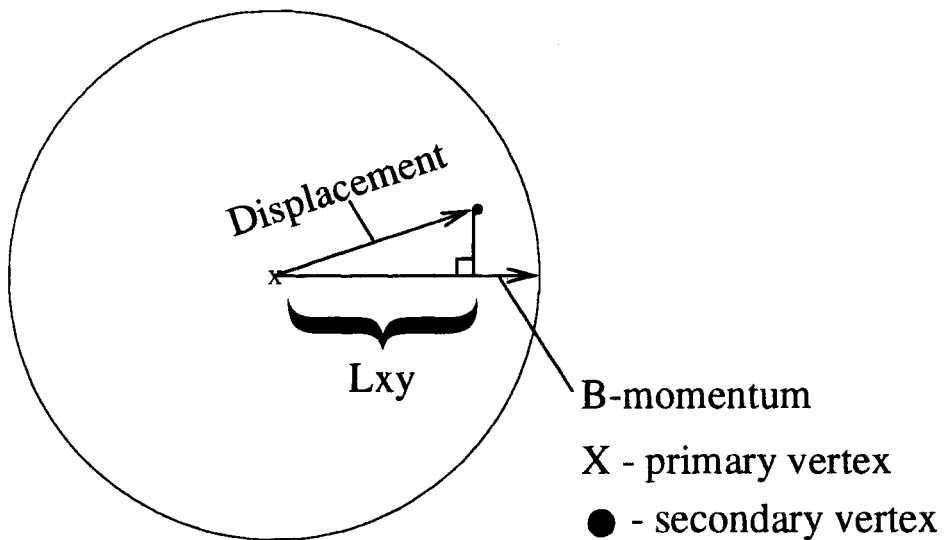


Figure 6.1: The figure shows the primary and secondary vertices and the B meson's momentum direction, all in two dimensions. L_{xy} is the dot product of the displacement vector from the primary to the secondary and the B momentum's unit vector.

6.3 Mass Distributions

The $J/\psi K^+$ and $J/\psi\pi^+$ mass distributions are shown in Figures 6.2 and 6.3, respectively. A clean peak, shown in Figure 6.2, is seen at 5.2789 GeV/ c , identifying the well-known $B_u^+ \rightarrow J/\psi K^+$ decay mode. The $B_u^+ \rightarrow J/\psi\pi^+$ decay mode is concealed on the $J/\psi\pi^+$ mass plot by the residual $B_u^+ \rightarrow J/\psi K^+$ decay mode. Since we do not have particle identification, we expect to observe the $B_u^+ \rightarrow J/\psi K^+$ decay mode on the $J/\psi\pi^+$ plot at lower mass than the B_u^+ mass because $M_{\pi^+} < M_{K^+}$.

A procedure to simultaneously fit the $J/\psi K^+$ and $J/\psi\pi^+$ decay modes will be described in Chapter 7. This will allow us to separate the $J/\psi\pi^+$ signal from the overlapping $J/\psi K^+$ signal.

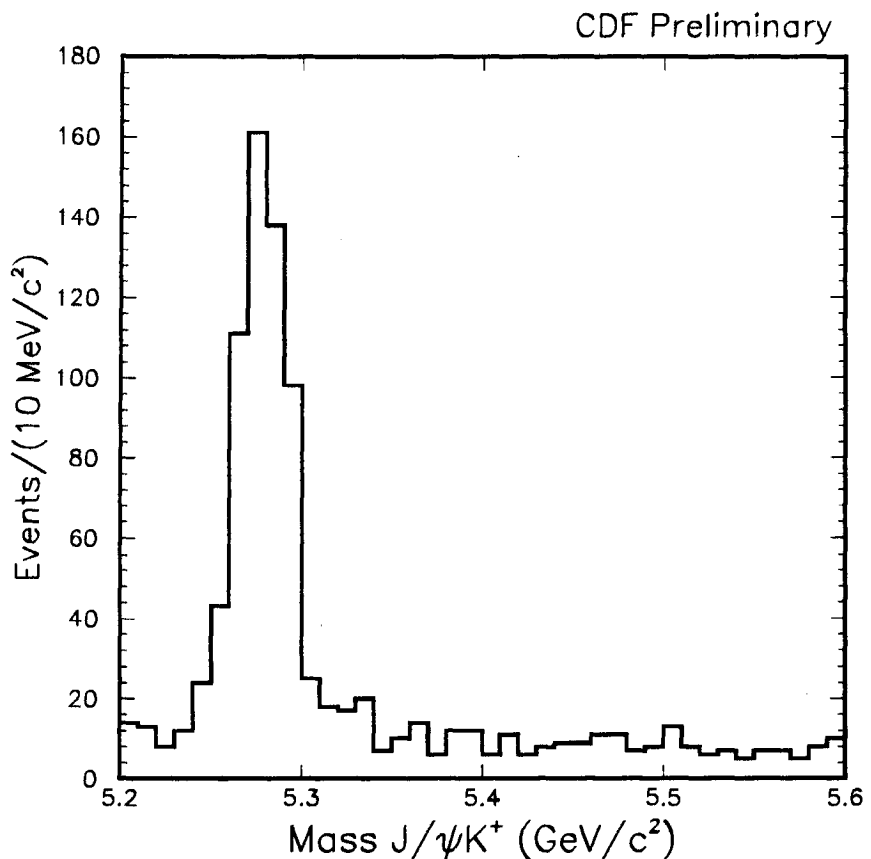


Figure 6.2: The figure shows the invariant mass distribution for events passing the selection criteria. The $B_u^+ \rightarrow J/\psi K^+$ mode is evident at the known B_u^+ mass of 5.2787 GeV/ c^2 .

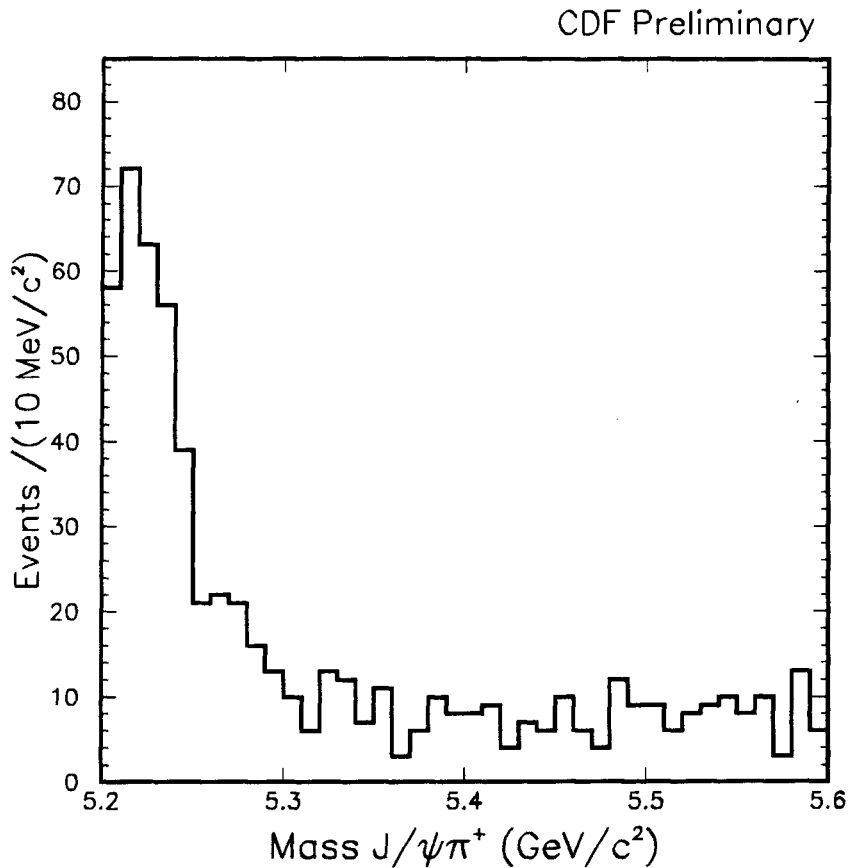


Figure 6.3: The figure shows the $J/\psi\pi^+$ invariant mass distribution for events passing the selection criteria. The $B_u^+ \rightarrow J/\psi K^+$ mode is present at the left edge of the plot. This is expected since the transformation from $M_{J/\psi K^+}$ to $M_{J/\psi\pi^+}$ necessarily yields a mass below the B_u^+ mass since $M_{\pi^+} < M_{K^+}$.

Chapter 7

Measurement of the Ratio of Branching Ratios

In this chapter we discuss the methods we employed to measure the ratio of branching ratios for $B_u^+ \rightarrow J/\psi\pi^+$ and $J/\psi K^+$. A fitting procedure to simultaneously fit the $J/\psi\pi^+$ and $J/\psi K^+$ signals is described. In addition, corrections for efficiencies and decay-in-flight are made.

7.1 Ratio of Branching Ratios Calculation

The absolute branching ratio for $B_u^+ \rightarrow J/\psi\pi^+$ is given by

$$\mathcal{B}(B_u^+ \rightarrow J/\psi\pi^+) = \frac{\frac{(\#J/\psi\pi^+ \text{ observed})}{\epsilon_{\text{trigger}} \epsilon_{\text{cuts}} \epsilon_{\text{dif}}}}{\#B_u^+ \text{ produced}}, \quad (7.1)$$

where $\epsilon_{\text{trigger}}$ is the efficiency of the trigger, ϵ_{cuts} is the efficiency of the cuts on events passing the trigger and ϵ_{dif} is the efficiency of reconstructing events for which the pion decays in flight.

To compare this with $B_u^+ \rightarrow J/\psi K^+$, we use the similar formula

$$\mathcal{B}(B_u^+ \rightarrow J/\psi K^+) = \frac{\frac{(\#J/\psi K^+ \text{ observed})}{\epsilon_{\text{trigger}} \epsilon_{\text{cuts}} \epsilon_{\text{dif}}}}{\#B_u^+ \text{ produced}}. \quad (7.2)$$

For the ratio of $B_u^+ \rightarrow J/\psi \pi^+$ to $B_u^+ \rightarrow J/\psi K^+$, we divide the above two branching ratios to get

$$\begin{aligned} \frac{\mathcal{B}(B_u^+ \rightarrow J/\psi \pi^+)}{\mathcal{B}(B_u^+ \rightarrow J/\psi K^+)} &= \left(\frac{(\#J/\psi \pi^+ \text{ observed})}{(\#J/\psi K^+ \text{ observed})} \right) \\ &\quad \cdot \left(\frac{\epsilon_{\text{trigger}}^{J/\psi K}}{\epsilon_{\text{trigger}}^{J/\psi \pi}} \cdot \frac{\epsilon_{\text{cuts}}^{J/\psi K}}{\epsilon_{\text{cuts}}^{J/\psi \pi}} \right) \left(\frac{\epsilon_{\text{dif}}^{J/\psi K}}{\epsilon_{\text{dif}}^{J/\psi \pi}} \right) \quad (7.3) \\ &= \frac{r_{\text{obs}}}{\epsilon_{\text{rel}} \mathcal{D}}. \quad (7.4) \end{aligned}$$

This is factored into three convenient quantities:

1. r_{obs} : The observed raw ratio of branching ratios in the data, $\frac{(\#J/\psi \pi^+ \text{ observed})}{(\#J/\psi K^+ \text{ observed})}$.
2. ϵ_{rel} : The relative efficiency of the two decay modes for passing the trigger and cuts, $\frac{\epsilon_{\text{trigger}}^{J/\psi K}}{\epsilon_{\text{trigger}}^{J/\psi \pi}} \cdot \frac{\epsilon_{\text{cuts}}^{J/\psi K}}{\epsilon_{\text{cuts}}^{J/\psi \pi}}$.
3. \mathcal{D} : The relative efficiency of reconstruction due to decay-in-flight, $\frac{\epsilon_{\text{dif}}^{J/\psi K}}{\epsilon_{\text{dif}}^{J/\psi \pi}}$.

By determining the above quantities, the ratios of branching ratios can be computed.

7.2 Maximum Likelihood Fit

Figure 6.3 in the previous chapter showed the difficulty in measuring the $B_u^+ \rightarrow J/\psi \pi^+$ mode since there is a large overlapping $J/\psi K^+$ signal. We have developed a maximum

likelihood function to fit the data. This fit will give us the observed ratio, r_{obs} , which is necessary to determine the ratio of branching ratios.

7.3 Fitting Region

We choose the fitting region to get the best possible fit to the data. First, we choose to parameterize our background as linear in $M_{J/\psi K^+}$ rather than $M_{J/\psi \pi^+}$. This choice gives us a normalizable region for our fit and a good handle on the $J/\psi K^+$ signal, since it is better behaved in $M_{J/\psi K^+}$ than $M_{J/\psi \pi^+}$ and it is a large fraction (62%) of the events in the fit. Second, we choose the lower limit fitting boundary, $ll = 5.2 \text{ GeV}/c^2$, in $M_{J/\psi K^+}$ to avoid long-lived backgrounds from partially reconstructed B mesons, which fall below the B meson's mass. Third, we choose the upper fitting boundary, $up = 5.6 \text{ GeV}/c^2$, to include a very large fraction (99.9%) of $B_u^+ \rightarrow J/\psi \pi^+$ events.

7.4 Likelihood Function

The likelihood function contains three terms, the $J/\psi K^+$ signal, the $J/\psi \pi^+$ signal and the linear background. The signal terms are represented by Gaussian distributions and the background, by a linear distribution. The likelihood function coefficients of the $J/\psi K^+$ and $J/\psi \pi^+$ signal terms ($\frac{1}{1+r_{\text{obs}}}$ and $\frac{r_{\text{obs}}}{1+r_{\text{obs}}}$, respectively) are proportional to the amount of each signal. Their ratio ($J/\psi \pi^+$ to $J/\psi K^+$), r_{obs} , is the observed ratio of branching ratios. The likelihood function for an event is given below.

$$\mathcal{L} = f_s \left(\frac{1}{1+r_{\text{obs}}} G(M_{\psi K^+}, M_{B^+}) + \frac{r_{\text{obs}}}{1+r_{\text{obs}}} G(M_{\psi \pi^+}, M_{B^+}) \frac{dM_{\psi \pi^+}}{dM_{\psi K^+}} \right) + (1 - f_s) Y_{\text{bkg}}, \quad (7.5)$$

where G is a Gaussian distribution and Y_{bkg} is a linear background normalized to unit area over the interval (ll, up) , where ll is the lower limit and up is the upper limit.

$$Y_{\text{bkg}} = m \left[M_{J/\psi K^+} - \frac{(up + ll)}{2} \right] + \frac{1}{up - ll}, \quad (7.6)$$

where m is the slope of the linear background. The term in brackets is chosen to integrate to zero over the fitting region.

$$\int_u^{up} Y_{\text{bkg}} dM_{J/\psi K^+} = 1 \quad (7.7)$$

The fitting parameters are

f_s - the fraction of signal events in the fit.

r_{obs} - the ratio of branching ratios.

M_{B^+} - the B_u^+ mass.

m - the slope of the linear background.

The term $\frac{dM_{\psi \pi^+}}{dM_{\psi K^+}}$ has been included to properly normalize the likelihood function.

$$\begin{aligned} \int_{ll}^{up} \mathcal{L} dM_{J/\psi K^+} &= \frac{f_s}{1 + r_{\text{obs}}} \int_{-\infty}^{\infty} G(M_{J/\psi K^+}, M_{B_u^+}) dM_{J/\psi K^+} \\ &\quad + \frac{f_s r_{\text{obs}}}{1 + r_{\text{obs}}} \int_{-\infty}^{\infty} G(M_{J/\psi \pi^+}, M_{B_u^+}) dM_{J/\psi \pi^+} \\ &\quad + (1 - f_s) \int_{ll}^{up} Y_{\text{bkg}} dM_{J/\psi K^+} \end{aligned} \quad (7.8)$$

$$= \frac{f_s}{1 + r_{\text{obs}}} + \frac{f_s r_{\text{obs}}}{1 + r_{\text{obs}}} + (1 - f_s) = 1, \quad (7.9)$$

where the limits over the Gaussian integrals have been converted to infinity. This makes the integral much simpler with little loss of accuracy. The $M_{J/\psi \pi^+}$ Gaussian shows some “leakage” over the upper boundary, $M_{J/\psi K^+} > up$, but this is less than a 1% effect.

7.5 Fit Testing

The likelihood fitting function has been tested using many independent Monte Carlo data samples. Data have been generated using a random number generator to determine the mass, the Lorentz boost β and θ , the decay angle in the B meson’s rest frame. The β distribution for the signal has been determined by parameterizing the Monte Carlo $\beta\gamma$ distribution. The β distribution for the background is taken from the data. The results of the fitting are summarized in Table 7.1 below.

Table 7.1 shows the excellent agreement of the fitted ratio of branching ratios with the input values. Figure 7.1 graphically shows the result.

N _{back}	N _{ψK}	N _{$\psi\pi$}	slope	$\langle f_s \rangle$	$f_s(\text{observed})$	$\langle r_{\text{obs}} \rangle (\%)$	$r_{\text{obs}}(\text{observed}) (\%)$
750	500	0	0	0.4	0.4006 ± 0.0005	0.0	0.026 ± 0.043
819	520	26	0	0.4	0.4006 ± 0.0005	5.0	5.044 ± 0.055
825	500	50	0	0.4	0.4001 ± 0.0005	10.0	9.942 ± 0.067
1500	1000	0	0	0.4	0.4001 ± 0.0004	0.0	-0.007 ± 0.031
1599	1040	26	0	0.4	0.3999 ± 0.0004	2.5	2.48 ± 0.03
1575	1000	50	0	0.4	0.4002 ± 0.0004	5.0	4.99 ± 0.04
1650	1000	100	0	0.4	0.4002 ± 0.0004	10.0	9.98 ± 0.05
750	500	0	-1	0.4	0.4006 ± 0.0006	0.0	0.12 ± 0.05
819	520	26	-1	0.4	0.4002 ± 0.0005	5.0	5.06 ± 0.05
825	500	50	-1	0.4	0.4007 ± 0.0005	10.0	10.04 ± 0.07
900	500	100	-1	0.4	0.3998 ± 0.0005	20.0	19.87 ± 0.09

Table 7.1: The table shows the results of a set of 1000 Monte Carlo tests with each set of input parameters. The ratio of branching ratios, r_{obs} , is reproduced well by the fitting procedure. The input parameters were chosen in different ranges, but with the desire to have a simple ratio for the final result.

Results of Fit Testing

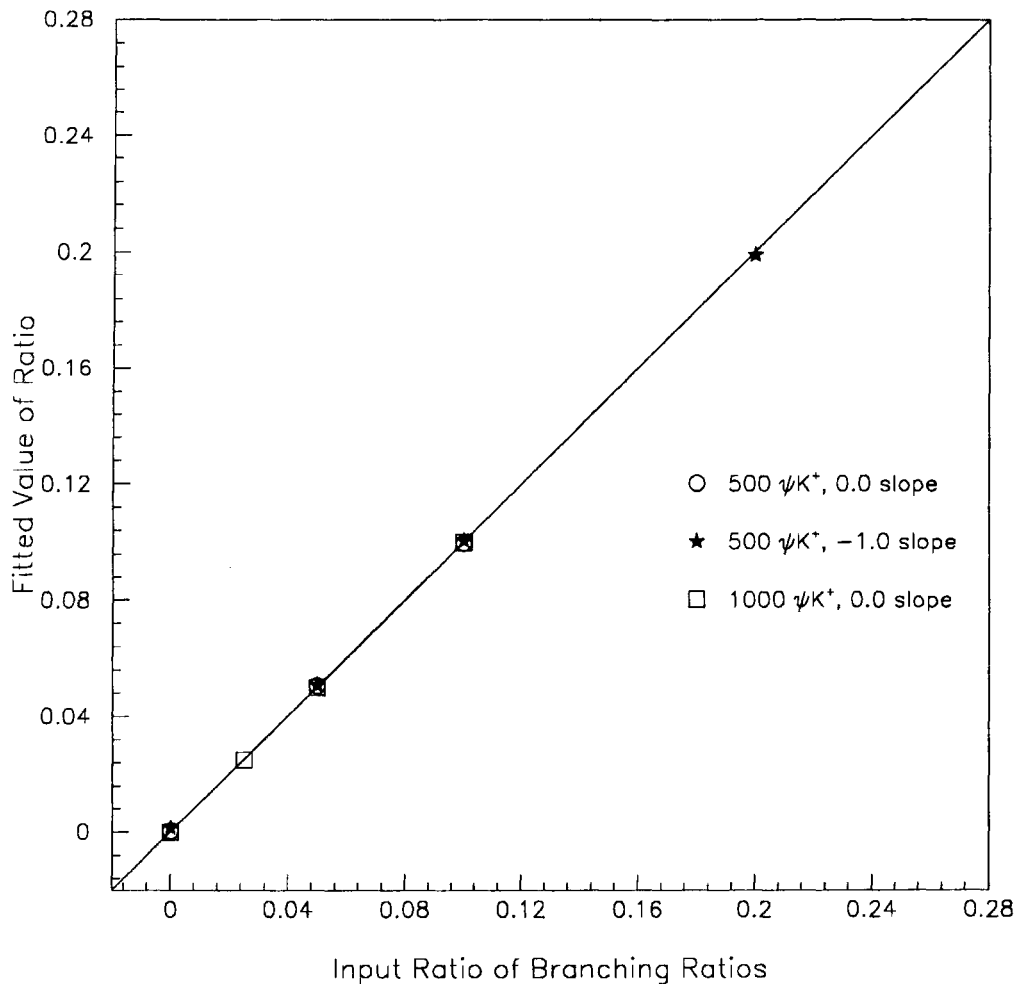


Figure 7.1: The figure shows the results of the fit testing. There are three categories of points, each with a different slope or background level.

Parameter	Value
f_s	0.62 ± 0.02
r_{obs}	$0.051^{+0.019}_{-0.017}$
$M_{B_u^+}$	5.2780 ± 0.0006
k_σ	1.23 ± 0.06
m	-2.6 ± 1.4

Table 7.2: The table displays the values of the fitting parameters that best represent the data.

7.6 Fit Results

The likelihood fitting method was applied to the data. We determine a signal fraction of 0.62 ± 0.02 for the 925 events we fit. The ratio of $J/\psi\pi^+$ to $J/\psi K^+$ is $5.1^{+1.9\%}_{-1.7\%}$. Our measured B_u^+ mass is 5.2780 ± 0.0006 GeV/ c^2 , which is consistent with the world average value of 5.2789 ± 0.0018 GeV/ c^2 [14]. The scale factor we use to correct the mass uncertainty, k_σ , is 1.23 ± 0.06 . The results of the fit are summarized in Table 7.2 below. The fit to the $J/\psi K^+$ mass plot is shown in Figure 7.2.

7.7 Cross Checks

Various cross-checks have been performed on the data. They are all concerned with checking that our signal events are not really $J/\psi K^+$ events.

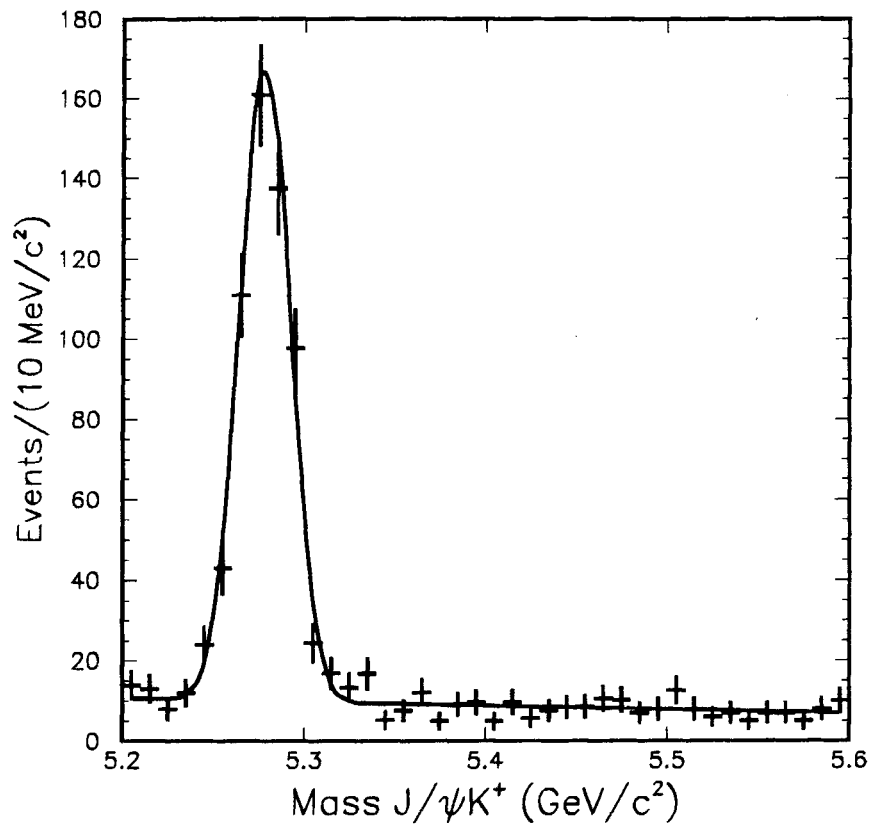


Figure 7.2: The figure shows the results of the fit to the $J/\psi K^+$ plot. The $B_u^+ \rightarrow J/\psi \pi^+$ events have been removed.

The first cross-check is a scatter plot of $M_{J/\psi K^+}$ vs. $M_{J/\psi \pi^+}$. This plot is shown in Figure 7.3. The plot shows that, although there is some overlap, which is expected, the majority of the events are far from the B_u^+ mass in $M_{J/\psi K^+}$.

The second check that was performed was to overlay the Monte Carlo mass distribution on the Data. Figure 7.4 shows the data with the Monte Carlo superimposed. The Monte Carlo distributions show $B_u^+ \rightarrow J/\psi K^+$ events, which have shifted to the left on the plot, and the background events. The dashed line shows the expected distribution when there are zero $B_u^+ \rightarrow J/\psi \pi^+$ events in the sample. The solid line shows the same distribution with the addition of 29 $J/\psi \pi^+$ events. The solid line, which includes the $B_u^+ \rightarrow J/\psi \pi^+$ events better represents and is consistent with the data.

An additional check is to consider all the events to be from B_u^+ decay and to find the mass of the third track. The B meson's four-momentum is found by adding the J/ψ 's and the third track's three-momentum,

$$\vec{P}_{J/\psi} + \vec{P}_3 = \vec{P}_B, \quad (7.10)$$

and then assuming the B_u^+ mass to find

$$P_B^0 = \sqrt{\vec{P}_B \cdot \vec{P}_B + M_B^2}. \quad (7.11)$$

Then the energy of the third track is determined by subtracting the J/ψ 's energy

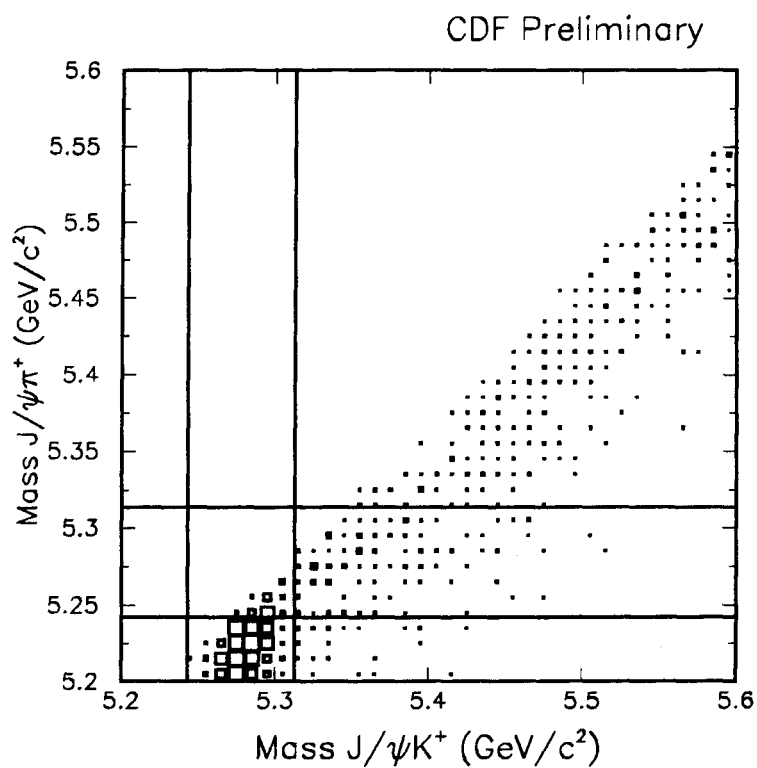


Figure 7.3: The figure shows a scatter plot of $M_{J/\psi K^+}$ vs. $M_{J/\psi \pi^+}$. The lines shown are the 2.5σ lines.

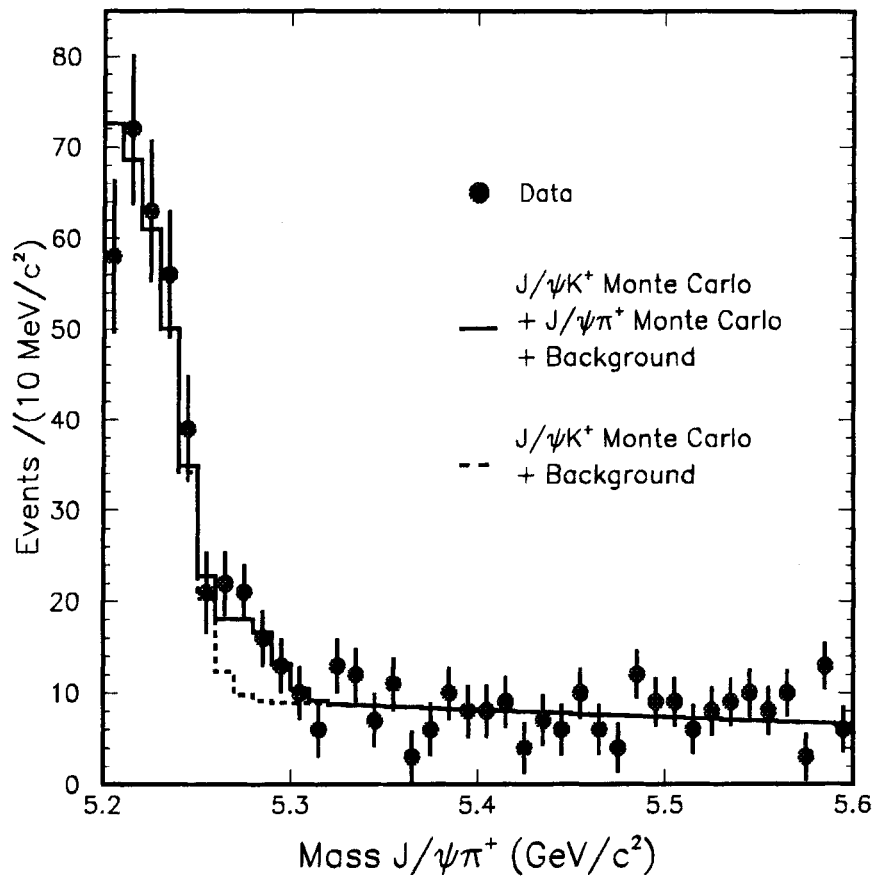


Figure 7.4: The figure shows the data with the Monte Carlo superimposed. The $J/\psi\pi^+$ events are not accounted for in the Monte Carlo background distribution shown as the dashed line. The solid line shows the same distribution with the addition of $B_u^+ \rightarrow J/\psi\pi^+$ events in the same proportion as we measure.

from the B 's.

$$P_3^0 = P_B^0 - P_{J/\psi}^0 \quad (7.12)$$

Squaring this recalculated four-vector gives the third track's mass.

$$M_3 = \sqrt{P_\mu P^\mu} \quad (7.13)$$

A plot of the third track mass vs. the $J/\psi\pi^+$ mass is shown in Figure 7.5.

7.8 Relative Efficiency Determination

In order to determine the true ratio of branching ratios, we must correct the measured ratio by the relative efficiency. Since the two modes are so similar, we expect the relative efficiency to be close to unity. We define this efficiency as

$$\epsilon_{\text{rel}} = \frac{\epsilon_{J/\psi\pi^+}(\text{cuts})\epsilon_{J/\psi\pi^+}(\text{trigger})}{\epsilon_{J/\psi K^+}(\text{cuts})\epsilon_{J/\psi K^+}(\text{trigger})}. \quad (7.14)$$

We expect the ratio to be near unity for two reasons. First, the mass of the pion is close to the kaon's, relative to the mass scale of the B_u^+ and J/ψ . The momentum of the J/ψ and the π^+ in the B_u^+ meson's rest frame is given by

$$P_{J/\psi} = P_{\pi^+} = \frac{(M_B^4 + M_{J/\psi}^4 + M_\pi^4 - 2M_B^2 M_{J/\psi}^2 - 2M_B^2 M_\pi^2 - 2M_{J/\psi}^2 M_\pi^2)^{\frac{1}{2}}}{2M_B} \quad (7.15)$$

$$= 1.727 \text{ GeV}/c^2. \quad (7.16)$$

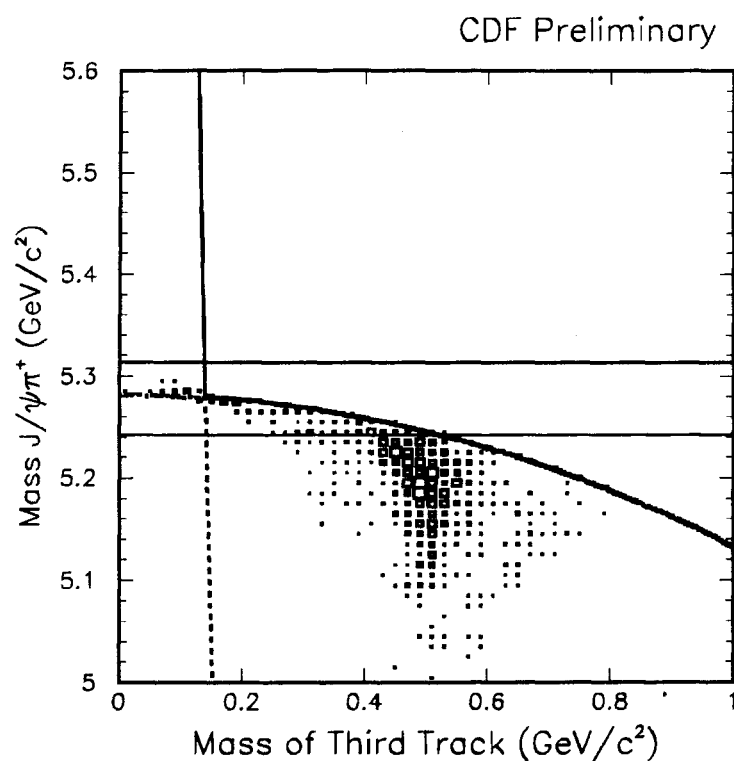


Figure 7.5: The figure shows the $J/\psi\pi^+$ mass vs. the third track's invariant mass. This mass is calculated by constraining the three tracks to form a B_u^+ .

By replacing the pion's mass with the kaon's,

$$P_{K^+} = 1.683 \text{ GeV}/c^2. \quad (7.17)$$

From the rest frame momenta, the ratio of average energies for the J/ψ is computed as

$$\frac{\langle E_{J/\psi}(J/\psi\pi^+) \rangle}{\langle E_{J/\psi}(J/\psi K^+) \rangle} = \frac{\sqrt{M_{J/\psi}^2 + P_{\pi^+}^2}}{\sqrt{M_{J/\psi}^2 + P_{K^+}^2}} = 1.006. \quad (7.18)$$

The second reason we expect the ratio to be similar is the fact that in both cases a spin 0 particle is decaying into a spin 1 J/ψ and a spin 0 light meson. This insures that the angular distributions will be the same.

To determine the relative efficiency, we generate a sample of B_u^+ mesons using the Herwig Monte Carlo generator[31]. The meson is allowed to decay by CLEOMC[32]. The relevant information, such as $P_T(B)$, $P_T(K^+)$ and L_{xy} , is recorded. The B_u^+ is then re-decayed as $J/\psi\pi^+$ with the same decay angle and boost. Again, the relevant information is recorded. This permits a more direct relative efficiency since these events are so highly correlated. The results are summarized in Table 7.3.

Using the observed ratio of $J/\psi K^+$ events from Run 1a and Run 1b, we combine the above results to get our overall efficiency.

$$\epsilon_{\text{rel}} = 0.997 \pm 0.002 \quad (7.19)$$

<i>B</i> 's Passing Cuts					
P_T (GeV/c)	$\epsilon_{\text{rel}}(1a)$	$\epsilon_{\text{rel}}(1b)$	1a(%)	1b(%)	% <i>B</i> 's in MC
5-6	1.048 ± 0.016	1.053 ± 0.012	8.2	5.2	16.0
6-7	1.027 ± 0.013	1.025 ± 0.010	11.0	8.3	15.1
7-8	1.030 ± 0.012	1.001 ± 0.006	12.2	10.2	13.7
8-9	0.999 ± 0.011	1.000 ± 0.005	12.2	10.8	11.8
9-10	0.985 ± 0.010	0.992 ± 0.004	11.3	10.9	9.8
10-12	0.988 ± 0.008	0.995 ± 0.003	17.8	19.6	14.3
12-14	0.991 ± 0.009	0.985 ± 0.004	11.8	14.3	8.7
14-900	0.975 ± 0.007	0.985 ± 0.003	15.5	20.9	10.7
overall	1.002 ± 0.004	0.996 ± 0.002	100.0	100.2	

Table 7.3: The table displays the relative efficiency as a function of $P_T(B)$. The events are grouped in 1 GeV/ c P_T bins, except for the last few bins. The fourth and fifth columns show the percentage of B_u^+ mesons passing the cuts that are in each bin. The last column shows the percentage of B_u^+ mesons in each bin before any cuts are applied.

7.9 Decay-in-Flight

Since there is over a factor of 2 difference in lifetime between the π^+ and K^+ and roughly 5% of kaons will decay within the CTC, the relative efficiency for reconstructing tracks needs to be considered.

$$\mathcal{D} = \frac{\epsilon_{\text{dif}}^{\pi^+}}{\epsilon_{\text{dif}}^{K^+}} \quad (7.20)$$

The efficiency of the two modes is determined separately. A track embedding program is used to embed Monte Carlo tracks in “*B*-like” data events, which have a secondary J/ψ vertex displaced from the primary such that

$$L_{xy} > 100 \mu m. \quad (7.21)$$

A sample of runs with a large range of luminosity was used to determine luminosity effects. The runs and luminosities are listed below.

The embedding program, written originally by Julio González[33], embeds the charged tracks and any charged daughters, if it decays within the CTC. A software switch allows the user to “turn-off” particle decay, giving the kaon and pion infinite lifetime.

The program finds “*B*-like” events with a J/ψ . A Monte Carlo $B_u^+ \rightarrow J/\psi K^+/\pi^+$ event is then generated. The Monte Carlo event is rotated so that its J/ψ is in the same direction as the data J/ψ . The rotated J/ψ is saved for later use. The K^+/π^+

Run #	$\langle \mathcal{L} \rangle (10^{30})$	$\int \mathcal{L} dt (nb^{-1})$
56121	2.85	20.5
60705	4.35	62.1
62865	7.73	82.4
65697	10.1	54.2

Table 7.4: The table displays the data runs used to determine the decay-in-flight correction. The average luminosity during the run, $\bar{\mathcal{L}}$, and the integrated luminosity, $\int \mathcal{L} dt$, are given.

is embedded using calls to CTADDH. After dropping the tracking banks, an attempt to reconstruct the tracks is made by TRCONTROL. The saved J/ψ is then added to the retracked K^+/π^+ candidates. The number of reconstructed K^+/π^+ is determined from a fit to the resulting B_u^+ peak.

The efficiency of reconstructing a track that traverses the CTC before decaying is assumed to be independent of particle type. This will especially be an accurate assumption for this analysis since the pion and kaon distributions are so similar. Therefore, we are only interested in the effect of decay-in-flight.

The efficiency is determined by comparing the number of tracks found when allowing decay according to the lifetime distribution with the number of tracks found for “infinite” lifetime particles. The efficiencies for pions from $J/\psi\pi^+$ and kaons from $J/\psi K^+$ decays are given below.

P_T (GeV/c)	$\epsilon(1a)$	$\epsilon(1b)$	\mathcal{D}
5-6	0.99 ± 0.01	0.94 ± 0.01	1.05 ± 0.01
6-7	0.96 ± 0.01	0.96 ± 0.01	1.00 ± 0.01
7-8	0.98 ± 0.01	0.97 ± 0.01	1.01 ± 0.01
8-9	0.98 ± 0.02	0.98 ± 0.01	1.00 ± 0.02
9-10	1.00 ± 0.02	0.95 ± 0.02	1.05 ± 0.03
10-12	1.00 ± 0.02	0.95 ± 0.02	1.05 ± 0.03
12-14	0.95 ± 0.02	0.96 ± 0.02	0.99 ± 0.03
14-900	0.99 ± 0.02	1.00 ± 0.02	0.99 ± 0.03

Table 7.5: The table displays the decay-in-flight efficiencies for Run-1a and Run-1b and the overall decay-in-flight correction factor.

The overall decay-in-flight correction is given by

$$\mathcal{D} = 1.028 \pm 0.005. \quad (7.22)$$

Figure 7.6 shows the overall decay-in-flight correction for $J/\psi K^+$ and Figure 7.7 shows the overall decay-in-flight correction for $J/\psi \pi^+$.

7.10 Ratio of Ratios Calculation

Applying the numbers determined above to equation 7.4, we determine the ratio of branching ratios.

$$\frac{\mathcal{B}(B_u^+ \rightarrow J/\psi \pi^+)}{\mathcal{B}(B_u^+ \rightarrow J/\psi K^+)} = \frac{r_{\text{obs}}}{\epsilon_{\text{rel}} \mathcal{D}} = \frac{5.1^{+1.9}_{-1.7}\%}{(0.997 \pm 0.002) \cdot (1.028 \pm 0.005)} = (5.0^{+1.9}_{-1.7})\% \quad (7.23)$$

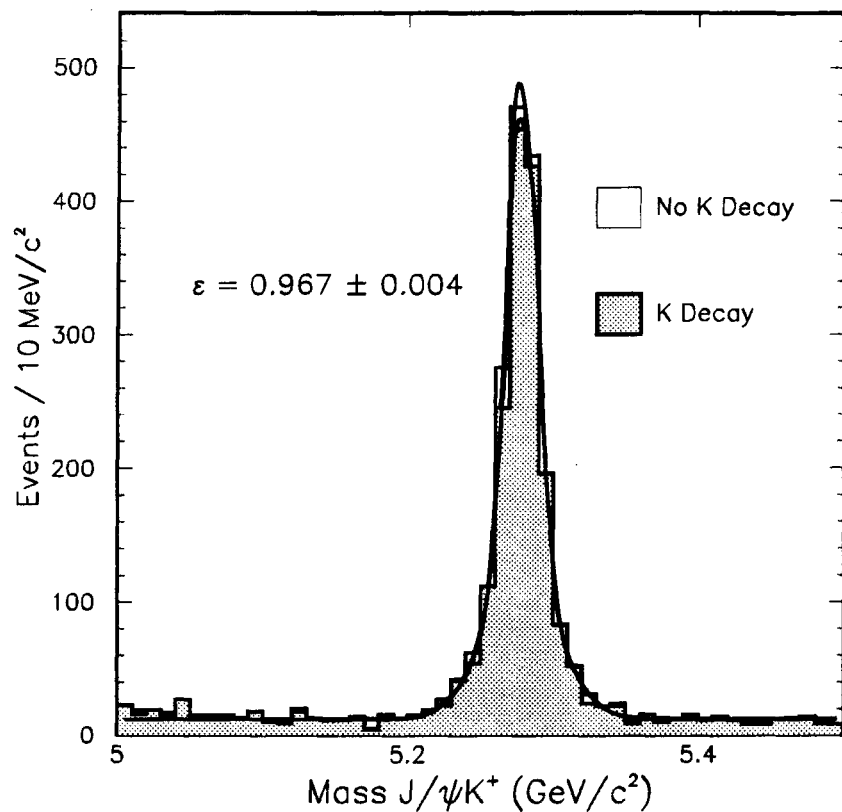


Figure 7.6: The figure shows the overall decay-in-flight correction for $J/\psi K^+$.

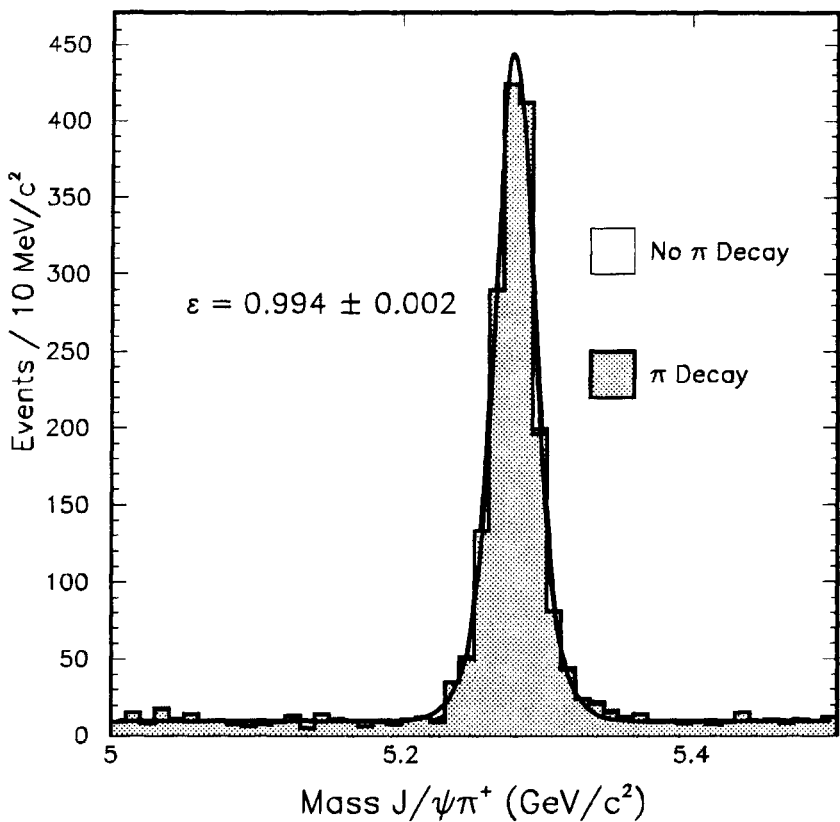


Figure 7.7: The figure shows the overall decay-in-flight correction for $J/\psi\pi^+$.

Chapter 8

B_c^+ Reconstruction

The B_c^+ meson is an undiscovered bound state of the bottom and charm quarks. It is predicted to exist by the standard model and have a mass of 6.256 ± 0.020 GeV/ c^2 [22] and a lifetime of 0.4–1.4 ps[21, 22]. This chapter will discuss our search for $B_c^+ \rightarrow J/\psi\pi^+$.

8.1 Backgrounds

There are two major backgrounds to the $B_c^+ \rightarrow J/\psi\pi^+$ decay mode. The first is partially or incorrectly reconstructed light B mesons which form a vertex with an unassociated charged track yet still pass the confidence level cut on the vertex. The second background is from prompt J/ψ mesons which form a vertex with a background track.

8.2 Techniques

We have developed several techniques to search for the B_c^+ meson. First, we developed two sets of cuts because of the wide range of predicted lifetimes. One set assumes the B_c^+ has zero lifetime and the other assumes it has the same lifetime as light B mesons. Another technique we have employed is to search for events with associated K_s^0 mesons. This is motivated by the B_c^+ meson's need to hadronize with a c -quark from the background sea. The \bar{c} -quark, partner of the c -quark in the B_c^+ , will typically hadronize as a D meson, which decays to a K_s^0 meson approximately 25% of the time.

8.3 $\pi^+ - \mu^+$ Angular Correlations

The spin structure of $B_c^+ \rightarrow J/\psi\pi^+$, $J/\psi \rightarrow \mu^+\mu^-$ gives useful information about the angular correlation between the μ^+ (or μ^-) and the π^+ . This correlation will be developed in two steps below. First, the spin 0 B_c^+ decay to the vector meson J/ψ and pseudoscalar meson π^+ will be considered. Second, the information obtained from the $B_c^+ \rightarrow J/\psi\pi^+$ analysis will be used in conjunction with quantum electrodynamics (QED) to determine the angular distribution of the μ^+ relative to the π^+ .

8.3.1 $B_c^+ \rightarrow J/\psi\pi^+$ Decay

The B_c^+ is a spin 0 particle. It decays to a spin 1 and a spin 0 particle. The spins of the J/ψ and π^+ couple

$$S_{J/\psi\pi^+} = S_{J/\psi} \oplus S_{\pi^+} = 1 \oplus 0 = 1, \quad (8.1)$$

where \oplus represents the addition of angular momentum for quantum particles. Angular momentum conservation requires the final state to have 0 angular momentum.

$$J_{J/\psi\pi^+} = S_{J/\psi\pi^+} \oplus L_{J/\psi\pi^+} = 1 \oplus L_{J/\psi\pi^+} = 0 \quad (8.2)$$

The only value for $L_{J/\psi\pi^+}$ that can satisfy this requirement is $L_{J/\psi\pi^+} = 1$.

We now define the \hat{z} -axis to be in the same direction as the J/ψ , as shown in Figure 8.1. From this diagram, it is clear that the \hat{z} -component of angular momentum is 0 since $\vec{L} = \vec{r} \times \vec{p}$ and $\vec{p} = p\hat{z}$. Therefore, the angular momentum of the J/ψ is in the state $|LM_L\rangle = |10\rangle$, relative to the π^+ . We also know that the \hat{z} -components of angular momenta add arithmetically, so

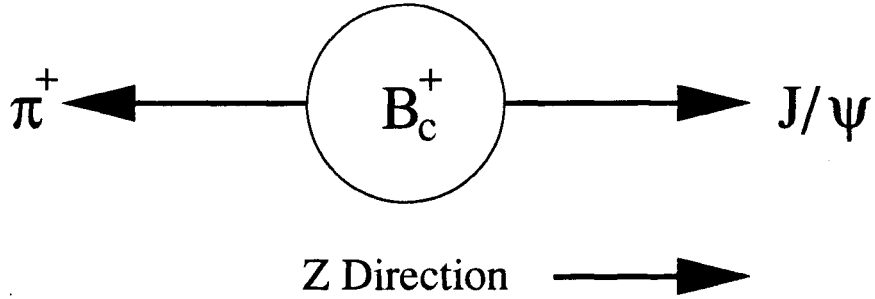


Figure 8.1: The diagram shows the $B_c^+ \rightarrow J/\psi\pi^+$ decay. The \hat{z} -axis is defined to be parallel to the J/ψ direction.

$$M_S(B_c^+) = M_S(J/\psi) + M_S(\pi^+) + M_L = M_S(J/\psi) + 0 + 0 = 0. \quad (8.3)$$

Therefore,

$$M_S(J/\psi) = 0. \quad (8.4)$$

8.3.2 J/ψ Decay

We now Lorentz boost the B_c^+ meson's rest system of Figure 8.1 along the \hat{z} -axis into the J/ψ 's rest frame. The spin state of the J/ψ is invariant under this transformation because the \hat{z} -component of angular momentum is unchanged. The reference frame we are interested in is diagrammed in Figure 8.2.

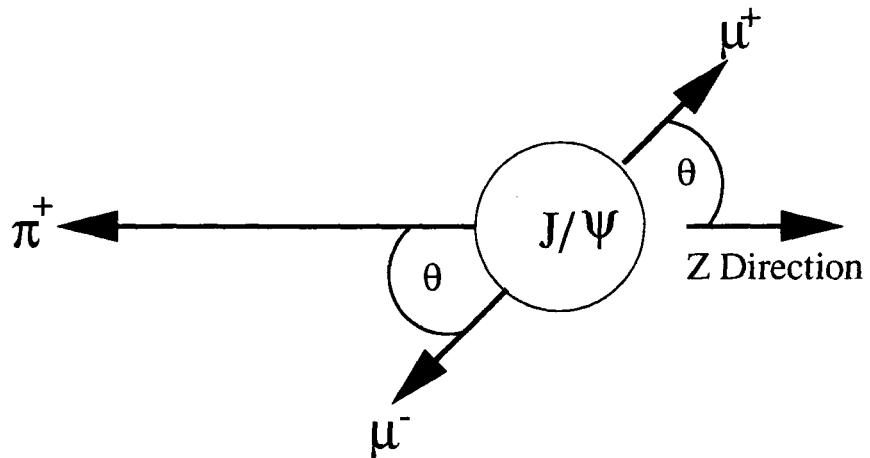


Figure 8.2: The diagram shows the $B_c^+ \rightarrow J/\psi \pi^+$ decay in the rest frame of the J/ψ . The \hat{z} -axis is defined to be parallel to the J/ψ meson's direction in the B_c^+ meson's rest frame and anti-parallel to the π^+ meson's direction in this rest frame.

We model the J/ψ decay as the pair-annihilation of $\bar{c}c$ into $\mu^+\mu^-$ in the context of QED, as shown in Figure 8.3. We constrain the spin state of the $\bar{c}c$ pair to be $|10\rangle$ by noting that for spin- $\frac{1}{2}$ particles

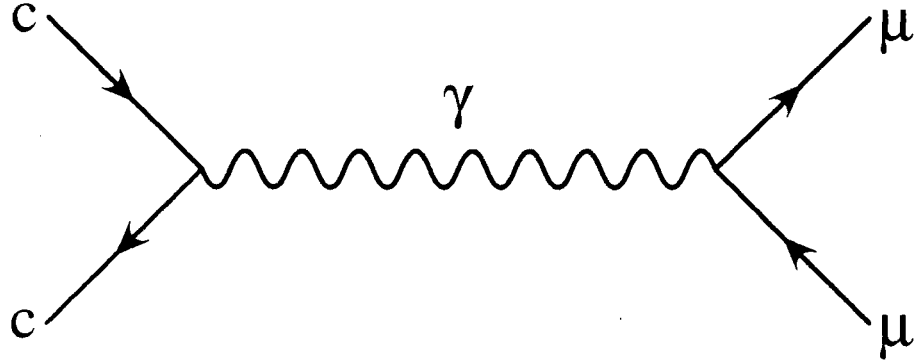


Figure 8.3: The diagram shows the Feynmann graph for the QED annihilation of $\bar{c}c$ in the J/ψ meson to $\mu^+\mu^-$.

$$|10\rangle = \frac{1}{\sqrt{2}}(|\uparrow\downarrow\rangle + |\downarrow\uparrow\rangle), \quad (8.5)$$

where \uparrow represents the “spin-up” state and \downarrow represents the “spin-down” state.

The matrix element for this process is[34]

$$\mathcal{M} = -\frac{\frac{2}{3}g_e^2}{(p_1 + p_2)^2} [\bar{u}(3)\gamma^\mu\nu(4)] [\bar{\nu}(2)\gamma_\mu u(1)], \quad (8.6)$$

where g_e is the dimensionless electro-magnetic coupling constant, u is the particle spinor and ν is the antiparticle spinor. The c and \bar{c} -quarks are numbered 1 and 2, respectively. The μ^- and μ^+ are labeled 3 and 4, respectively. The Dirac Matrices are represented by γ^μ .

For the $|\uparrow\downarrow\rangle$ case,

$$u(1) = \sqrt{2M_c c} \begin{pmatrix} 1 \\ 0 \\ 0 \\ 0 \end{pmatrix}, \bar{\nu}(2) = \sqrt{2M_c c} \begin{pmatrix} 0 & 0 & 1 & 0 \end{pmatrix}, \quad (8.7)$$

where M_c is the mass of the charm quark. Substituting this into equation 8.6,

$$\mathcal{M}_{\uparrow\downarrow} = \frac{4M_c g_e^2}{3(p_1 + p_2)^2} [\bar{u}(3)\Gamma^3\nu(4)]. \quad (8.8)$$

For the $|\downarrow\uparrow\rangle$ case,

$$u(1) = \sqrt{2M_c c} \begin{pmatrix} 0 \\ 1 \\ 0 \\ 0 \end{pmatrix}, \bar{\nu}(2) = -\sqrt{2M_c c} \begin{pmatrix} 0 & 0 & 0 & 1 \end{pmatrix}. \quad (8.9)$$

Substituting into equation 8.6,

$$\mathcal{M}_{\downarrow\uparrow} = \frac{4M_c g_e^2}{3(p_1 + p_2)^2} [\bar{u}(3)\Gamma^3\nu(4)] = \mathcal{M}_{\uparrow\downarrow} \quad (8.10)$$

$$\mathcal{M}_{10} = \frac{1}{2}(\mathcal{M}_{\uparrow\downarrow} + \mathcal{M}_{\downarrow\uparrow}) = \frac{4M_c g_e^2}{3(p_1 + p_2)^2} [\bar{u}(3)\Gamma^3\nu(4)]. \quad (8.11)$$

Evaluating the expectation value of the square of the matrix element, we find

$$\langle |\mathcal{M}_{10}|^2 \rangle \propto M_\mu^2 c^2 + p^2 \sin^2 \theta \approx p^2 \sin^2 \theta, \quad (8.12)$$

where the last approximation was used since

$$2\sqrt{p^2 + M_\mu^2 c^2} = M_{J/\psi} c \quad (8.13)$$

$$p \approx 1.54 \text{ GeV}/c \quad (8.14)$$

$$M_\mu c \approx 0.106 \text{ GeV}/c. \quad (8.15)$$

This gives a decay rate relative to the \hat{z} -axis (or the π^+ -direction)

$$\frac{d\Gamma}{d \cos \theta} \propto \sin^2 \theta. \quad (8.16)$$

Appendix D details this calculation.

8.3.3 Optimization of Helicity Angle Selection

We optimize our selection criteria on the helicity angle by optimizing our estimate of $\frac{S^2}{S+N}$, where S and N are our estimates of the signal and background, respectively.

By including the helicity angles in the interval $|\cos \theta| < \lambda$, we find

$$S = \frac{3}{2} N_S \int_0^\lambda (1 - \cos^2 \theta) d \cos \theta = \frac{3}{2} N_S \left(\lambda - \frac{\lambda^3}{3} \right) \quad (8.17)$$

and

$$N = N_B \int_0^\lambda d \cos \theta = N_B \lambda, \quad (8.18)$$

where N_S and N_B are the number of signal and background events, respectively, without the imposition of this criteria.

$$F \equiv \frac{S^2}{S + N} = \frac{N_S^2 \lambda^2 (3 - \lambda^2)^2}{2N_S \lambda (3 - \lambda^2) + 4N_B \lambda} \quad (8.19)$$

When we differentiate this equation with respect to λ and solve for the maximum we find the equation

$$3(1 - \lambda^2)[2N_S(3 - \lambda^2) + 4N_B] - (3 - \lambda^2)[3N_S(1 - \lambda^2) + 2N_B] = 0. \quad (8.20)$$

Solving this for λ^2 , we find

$$\lambda^2 = \frac{12N_S + 10N_B \pm \sqrt{(12N_S + 10N_B)^2 - 12N_S(9N_S + 6N_B)}}{6N_S}. \quad (8.21)$$

We estimate values for N_S and N_B of 5 and 15, respectively, and determine

$$\lambda^2 = 0.68, \quad (8.22)$$

$$\lambda = 0.82, \quad (8.23)$$

which is 95% efficient for the signal, but only 82% efficient for the background.

We combine this selection criteria with the others listed below to search for the B_c^+ meson.

8.4 Standard Cuts

The two sets of cuts we use below differ on their assumption of B_c^+ meson lifetime.

The first set are cuts optimized for finding a zero lifetime B_c^+ . The second set are optimized for finding a B_c^+ meson with the same lifetime as the light B mesons.

Zero-lifetime B_c^+ cuts

- $P_T(B_c^+) > 10.0 \text{ GeV}/c$
- $P_T(\pi^+) > 2.5 \text{ GeV}/c$
- $|\cos\theta| < 0.82$
- $c\tau > 0 \mu\text{m}$
- 2 or more ‘SVX’ tracks

Long-lived B_c^+ cuts

- $P_T(B_c^+) > 6.0 \text{ GeV}/c$
- $P_T(\pi^+) > 2.5 \text{ GeV}/c$
- $|\cos\theta| < 0.82$

- $c\tau > 150 \mu\text{m}$
- 2 or more ‘SVX’ tracks

We use the Lorentz-invariant quantity $c\tau$ to separate B_c^+ mesons from prompt backgrounds because of its convenience for determining the efficiency as a function of B_c^+ lifetime.

Figure 8.4 shows the $J/\psi\pi^+$ invariant mass plot for the zero lifetime selection and Figure 8.5 shows the same region for the long-lived B_c^+ selection. Neither plot suggests a signal for B_c^+ .

8.5 Associated K_s^0 Events

The production of the B_c^+ requires the hadronization of the \bar{b} -quark, which is produced by the $\bar{p}p$ interaction, with a c -quark. Since $\bar{c}c$ must be produced in pairs, there is a \bar{c} -quark in the event, other than the c -quark in the B_c^+ . We therefore search for B events with associated K_s^0 mesons because of the large branching fraction for the \bar{c} -quark to decay into K_s^0 . We look for K_s^0 mesons that pass the following criteria:

- $\frac{\delta(\pi^\pm)}{\sigma(\delta)} > 1.0$
- $L_{xy} > 0.5 \text{ cm}$
- $P_T(\pi^\pm) > 0.5 \text{ GeV}/c$
- $P_T(\pi^+\pi^-) > 1.0 \text{ GeV}/c$

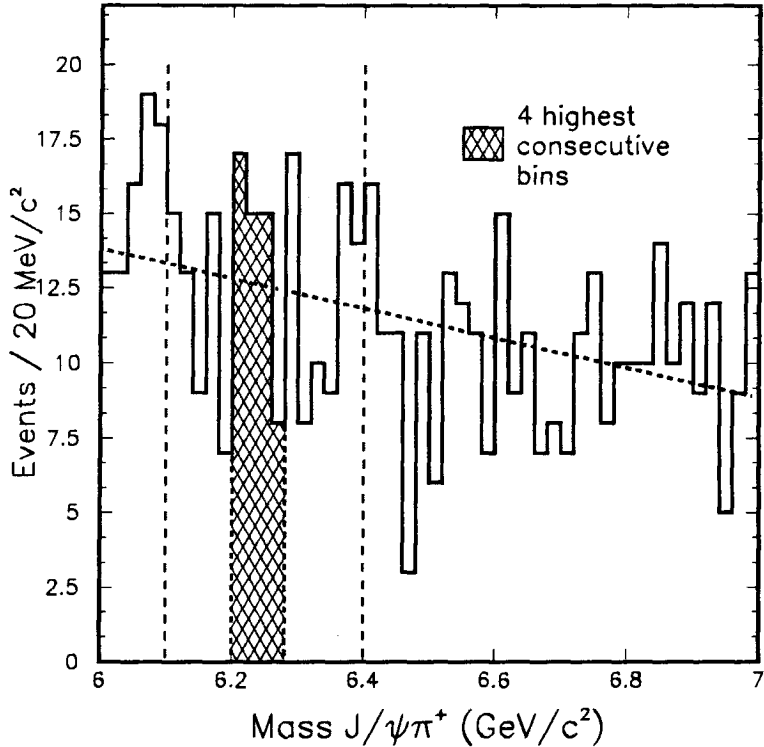


Figure 8.4: The plot shows the $J/\psi\pi^+$ invariant mass distribution over the B_c^+ signal region. The cuts used on this plot assume that the B_c^+ has zero lifetime.

- $|M_{\pi^+\pi^-} - M_{K_s^0}| < 15 \text{ MeV}/c^2$

The above cuts yield a K_s^0 signal of 2400 ± 100 events in the dimuon data set. The K_s^0 mesons have a signal-to-noise ratio of 0.6. The $\pi^+\pi^-$ invariant mass distribution is shown in Figure 8.6.

In addition, we modify the cuts on the B_c^+ candidates. We add a requirement that the angle between the reconstructed B_c^+ candidate and the K_s^0 candidate must be less than 90° , since we expect that the \bar{c} -quark that yields the K_s^0 would be in the

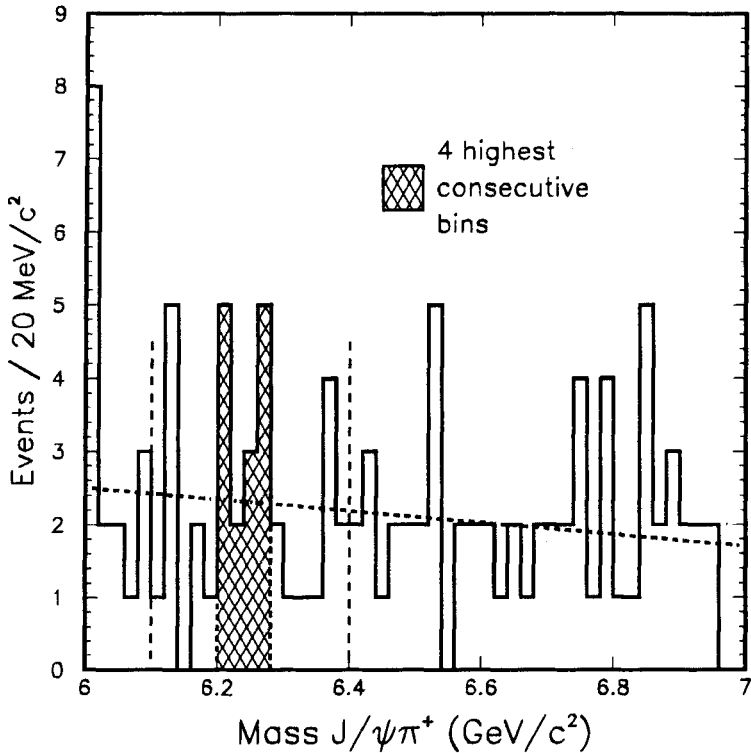


Figure 8.5: The plot shows the $J/\psi\pi^+$ invariant mass distribution over the B_c^+ signal region. The cuts used on this plot assume that the B_c^+ has a lifetime equal to B_u^+ .

same hemisphere as the B_c^+ . We also loosen the rest of the cuts from the long-lived analysis. The resulting cuts are:

- $P_T(B_c^+) > 5.0 \text{ GeV}/c$
- $P_T(\pi^+) > 2.0 \text{ GeV}/c$
- $|\cos \theta| < 0.82$
- $c\tau > 100 \mu\text{m}$

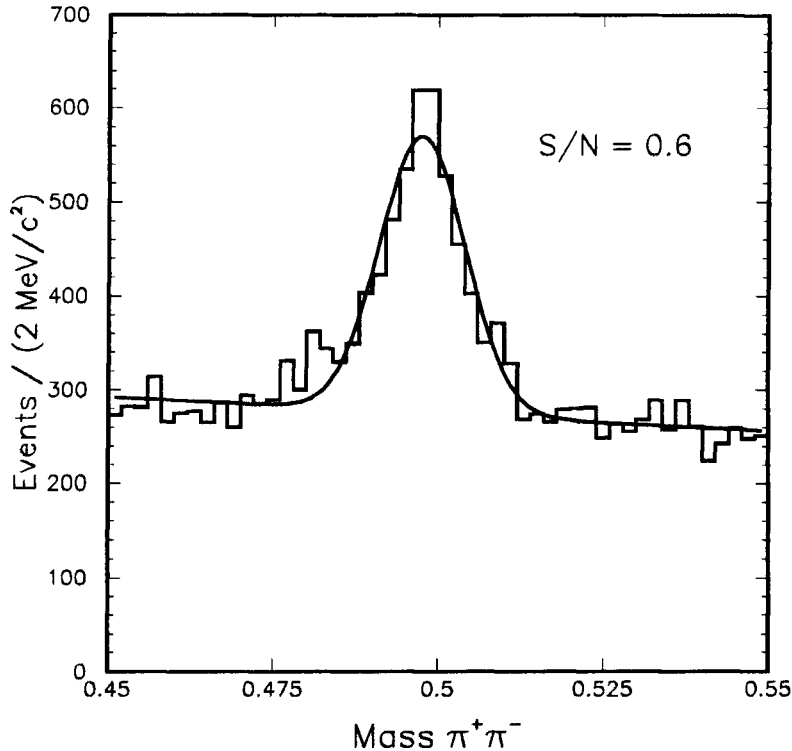


Figure 8.6: The plot shows the $\pi^+\pi^-$ invariant mass distribution over the K_s^0 signal region for events consistent with having a B meson. There are 2400 ± 100 K_s^0 candidates with a signal-to-noise ratio of 0.6.

- 2 or more ‘SVX’ tracks

- $\cos \alpha > 0$

where α is the angle between the reconstructed B_c^+ meson candidate and K_s^0 meson candidate. Figure 8.7 shows the $J/\psi\pi^+$ invariant mass plot for the associated K_s^0 events. There is no apparent B_c^+ signal.

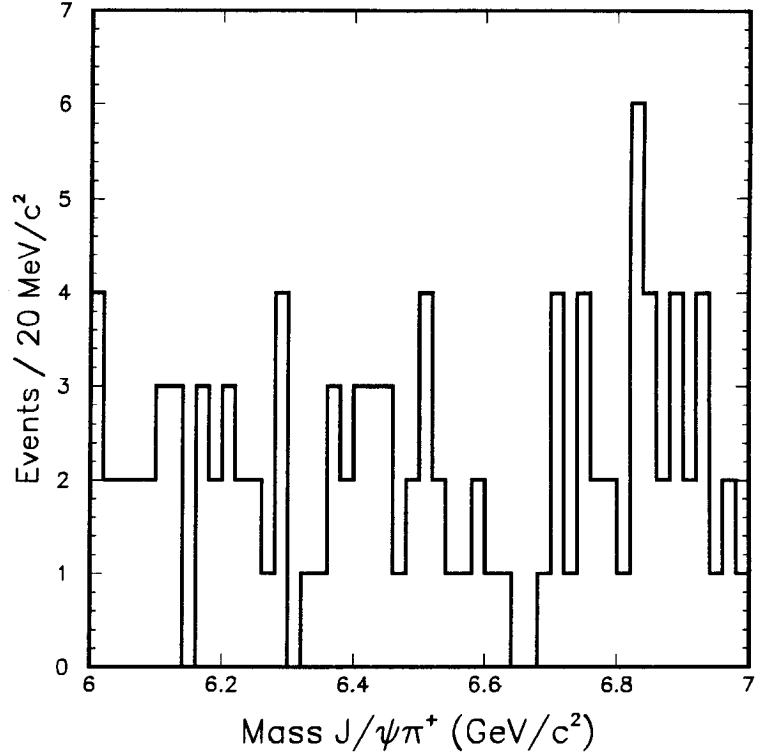


Figure 8.7: The plot shows the $J/\psi\pi^+$ invariant mass distribution over the B_c^+ signal region. These events require an associated K_s^0 meson candidate in the event. There is no apparent B_c^+ signal in this plot.

8.6 Limit Formulation

We calculate a limit on B_c^+ production in the form

$$r = \frac{\sigma(B_c^+) \cdot \mathcal{B}(B_c^+ \rightarrow J/\psi\pi^+)}{\sigma(B_u^+) \cdot \mathcal{B}(B_u^+ \rightarrow J/\psi K^+)} \quad (8.24)$$

We choose this ratio because the relative cross sections are unknown and systematic uncertainties on efficiencies are reduced. We use both sets of standard cuts to set an

upper limit. We will then determine the limit as a function of lifetime for the range (0,2 ps).

The above ratio can be rewritten as

$$r = \frac{(\#B_c^+ \rightarrow J/\psi\pi^+ \text{events})}{(\#B_u^+ \rightarrow J/\psi K^+ \text{events})} / (\epsilon_{\text{rel}} \cdot \mathcal{D}_{\text{rel}}), \quad (8.25)$$

where ϵ_{rel} and \mathcal{D}_{rel} are the relative efficiency and decay-in-flight correction, respectively. The number of $B_u^+ \rightarrow J/\psi K^+$ events, ϵ_{rel} and \mathcal{D}_{rel} are well-defined quantities. However, the number of $B_c^+ \rightarrow J/\psi\pi^+$ events is unknown.

The upper limit on a signal s with background b for N total events is[35]

$$CL = 1 - \frac{\sum_{n=0}^N \int G(b) P(n, s+b) db}{\sum_{n_b=0}^N \int G(b) P(n_b, b) db}, \quad (8.26)$$

where CL is the desired confidence level, $P(n, \mu)$ is the Poisson distribution with the expected value μ , b is the background estimate and $G(b)$ is a Gaussian distribution of the background with its estimated uncertainty.

We note that

$$s = N_{J/\psi K} \epsilon_{\text{rel}} \mathcal{D}_{\text{rel}} r. \quad (8.27)$$

Therefore, we generalize equation 8.26 to include uncertainties on $N_{J/\psi K}$, ϵ_{rel} and \mathcal{D}_{rel} .

$$CL = 1 - \frac{\sum_{n=0}^N \int G(b)G(N_{\psi K})G(\epsilon_{\text{rel}})G(\mathcal{D}_{\text{rel}})P(n, N_{\psi K}\epsilon_{\text{rel}}\mathcal{D}_{\text{rel}}r + b)d\mathcal{D}_{\text{rel}}d\epsilon_{\text{rel}}dN_{\psi K}db}{\sum_{n_b=0}^N \int G(b)P(n_b, b)db} \quad (8.28)$$

We now estimate the background and efficiencies so that we may determine the upper limit.

8.7 B_c^+ Width

The B_c^+ width is determined from the data. The mass uncertainty in the B_c^+ signal region of 6.2–6.3 GeV/ c^2 is compared to the mass uncertainty for $B_u^+ \rightarrow J/\psi K^+$ events. The B_c^+ width is estimated to be

$$\sigma_{B_c^+} = \sigma_{B_u^+} \frac{\Sigma_{B_c^+}}{\Sigma_{B_u^+}}, \quad (8.29)$$

where $\Sigma_{B_c^+}$ and $\Sigma_{B_u^+}$ are the average mass uncertainties in the B_c^+ and B_u^+ signal regions, respectively.

From the data, we estimate the mass uncertainty of the B_c^+ to be

$$\sigma_{B_c^+} = (14 \text{ MeV}/c^2) \frac{0.018 \text{ MeV}/c^2}{0.011 \text{ MeV}/c^2} = 23 \text{ MeV}/c^2. \quad (8.30)$$

8.8 B_c^+ Search Region

We define the B_c^+ search region to be ± 150 MeV/ c^2 around the predicted mass[22]. Based on an estimated width of 23 MeV/ c^2 , we assume the entire B_c^+ signal is contained within 7 bins of width 20 MeV/ c^2 . The 4 highest consecutive bins contain 1.5σ of the expected peak (87% of the events) and are used to determine the signal upper limit based on a background estimate from the remaining bins in the signal region. The four highest bins in the B_c^+ search region for the zero-lifetime plot contain 55 events. The background for this has been estimated to be 51 ± 2 . The four highest bins in the long-lived plot contain 15 events with an estimated background of 9.2 ± 2.0 events.

8.9 $B_u^+ \rightarrow J/\psi K^+$ Reference Signal

The $B_u^+ \rightarrow J/\psi K^+$ is used as a reference signal for the $B_c^+ \rightarrow J/\psi \pi^+$ search. By using the $J/\psi K^+$ signal, we can create ratios, which reduce systematic uncertainties. Since we do not know the B_c^+ lifetime, we modify the selection criteria on B_u^+ events to use a Lorentz-invariant lifetime cut rather than a decay distance cut. We also remove the impact parameter criteria. The selection criteria are listed below.

- $P_T(B_u^+) > 5.0$ GeV/ c
- $P_T(K^+) > 1.25$ GeV/ c

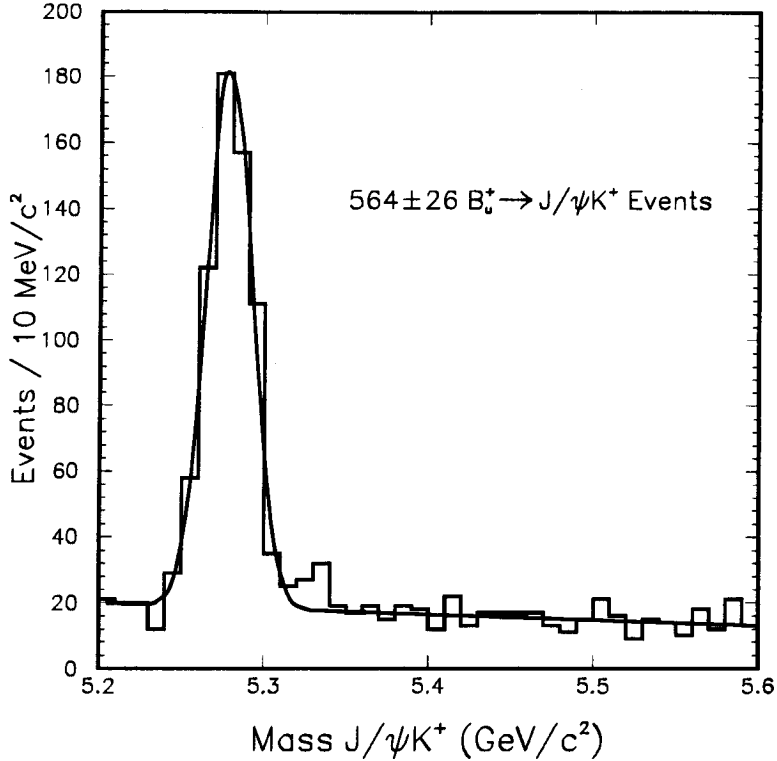


Figure 8.8: The figure shows the $B_u^+ \rightarrow J/\psi K^+$ mass distribution for events used as a reference signal to the B_c^+ signal.

- $c\tau > 150 \mu m$.

Figure 8.8 shows the resulting mass distribution. There are 564 ± 26 $B_u^+ \rightarrow J/\psi K^+$ events in the plot. This number is used in the calculation of the limit.

8.10 Relative Efficiency

The relative efficiency is determined by a Monte Carlo model of B_c^+ and B_u^+ decays. Events are generated for both B_c^+ and B_u^+ . The fraction of events that pass the

selection criteria is taken to be the efficiency. The relative efficiency is determined by dividing the two efficiencies,

$$\epsilon_{\text{rel}} = \frac{\epsilon_{B_c^+}}{\epsilon_{B_u^+}}. \quad (8.31)$$

We determine the relative efficiency from a Monte Carlo model[31]. We place a preliminary cut of $P_T(B) > 4.0 \text{ GeV}/c$. We also assume that the fractions of B_c^+ and B_u^+ events that pass this criteria are equal. The efficiencies given are for events with $P_T(B) > 4.0 \text{ GeV}/c$.

We find 1,269,468 B_c^+ events and B_u^+ events. Table 8.1 shows the $P_T(B)$ -spectrum of events passing the cuts. We found 177,817 events that passed the long-lived B_c^+ cuts and 108,350 events passed the zero-lifetime B_c^+ cuts, where the number of events passing the cut does not include the effect of the lifetime cut, which will be determined later.

$$\epsilon_{B_c^+}(\text{long - lived}) = \frac{177,817}{1,269,468} = 0.1401 \pm 0.0003 \quad (8.32)$$

$$\epsilon_{B_c^+}(\text{zero - lifetime}) = \frac{108,350}{1,269,468} = 0.0854 \pm 0.0002 \quad (8.33)$$

$$\epsilon_{B_u^+} = \frac{22,421}{119,351} = 0.1879 \pm 0.0011, \quad (8.34)$$

where the uncertainties are statistical only.

$P_T(B)$	# B_c^+ Passing Cuts	# B_u^+ Passing Cuts
5–6	8671	1429
6–7	12750	2102
7–8	16666	2422
8–9	18017	2467
9–10	17881	2397
10–11	16237	2266
11–12	14356	1910
12–13	12226	1528
13–14	10331	1366
14–15	8491	1013
15–900	46709	3037
All	186488	22421
Original Sample	1269468	119351

Table 8.1: The table displays the number of B_c^+ and B_u^+ Monte Carlo events that pass the selection criteria as a function of $P_T(B)$. The B_c^+ cuts require $P_T(B_c^+) > 6.0$ GeV/ c , but the 5.0–6.0 GeV/ c range is shown for comparison with B_u^+ .

We have measured the $c\tau$ resolution for B events by taking a sample of three-track events with a $J/\psi \rightarrow \mu^+ \mu^-$ and at least two SVX tracks with $5.4 \text{ GeV}/c^2 < M_{J/\psi K^+} < 5.6 \text{ GeV}/c^2$ and fitting it with a Gaussian distribution. The $c\tau$ resolution is measured to be $47 \text{ }\mu\text{m}$.

The observed $c\tau$ -distribution of long-lived events is given by the exponential decay distribution, convolved with a Gaussian resolution distribution. The probability density, P , of observing an event with $c\tau_{\text{obs}}$ for decays with lifetime τ and a detector $c\tau$ resolution of σ is given by

$$P(c\tau_{\text{obs}}) = \int_{ct=0}^{ct=\infty} (\text{Probability of an event with proper decay distance } ct) d(ct) \quad (8.35)$$

$$\times (\text{Probability of observing } c\tau_{\text{obs}} \text{ given } ct) d(ct) \quad (8.36)$$

$$= \int_{ct=0}^{ct=\infty} \frac{\exp\left(-\frac{ct}{c\tau}\right)}{c\tau} \frac{\exp\left[-\frac{(ct-c\tau_{\text{obs}})^2}{2\sigma^2}\right]}{\sqrt{2\pi}\sigma} d(ct) \quad (8.37)$$

$$= \frac{\exp\left(-\frac{(c\tau_{\text{obs}})^2}{2\sigma^2}\right)}{\sqrt{2\pi}\sigma c\tau} \int_{ct=0}^{ct=\infty} \exp\left(-\frac{ct}{c\tau} - \frac{(ct)^2}{2\sigma^2} + \frac{2ctc\tau_{\text{obs}}}{2\sigma^2}\right) d(ct) \quad (8.38)$$

$$= \frac{\exp\left(\frac{(\sigma^2 - c\tau_{\text{obs}}c\tau)^2}{2\sigma^2(c\tau)^2} - \frac{(c\tau_{\text{obs}})^2}{2\sigma^2}\right)}{\sqrt{2\pi}\sigma c\tau} \int_{ct=0}^{ct=\infty} \exp\left[-\frac{\left(ct + \frac{\sigma^2 - c\tau_{\text{obs}}c\tau}{c\tau}\right)^2}{2\sigma^2}\right] d(ct) \quad (8.39)$$

$$= \frac{\exp\left(\frac{\sigma^2 - 2c\tau c\tau_{\text{obs}}}{2(c\tau)^2}\right)}{\sqrt{\pi}c\tau} \int_{v=\frac{\sigma}{\sqrt{2}c\tau} - \frac{c\tau_{\text{obs}}}{\sqrt{2}\sigma}}^{\infty} e^{-v^2} dv \quad (8.40)$$

$$= \frac{\exp\left(\frac{\sigma^2 - 2c\tau c\tau_{\text{obs}}}{2(c\tau)^2}\right)}{2c\tau} \frac{2}{\sqrt{\pi}} \left[\int_{v=0}^{v=\infty} e^{-v^2} dv - \int_{v=0}^{v=\frac{\sigma}{\sqrt{2}c\tau} - \frac{c\tau_{\text{obs}}}{\sqrt{2}\sigma}} e^{-v^2} dv \right] \quad (8.41)$$

$$= \frac{\exp\left(\frac{\sigma^2 - 2c\tau c\tau_{\text{obs}}}{2(c\tau)^2}\right)}{2c\tau} \left[1 - \frac{2}{\sqrt{\pi}} \int_{v=0}^{v=\frac{\sigma}{\sqrt{2}c\tau} - \frac{c\tau_{\text{obs}}}{\sqrt{2}\sigma}} e^{-v^2} dv \right] \quad (8.42)$$

$$= \frac{\exp\left(\frac{\sigma^2 - 2c\tau c\tau_{\text{obs}}}{2(c\tau)^2}\right)}{2c\tau} \left[1 - \text{erf}\left(\frac{\sigma}{\sqrt{2}c\tau} - \frac{c\tau_{\text{obs}}}{\sqrt{2}\sigma}\right) \right], \quad (8.43)$$

where $\text{erf}(x) = \frac{2}{\sqrt{\pi}} \int_{x'=0}^{x'=x} e^{-x'^2} dx'$ is the error function and the substitution $v = \frac{1}{\sqrt{2}\sigma} (ct + \frac{\sigma^2 - c\tau_{\text{obs}}c\tau}{c\tau})$ was used.

The measured lifetime of the B_u^+ of $\tau(B_u^+) = 1.62 \pm 0.06$ ps[14] gives an efficiency for an event to pass the $c\tau$ selection of

$$\epsilon_{B_u^+}(\text{lifetime}) = 0.737 \pm 0.008. \quad (8.44)$$

B_c^+ mesons with the same lifetime would have the identical efficiency. For zero-lifetime B_c^+ mesons, the efficiency of the lifetime cut of $c\tau > 0$ μm is determined by the resolution. Half of the mesons will pass the cut. Therefore, the two relative efficiencies are

$$\begin{aligned} \epsilon_{\text{rel}}(\text{long-lived}) &= \frac{\epsilon_{B_c^+}(\text{long-lived})}{\epsilon_{B_u^+}} \frac{\epsilon_{B_c^+}(\text{lifetime})}{\epsilon_{B_u^+}(\text{lifetime})} \\ &= \frac{0.1401 \pm 0.0003}{0.1879 \pm 0.0011} \cdot 1 = 0.746 \pm 0.003 \end{aligned} \quad (8.45)$$

and

$$\begin{aligned} \epsilon_{\text{rel}}(\text{zero-lifetime}) &= \frac{\epsilon_{B_c^+}(\text{zero-lifetime})}{\epsilon_{B_u^+}} \frac{\epsilon_{B_c^+}(\text{lifetime})}{\epsilon_{B_u^+}(\text{lifetime})} \\ &= \frac{0.0854 \pm 0.0002}{0.1879 \pm 0.0011} \cdot \frac{0.5}{0.963} \\ &= 0.236 \pm 0.002, \end{aligned} \quad (8.46)$$

where the efficiency for the B_u^+ to pass the $c\tau > 0$ cut is 0.963 ± 0.001 .

8.11 Decay-in-Flight Correction

The kaon decay from $B_u^+ \rightarrow J/\psi K^+$ events is the dominant decay-in-flight component. The pion from B_c^+ decay has a longer lifetime and a higher P_T spectrum than the kaon from $B_u^+ \rightarrow J/\psi K^+$. Therefore, the decay-in-flight correction is the same as the correction for kaon decay that is used for the Cabibbo-suppressed B_u^+ decay. $\mathcal{D}_{\text{rel}} = 1.035 \pm 0.006$.

8.12 Limit Determination

The background has been estimated to be 51 ± 2 for the zero-lifetime B_c^+ and 9.2 ± 2.0 for the long-lived B_c^+ . The number of $J/\psi K^+$ events is 564 ± 26 . The relative efficiency is 0.746 ± 0.003 for the long-lived B_c^+ and 0.236 ± 0.002 for the zero-lifetime B_c^+ . The decay-in-flight correction is 1.035 ± 0.006 . We solve equation 8.28 numerically for the above values for a four bin region with 15 events for the long-lived B_c^+ and 55 events for the zero-lifetime B_c^+ . We determine an upper limit of

$$r = \frac{\sigma(B_c^+) \cdot \mathcal{B}(B_c^+ \rightarrow J/\psi \pi^+)}{\sigma(B_u^+) \cdot \mathcal{B}(B_u^+ \rightarrow J/\psi K^+)} < 0.034 \quad (8.47)$$

for the long-lived assumption and

$$r = \frac{\sigma(B_c^+) \cdot \mathcal{B}(B_c^+ \rightarrow J/\psi \pi^+)}{\sigma(B_u^+) \cdot \mathcal{B}(B_u^+ \rightarrow J/\psi K^+)} < 0.14 \quad (8.48)$$

for the zero-lifetime hypothesis.

We then use equation 8.43 to plot both limits as a function of lifetime in Figure 8.9.

The relative efficiency is computed as a function of lifetime and is used to compute the limit as a function of lifetime. We also superimpose the theoretical expectation based on the assumption that the B_c^+ is produced 1.5×10^{-3} [20] times as often as all other B mesons and that the partial width $\Gamma(B_c^+ \rightarrow J/\psi\pi^+) = 4.2 \times 10^9 \text{ s}^{-1}$ [36].

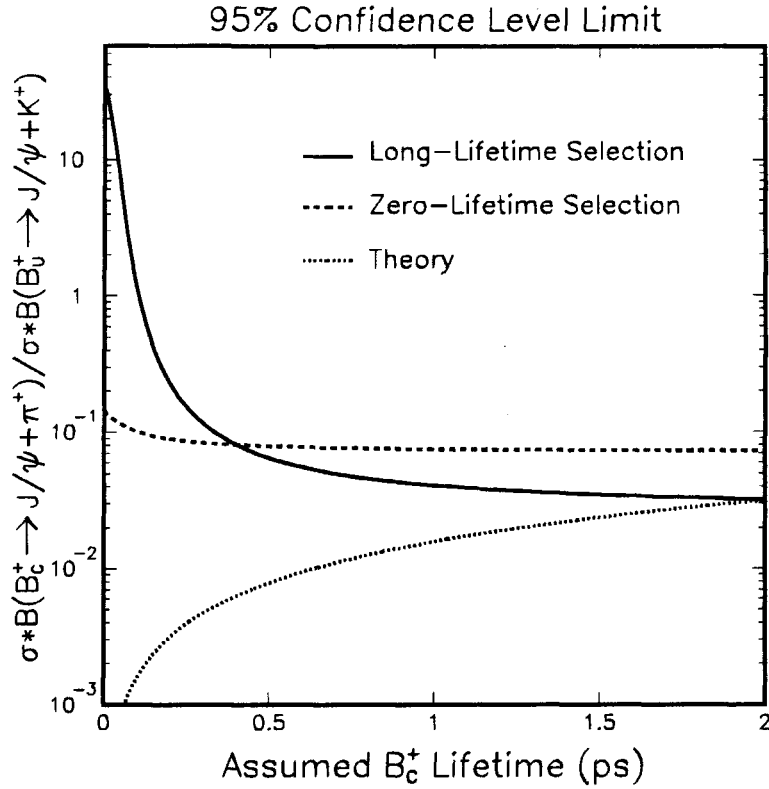


Figure 8.9: The figure shows the 95% confidence level limit on the ratio of cross section multiplied by branching ratio for the $B_c^+ \rightarrow J/\psi\pi^+$ and $B_u^+ \rightarrow J/\psi K^+$ decay modes. The theory curve assumes that the B_c^+ is produced 1.5×10^{-3} times as often as all other B mesons and that $\Gamma(B_c^+ \rightarrow J/\psi\pi^+) = 4.2 \times 10^9 \text{ s}^{-1}$.

Chapter 9

Systematics

The determination of the systematic error for the ratio of branching ratios and the ratio of cross section times branching ratio is accomplished by estimating the systematic error for each of the three terms. The following sections describe the possible systematic uncertainties for each term and estimate their magnitude.

9.1 Systematics on r_{obs}

9.1.1 Cabibbo-suppressed Analysis

The fitting procedure has been shown to correctly reproduce the data for Monte Carlo events (see Section 7.5). There are two primary sources of systematic error on r_{obs} . One source is due to incorrectly parameterizing the background. The other originates from incorrectly determining the normalization correction term in the likelihood.

The first systematic is due to incorrectly modeling the background with only a linear term. This effect is believed to be small. However, we will show below the

Parameter	Value
f_s	0.62 ± 0.02
r_{obs}	$0.051^{+0.018}_{-0.017}$
M_{B^+}	5.2780 ± 0.0006
k_σ	1.23 ± 0.06
a	0.9 ± 0.2
m	-13 ± 22

Table 9.1: The table displays the results of refitting the data with a parabolic background term.

effect of this by refitting the data with a parabolic background term and taking the difference in the ratio of branching ratios as a systematic. The new background term is

$$Y_{\text{bkg}} = a \left(M_{J/\psi K^+}^2 - \frac{(up^3 - ll^3)}{3(up - ll)} \right) + m \left(M_{J/\psi K^+} - \frac{(up + ll)}{2} \right) + \frac{1}{up - ll}. \quad (9.1)$$

The results of the fit are shown in Table 9.1.

The ratio of branching ratios differs by less than 0.001 out of 0.051, for approximately a 0.8% effect.

The second systematic is due to incorrectly estimating the ratio of the mass uncertainties, $\frac{dM_{\psi\pi^+}}{dM_{\psi K^+}}$. This effect was simulated in the Monte Carlo by multiplying the

correct ratio by a scale factor, k . The Monte Carlo data samples are prepared as prescribed by the fit. Table 9.2 shows the effect of varying k .

We estimate the systematic due to incorrectly calculating the ratio of mass uncertainties by comparing the ratio of mass errors to the expected calculated value, based on the momentum and decay angle. We find that the data tends to be lower, on average, by 0.7%. This gives a systematic of 1.6%, which we will treat as symmetric. Overall, the systematic in fitting is determined by adding the separate errors in quadrature. This gives a final uncertainty of 1.8%.

9.1.2 B_c^+ Search

The parameterization of the background has a small effect on the calculated limit. We estimate the effect of incorrectly parameterizing the background by fitting it to the second order polynomial of equation 9.1 instead of a line. We take the difference as the systematic.

For the long-lived B_c^+ , we estimate that the background has a 0.1 event uncertainty due to shape parameterization. Similarly, the zero-lifetime B_c^+ has a 0.2 event uncertainty. These uncertainties are small compared with the statistical uncertainty.

<i>k</i>	% difference
0.95	-13
0.96	-12
0.97	-7.3
0.98	-4.9
0.99	-2.5
1.00	0.0
1.01	2.4
1.02	4.7
1.03	7.0
1.04	9.3
1.05	12

Table 9.2: The table shows the effect of incorrectly estimating the ratio of errors between $J/\psi\pi^+$ and $J/\psi K^+$. The scale factor k multiplies the ratio of errors.

9.2 Systematics on ϵ_{rel}

9.2.1 Cabibbo-suppressed Analysis

We expect the systematic error on ϵ_{rel} to be small. However, for completeness, we consider the major source of systematic error for the relative efficiency measurement. This systematic error is due to incorrectly modeling the $P_T(B_u^+)$ -spectrum.

The relative efficiency was measured over 1 GeV/c intervals in Table 7.3. These events pass the cuts determined in Section 6.2. From the table we estimate the systematic error by varying the percentage of B mesons passing the cuts by 50% and then rescaling the rest of the spectrum. In addition, we group the efficiencies in 3-bin groups and vary the spectrum by 30%, again rescaling the remainder. We estimate our systematic from this variation to be 0.0016 for Run 1a and 0.0015 for Run 1b, which gives us the relative efficiencies of

$$\epsilon_{\text{rel}}(1a) = 1.002 \pm 0.004(\text{stat}) \pm 0.002(\text{syst}) \quad (9.2)$$

and

$$\epsilon_{\text{rel}}(1b) = 0.996 \pm 0.002(\text{stat}) \pm 0.003(\text{syst}). \quad (9.3)$$

Combining the two efficiencies we come up with an overall efficiency of

$$\epsilon_{\text{rel}} = 0.997 \pm 0.002 \pm 0.003. \quad (9.4)$$

This gives a systematic of 0.3%.

9.2.2 B_c^+ Search

The systematic uncertainty on the relative efficiency is due to uncertainties in the shape of the $P_T(B)$ -spectrum of the B_c^+ and B_u^+ . Unlike the Cabibbo-suppressed case, the relative efficiency is dependent on the $P_T(B)$ -spectrum. We estimate the magnitude of the uncertainty by separately considering that the largest bin for each spectrum is off by 30%. This gives a systematic of 0.07 for the long-lived case and 0.03 for the zero-lifetime case.

$$\epsilon_{\text{rel}}(\text{long-lived}) = 0.746 \pm 0.003 \pm 0.07 \quad (9.5)$$

$$\epsilon_{\text{rel}}(\text{short-lived}) = 0.236 \pm 0.002 \pm 0.03 \quad (9.6)$$

9.3 Systematics on \mathcal{D} , the decay-in-flight correction

There are two major contributions to the systematic errors on \mathcal{D} . Incorrectly modeling the $P_T(K^+)$, $P_T(\pi^+)$ distributions would give an inaccurate result. In addition, luminosity effects in track reconstruction must be considered.

Inaccurate $P_T(K^+)$, $P_T(\pi^+)$ distributions would result from inaccurate $P_T(B_u^+)$ distributions. Table 7.5 shows the decay-in-flight correction for 1 GeV/ c $P_T(B_u^+)$

Run #	$\bar{\mathcal{L}} (10^{30})$	$\int \mathcal{L} dt (nb^{-1})$	\mathcal{D}
56121	2.85	20.5	1.05 ± 0.02
60705	4.35	62.1	1.04 ± 0.01
62865	7.73	82.4	1.00 ± 0.01
65697	10.1	54.2	1.01 ± 0.01

Table 9.3: The table displays the data runs used to determine the decay-in-flight correction. The average luminosity during the run, $\bar{\mathcal{L}}$, and the integrated luminosity, $\int \mathcal{L} dt$, are given. The last column shows the decay-in-flight correction for each run.

ranges. We estimate a systematic of 0.005 from this. We also note that the contribution to the correction from pion decays in the B_c^+ analysis is negligible.

The effect of varying average luminosity over the course of the run could affect our ability to reconstruct tracks that decayed inside of the CTC. This effect is considered by breaking the decay-in-flight correction into separate runs with different average luminosities. This was done in Table 9.3. From this we estimate a systematic error of 0.012, or 1.2%.

9.4 Total Systematic

The total systematic error is determined by adding the error on the three terms in quadrature. Table 9.4 summarizes the errors.

For the Cabibbo-suppressed case, the overall systematic error is 2.2% of the mea-

Term	Cabibbo-Suppressed Syst. Err.	B_c^+ Search Syst. Err.
r_{obs}	1.8	1.1
ϵ_{rel}	0.3	9–13
\mathcal{D}	1.2	1.2
Total	2.2	9–13

Table 9.4: The table summarizes the systematic errors on the measurement of the ratio of branching ratios for B_u^+ .

surement. This gives a measurement of the ratio of branching ratios of

$$\frac{\mathcal{B}(B_u^+ \rightarrow J/\psi \pi^+)}{\mathcal{B}(B_u^+ \rightarrow J/\psi K^+)} = (5.0^{+1.9}_{-1.7} \pm 0.1)\%. \quad (9.7)$$

The systematic uncertainty is 9% for long-lived B_c^+ mesons and 13% for zero-lifetime B_c^+ mesons.

9.5 Recalculation of the B_c^+ Limit

The systematic errors associated with the B_c^+ meson's efficiencies and background affect the calculation of the limit. We determine the limit again, considering the systematic errors. For the long-lived case, there are 55 total events in the four highest bins with a background of $51 \pm 2 \pm 0.2$. The relative efficiency is $0.746 \pm 0.003 \pm 0.07$ and the decay-in-flight correction is $1.035 \pm 0.006 \pm 0.012$. Based on these numbers,

we calculate the 95% confidence level limit to be

$$r = \frac{\sigma(B_c^+) \cdot \mathcal{B}(B_c^+ \rightarrow J/\psi\pi^+)}{\sigma(B_u^+) \cdot \mathcal{B}(B_u^+ \rightarrow J/\psi K^+)} < 0.035. \quad (9.8)$$

For the zero-lifetime B_c^+ case, there are 15 total events in the four highest bins with a background of $9.2 \pm 2.0 \pm 0.1$. The relative efficiency is $0.236 \pm 0.002 \pm 0.03$ and the decay-in-flight correction is $1.035 \pm 0.006 \pm 0.012$. Based on these numbers, we calculate the 95% confidence level limit to be

$$r = \frac{\sigma(B_c^+) \cdot \mathcal{B}(B_c^+ \rightarrow J/\psi\pi^+)}{\sigma(B_u^+) \cdot \mathcal{B}(B_u^+ \rightarrow J/\psi K^+)} < 0.015. \quad (9.9)$$

We then use equation 8.43 to plot both limits as a function of lifetime in Figure 9.1. The relative efficiency is computed as a function of lifetime and is used to compute the limit as a function of lifetime.

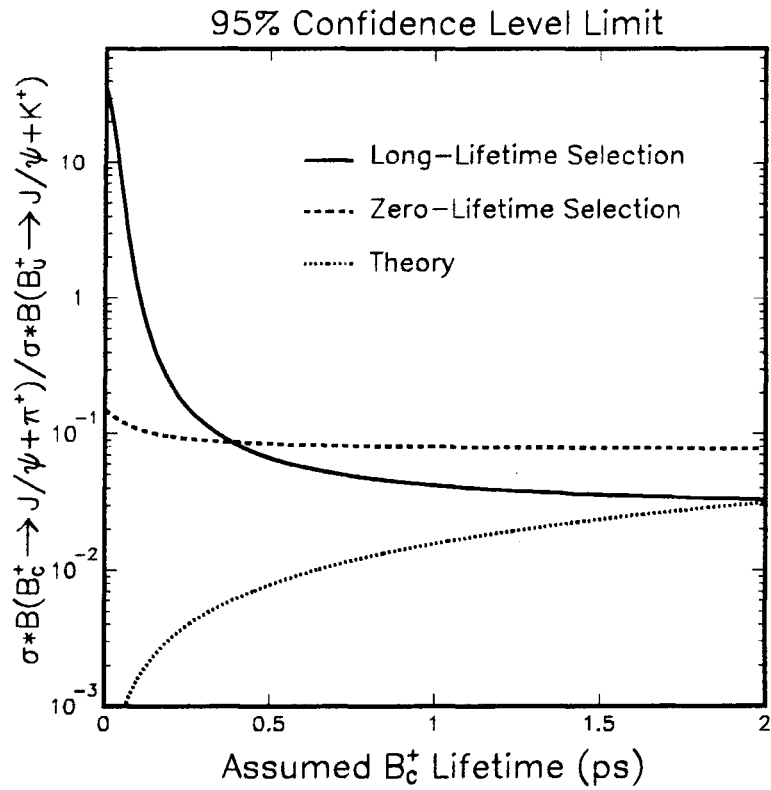


Figure 9.1: The figure shows the 95% confidence level limit on the ratio of cross section multiplied by branching ratio for the $B_c^+ \rightarrow J/\psi\pi^+$ and $B_u^+ \rightarrow J/\psi K^+$ decay modes. The theory curve assumes that the B_c^+ is produced 1.5×10^{-3} times as often as all other B mesons and that $\Gamma(B_c^+ \rightarrow J/\psi\pi^+) = 4.2 \times 10^9 \text{ s}^{-1}$.

Chapter 10

Conclusions

This thesis reports on the measurement of the ratio of branching ratios for the Cabibbo-suppressed decay mode $B_u^+ \rightarrow J/\psi\pi^+$. This is the first Cabibbo-suppressed $B \rightarrow J/\psi X$ mode that has been reconstructed and was first reported by the CLEO Collaboration based on 4.2 signal events[18]. We confirm their result with a larger sample of 28^{+10}_{-9} signal events, which is presently the world's largest sample of Cabibbo-suppressed B_u^+ decays. We use this signal to determine the ratio of branching ratios for the Cabibbo-suppressed to the Cabibbo-favored ($B_u^+ \rightarrow J/\psi K^+$) mode. The similarity of these modes reduces systematics to only 2.2% of the measured ratio. We report a ratio of

$$\frac{\mathcal{B}(B_u^+ \rightarrow J/\psi\pi^+)}{\mathcal{B}(B_u^+ \rightarrow J/\psi K^+)} = (5.0^{+1.9}_{-1.7} \pm 0.1)\%. \quad (10.1)$$

This result is consistent with the result presented by CLEO[18], $\frac{\mathcal{B}(B_u^+ \rightarrow J/\psi\pi^+)}{\mathcal{B}(B_u^+ \rightarrow J/\psi K^+)} = (4.3 \pm 2.3)\%$.

We use the world average value for $\mathcal{B}(B_u^+ \rightarrow J/\psi K^+) = (1.01 \pm 0.014) \times 10^{-3}$ [14] to obtain the Cabibbo-suppressed branching ratio

$$\mathcal{B}(B_u^+ \rightarrow J/\psi \pi^+) = (5.0_{-1.9}^{+2.1}) \times 10^{-5}. \quad (10.2)$$

This result is consistent with theoretical predictions.

We also search for $B_c^+ \rightarrow J/\psi \pi^+$. The search did not yield a definitive signal. Consequently, we set a limit on the ratio of cross section times branching ratio for the $B_c^+ \rightarrow J/\psi \pi^+$ and $B_u^+ \rightarrow J/\psi K^+$ decay modes. This ratio reduces some of the systematic uncertainties. We determined the 95% confidence level limit on this ratio as a function of lifetime, as shown in Figure 8.9. We find the limit to be 0.035 if the B_c^+ has lifetime equal to the B_u^+ meson's and 0.15 for zero-lifetime B_c^+ mesons. This result is also consistent with theory, since we expect a ratio of $\sim 5.0\% \times \frac{1}{7} = 0.7\%$ because the B_c^+ yield is suppressed by $\sim \frac{1}{7}$ (See equation 1.27) compared with the Cabibbo-suppressed yield (5.0%).

There are great prospects for these two modes during the Tevatron's Run II. With $\sim 2 \text{ fb}^{-1}$ of data, there will be approximately 600 $B_u^+ \rightarrow J/\psi \pi^+$ events. This gives a sensitivity to CP violation in this mode of $\sigma = \frac{1}{\sqrt{600}} = 4\%$, where σ is the uncertainty of charge asymmetry. In addition, the limit on $B_c^+ \rightarrow J/\psi \pi^+$ will be reduced by a factor of ~ 20 and may be observable if the lifetime of the B_c^+ is $\geq 0.5 \text{ ps}$. These modes will be aggressively pursued during Run II.

Appendix A

Decay-in-Flight Correction Limits

The decay-in-flight correction accounts for the relative efficiency of reconstructing an event for which the track (either π^+ or K^+) decays inside of the tracking chamber.

$$\mathcal{D} = \frac{\epsilon_{\text{dif}}^{J/\psi\pi}}{\epsilon_{\text{dif}}^{J/\psi K}} \quad (\text{A.1})$$

In this appendix we wish to determine the limits of this correction given the constraints of our cuts and detector. Since the kaon has a shorter lifetime than the pion, it will decay more frequently inside the detector. In addition, the kaon tends to have greater phase space for its daughter particles, which causes greater “kinks” in the track. A “kink” is a sharp turn in the track. The pion is only slightly heavier than its primary massive daughter, the μ^+ . Therefore, the “kink” is less severe, allowing for better track reconstruction after the decay. The scenario that allows the largest correction factor is when all kaons that decay within the chamber are lost and all pions are found. In addition, all the particles would just barely pass the cuts and exit

the detector at the boundary of the endplate and sidewall.

The fraction of particles that decay within rest frame time t of production is

$$\text{fraction decaying} = \frac{1}{\tau} \int_0^t e^{-\frac{t'}{\tau}} dt' = 1 - e^{-\frac{t}{\tau}}. \quad (\text{A.2})$$

The time to get to the edge of the detector, in the particle's rest frame, is

$$t = \frac{d}{c\beta\gamma}, \quad (\text{A.3})$$

where d is the path length of the particle.

This leads to the fraction decaying depending on the path length, lifetime and boost.

$$\text{fraction decaying} = 1 - \exp\left(-\frac{d}{c\beta\gamma}\right) \quad (\text{A.4})$$

Ignoring the Z_0 and D_0 components of the helix, it can be parameterized based on Figure A.1 as follows:

$$x_0 = -r \sin \phi_0 \quad (\text{A.5})$$

$$y_0 = r \cos \phi_0. \quad (\text{A.6})$$

If we parameterize the change in angle as u , we determine the x and y positions as

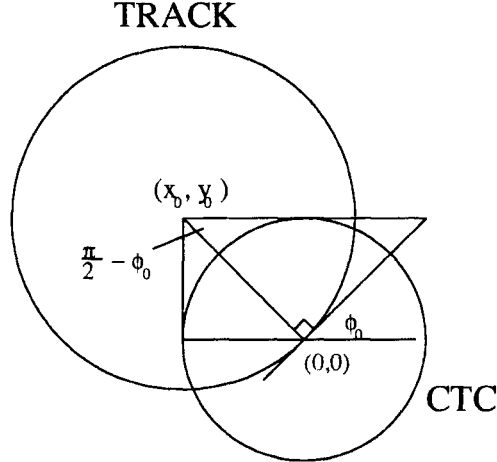


Figure A.1: The figure shows the two-dimensional view of a track's intersection with the CTC.

$$x = x_0 + r \cos \gamma = -r \sin \phi_0 + r \cos(u + \phi_0 - \frac{\pi}{2}) = r [-\sin \phi_0 + \sin(u + \phi_0)], \quad (\text{A.7})$$

$$y = y_0 + r \sin \gamma = r \cos \phi_0 + r \sin(u + \phi_0 - \frac{\pi}{2}) = r [\cos \phi_0 - \cos(u + \phi_0)]. \quad (\text{A.8})$$

To parameterize z , we use the relation

$$z = u \frac{dz}{du} = ur \cot \theta \quad (\text{A.9})$$

since

$$rdu = \tan \theta dz, \quad (\text{A.10})$$

giving

$$\frac{dz}{du} = r \cot \theta. \quad (\text{A.11})$$

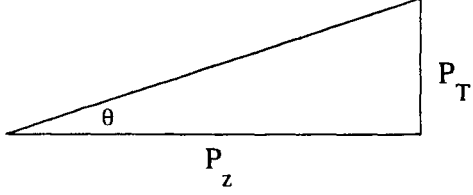


Figure A.2: The figure shows the $x - z$ plane. The angle θ relates P_Z to P_T .

For a particle leaving through the end plate of the detector, u covers an interval $(0, \frac{Z_{\max} \tan \theta}{r})$. To exit at the boundary of the endplate and the sidewall,

$$r_{\text{det}} = \sqrt{x^2 + y^2} = r[(\sin \phi_0 - \sin(u + \phi_0))^2 + (\cos \phi_0 - \cos(u + \phi_0))^2] = 2r \sin \frac{u}{2}, \quad (\text{A.12})$$

where r_{det} is the radius of the tracking chamber. This gives

$$u = 2 \sin^{-1} \frac{r_{\text{det}}}{2r} = \frac{Z_{\max} \tan \theta}{r}. \quad (\text{A.13})$$

This gives us a formula for $\tan \theta$.

$$\tan \theta = \frac{2r}{Z_{\max}} \sin^{-1} \frac{r_{\text{det}}}{2r} \quad (\text{A.14})$$

For a 1.25 GeV/ c particle, the radius in a 1.41 T magnetic field is

$$r = 296 \text{ cm}. \quad (\text{A.15})$$

The detector has a length of $Z_{\max} = 150$ cm and a radius of $r_{\text{det}} = 132$ cm. We solve for $\tan \theta$ to find

$$\tan \theta = \frac{2(296)}{150} \sin^{-1} \frac{132}{2(296)} = 0.89. \quad (\text{A.16})$$

We calculate the path length, d , as follows

$$d = \int_{u=0}^{u=\frac{Z_{\max} \tan \theta}{r}} \left[\left(\frac{dx}{du} \right)^2 + \left(\frac{dy}{du} \right)^2 + \left(\frac{dz}{du} \right)^2 \right]^{\frac{1}{2}} du \quad (\text{A.17})$$

where

$$\frac{dx}{du} = r \cos(u + \phi_0), \quad (\text{A.18})$$

$$\frac{dy}{du} = r \sin(u + \phi_0) \quad (\text{A.19})$$

and

$$\frac{dz}{du} = r \cot \theta. \quad (\text{A.20})$$

Substituting into equation A.17, we get

$$d = \int_{u=0}^{u=\frac{Z_{\max} \tan \theta}{r}} r \left[1 + \cot^2 \theta \right]^{\frac{1}{2}} du = \frac{r \csc \theta Z_{\max} \tan \theta}{r} = Z_{\max} \sec \theta. \quad (\text{A.21})$$

This gives the fraction decaying to be

$$\text{fraction decaying} = 1 - \exp \left[-\frac{Z_{\max} \sec \theta}{c \tau \beta \gamma} \right]. \quad (\text{A.22})$$

Since

$$\sec \theta = \frac{\sqrt{P_T^2 + P_Z^2}}{P_z} = \frac{M\beta\gamma c}{P_z}, \quad (\text{A.23})$$

we get

$$\text{fraction decaying} = 1 - \exp \left[-\frac{Z_{\max} Mc}{c\tau P_z} \right]. \quad (\text{A.24})$$

We calculate P_z from

$$P_z = P_T \cot \theta = \frac{1.25 \text{GeV}/c}{0.89} = 1.40 \text{GeV}/c. \quad (\text{A.25})$$

For $Z_{\max} = 150$ cm and the known kaon mass and lifetime of

$$c\tau = 370.9 \text{ cm},$$

$$Mc = 0.494 \text{ GeV}/c, \quad (\text{A.26})$$

we determine

$$\text{fraction decaying} = 1 - e^{-0.14} = 0.13. \quad (\text{A.27})$$

This gives a maximum decay-in-flight correction, \mathcal{D} , of

$$\mathcal{D} = \frac{1}{1 - 0.13} = 1.15. \quad (\text{A.28})$$

Therefore, \mathcal{D} is limited as follows

$$1 \leq \mathcal{D} \leq 1.15. \quad (\text{A.29})$$

Appendix B

Asymmetric Fitting

In order to test the correctness of the fitting procedure, a large number of Monte Carlo samples were produced and fit. The parameters that were returned by the fitting procedure were saved to do an overall fit for comparison with the input values. The evaluation of the ratio of branching ratios required a more sophisticated fit than the standard Gaussian due to significant asymmetries in the errors. The derivation of the fitting function is shown below.

Figure B.1 shows a likelihood function that is asymmetric near its maximum. If the log-likelihood, l , is expanded near the maximum, x_{\max} , we get

$$l(x) = l(x_{\max}) + \frac{d^2l}{dx^2} \frac{\rho^2}{2!} + \frac{d^3l}{dx^3} \frac{\rho^3}{3!} + \dots \quad (\text{B.1})$$

where $\rho = x - x_{\max}$ and $\frac{dl}{dx} = 0$.

For ρ very small, we get

$$l(x) = l(x_{\max}) + \frac{d^2 l}{dx^2} \frac{\rho^2}{2!}. \quad (\text{B.2})$$

If we compare

$$\begin{aligned} \mathcal{L} &= e^l = \exp \left[l_{\max} + \frac{d^2 l}{dx^2} \frac{\rho^2}{2!} \right] \\ &= e^{l_{\max}} \exp \left[\frac{d^2 l}{dx^2} \frac{\rho^2}{2!} \right] \end{aligned} \quad (\text{B.3})$$

with

$$\mathcal{L} = \frac{1}{\sqrt{2\pi}\sigma} e^{-\frac{\rho^2}{2\sigma^2}}, \quad (\text{B.4})$$

we find

$$\frac{d^2 l}{dx^2} = \frac{1}{\sigma^2}, \quad (\text{B.5})$$

which is just the reciprocal of the variance, which is the square of the symmetric error.

For larger ρ , we find

$$l = l_{\max} - \frac{1}{2\sigma^2} \rho^2 + \frac{d^3 l}{dx^3} \frac{\rho^3}{3!} + \frac{d^4 l}{dx^4} \frac{\rho^4}{4!}. \quad (\text{B.6})$$

For convenience, we substitute

$$a_3 = \frac{d^3 l}{dx^3}, a_4 = \frac{d^4 l}{dx^4}. \quad (\text{B.7})$$

The asymmetric errors, ρ_1 and ρ_2 , are the values of ρ that reduce l by $\frac{1}{2}$ from its maximum.

$$l(\rho_1) = l_{\max} - \frac{1}{2}, \quad (\text{B.8})$$

which gives

$$a_3 \left(\frac{\rho_1^3}{3!} \right) + a_4 \left(\frac{\rho_1^4}{4!} \right) + \left(\frac{1}{2} - \frac{\rho_1^2}{2\sigma^2} \right) = 0. \quad (\text{B.9})$$

Similarly,

$$a_3 \left(\frac{\rho_2^3}{3!} \right) + a_4 \left(\frac{\rho_2^4}{4!} \right) + \left(\frac{1}{2} - \frac{\rho_2^2}{2\sigma^2} \right) = 0. \quad (\text{B.10})$$

Solving for a_3 and a_4 , we find

$$a_3 = \frac{-3(\rho_1 + \rho_2)}{\rho_1^3 \rho_2^3 \sigma^2} \left[\sigma^2 (\rho_1^2 + \rho_2^2) - \rho_1^2 \rho_2^2 \right] \quad (\text{B.11})$$

and

$$a_4 = \frac{12}{\rho_1^3 \rho_2^3 \sigma^2} \left[\sigma^2 (\rho_1^2 + \rho_1 \rho_2 + \rho_2^2) - \rho_1^2 \rho_2^2 \right]. \quad (\text{B.12})$$

For a symmetric function with $\rho_1 = -\rho_2 = \sigma$,

$$a_3 = a_4 = 0. \quad (\text{B.13})$$

We have now established the form of our likelihood function. Numerical integration is used to normalize each term in

$$\mathcal{L}_i = A_i e^{l_i} = A_i \exp\left(-\frac{1}{2\sigma^2}\rho^2 + a_3 \frac{\rho^3}{3!} + a_4 \frac{\rho^4}{4!}\right) \quad (\text{B.14})$$

so that

$$\int \mathcal{L}_i d\rho = 1. \quad (\text{B.15})$$

The best value of the parameter is then found by maximizing the joint likelihood for all events.

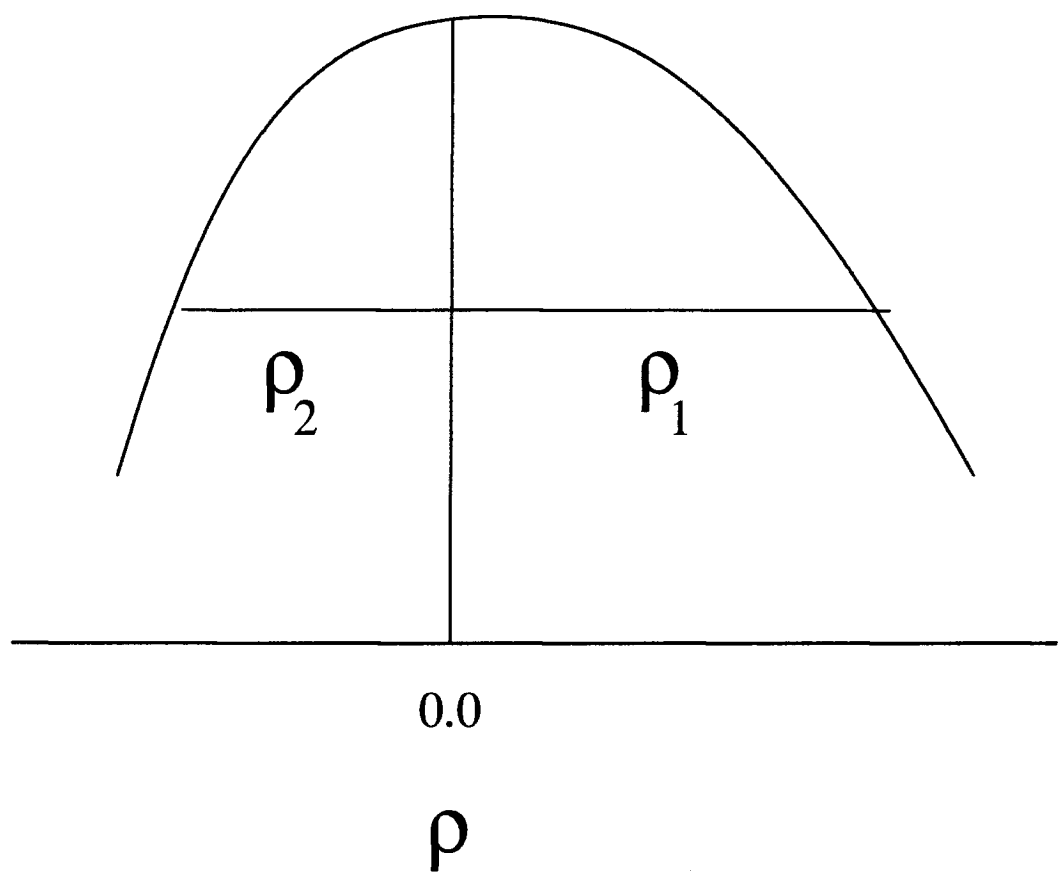


Figure B.1: The figure shows the asymmetric likelihood function for a measurement.

Appendix C

$\frac{dM_{J/\psi\pi^+}}{dM_{J/\psi K^+}}$ Determination

For $B_u^+ \rightarrow J/\psi\pi^+$ events, three variables determine the mass transformation from $M_{J/\psi\pi^+}$ to $M_{J/\psi K^+}$. We choose one set of variables which describe the transformation: $M_{J/\psi\pi^+}$, θ and β , where $M_{J/\psi\pi^+}$ is the measured invariant mass of the J/ψ and π^+ , θ is the measured polar angle between the J/ψ meson's momentum in the B meson's rest frame and the B meson's momentum in the lab frame and β is the measured relativistic boost of the B meson.

If we fix θ and β , $M_{J/\psi\pi^+}$ will be distributed as a Gaussian around $M_{B_u^+}$ with uncertainty σ_{π^+} .

If we define function F to transform $M_{J/\psi\pi^+}$ to $M_{J/\psi K^+}$, we find

$$M_{J/\psi K^+} = F(M_{J/\psi\pi^+}, \theta, \beta). \quad (\text{C.1})$$

The central value of this transformation is given when $M_{J/\psi\pi^+} = M_{B_u^+}$ so that

$$\langle M_{J/\psi K^+} \rangle = F(M_{B_u^+}, \theta, \beta). \quad (\text{C.2})$$

For small deviations from $M_{B_u^+}$, $M_{J/\psi K^+}$ will also be Gaussian.

For an event with $M_{J/\psi\pi^+} = M_{B_u^+} + x\sigma_{\pi^+}$, we find

$$M_{J/\psi K^+} = F(M_{B_u^+} + x\sigma_{\pi^+}, \theta, \beta) \quad (\text{C.3})$$

$$= F(M_{B_u^+}, \theta, \beta) + x\sigma_{\pi^+} \frac{\partial F(M_{B_u^+}, \theta, \beta)}{\partial M_{J/\psi\pi^+}}. \quad (\text{C.4})$$

For a $J/\psi\pi^+$ event that is $x\sigma_\pi$ from the central mass, the $J/\psi K^+$ mass will be $x\sigma_K$ from its central value to conserve probability. We subtract equation C.2 from equation C.4 to find

$$M_{J/\psi K^+} - \langle M_{J/\psi K^+} \rangle = M_{J/\psi K^+} - F(M_{B_u^+}, \theta, \beta) = x\sigma_{\pi^+} \frac{\partial F(M_{B_u^+}, \theta, \beta)}{\partial M_{J/\psi\pi^+}} = x\sigma_K. \quad (\text{C.5})$$

We rearrange this to get

$$\frac{\sigma_{K^+}}{\sigma_{\pi^+}} = \frac{\partial F}{\partial M_{J/\psi\pi^+}} = \frac{\partial M_{J/\psi K^+}}{\partial M_{J/\psi\pi^+}}. \quad (\text{C.6})$$

Therefore,

$$\frac{dM_{J/\psi\pi^+}}{dM_{J/\psi K^+}} = \frac{\sigma_{\pi^+}}{\sigma_{K^+}}. \quad (\text{C.7})$$

Appendix D

Angular Correlation of π^+ and μ^+ from $B_c^+ \rightarrow J/\psi\pi^+$, $J/\psi \rightarrow \mu^+\mu^-$

We here calculate the expectation value of the square of the matrix element for $\bar{c}c$ -quark pair annihilation in a $|LM_L\rangle = |10\rangle$ spin state to $\mu^+\mu^-$. We are particularly interested in the angular distribution of the muons.

We start with equation 8.11

$$\mathcal{M}_{10} = \frac{4M_c g_e^2}{3(p_1 + p_2)^2} [\bar{u}(3)\gamma^3\nu(4)]. \quad (\text{D.1})$$

We square the matrix element

$$|\mathcal{M}_{10}|^2 = \frac{16M_c^2 g_e^4}{9(p_1 + p_2)^4} [\bar{u}(3)\gamma^3\nu(4)] [\bar{u}(3)\gamma^3\nu(4)]^*. \quad (\text{D.2})$$

We then average over spin states

$$\frac{1}{4} \sum |\mathcal{M}_{10}|^2 = \frac{4M_c^2 g_e^4}{9(p_1 + p_2)^4} Tr [\gamma^3(\not{p}_3 + M_\mu c)\bar{\gamma}^3(\not{p}_4 - M_\mu c)] \quad (\text{D.3})$$

$$= \frac{4M_c c g_e^4}{9(p_1 + p_2)^2} \{ Tr(\gamma^3 \not{p}_3 \gamma^3 \not{p}_4) + M_\mu c [Tr(\gamma^3 \not{p}_3 \gamma^3) + Tr(\gamma^3 \gamma^3 \not{p}_4)] - M_\mu^2 c^2 Tr(\gamma^3 \gamma^3) \}. \quad (\text{D.4})$$

$$\not{p}_3 = p^\mu \gamma_\mu = E_3 \begin{pmatrix} 1 & 0 \\ 0 & -1 \end{pmatrix} - P_3^x \begin{pmatrix} 0 & \sigma_1 \\ -\sigma_1 & 0 \end{pmatrix} - P_3^y \begin{pmatrix} 0 & \sigma_2 \\ -\sigma_2 & 0 \end{pmatrix} - P_3^z \begin{pmatrix} 0 & \sigma_3 \\ -\sigma_3 & 0 \end{pmatrix} \quad (\text{D.5})$$

$$= \begin{pmatrix} E_3 & 0 & -P_3^z & -P_3^x + iP_3^y \\ 0 & E_3 & -P_3^x - iP_3^y & P_z \\ P_3^z & P_3^x - iP_3^y & -E_3 & 0 \\ P_3^x + iP_3^y & -P_3^z & 0 & -E_3 \end{pmatrix} \quad (\text{D.6})$$

$$\gamma^3 \not{p}_3 = \begin{pmatrix} 0 & 0 & 1 & 0 \\ 0 & 0 & 0 & -1 \\ -1 & 0 & 0 & 0 \\ 0 & 1 & 0 & 0 \end{pmatrix} \begin{pmatrix} E_3 & 0 & -P_3^z & -P_3^x + iP_3^y \\ 0 & E_3 & -P_3^x - iP_3^y & P_3^z \\ P_3^z & P_3^x - iP_3^y & -E_3 & 0 \\ P_3^x + iP_3^y & -P_3^z & 0 & -E_3 \end{pmatrix} \quad (\text{D.7})$$

$$= \begin{pmatrix} P_3^z & P_3^x - iP_3^y & -E_3 & 0 \\ -P_3^x - iP_3^y & P_3^z & 0 & E_3 \\ -E_3 & 0 & P_3^z & P_3^x - iP_3^y \\ 0 & E_3 & -P_3^x - iP_3^y & P_3^z \end{pmatrix} \quad (\text{D.8})$$

$$\Omega = \gamma^3 \not{p}_3 \gamma^3 \not{p}_4 = \quad (\text{D.9})$$

$$\begin{pmatrix} P_3^z & P_3^x - iP_3^y & -E_3 & 0 \\ -P_3^x - iP_3^y & P_3^z & 0 & E_3 \\ -E_3 & 0 & P_3^z & P_3^x - iP_3^y \\ 0 & E_3 & -P_3^x - iP_3^y & P_3^z \end{pmatrix} \begin{pmatrix} P_4^z & P_4^x - iP_4^y & -E_4 & 0 \\ -P_4^x - iP_4^y & P_4^z & 0 & E_4 \\ -E_4 & 0 & P_4^z & P_4^x - iP_4^y \\ 0 & E_4 & -P_4^x - iP_4^y & P_4^z \end{pmatrix} \quad (\text{D.10})$$

Since we are only interested in the diagonal elements of matrix Ω , we shall list those elements below as $\Omega_{i,j}$ where i is the row index and j is the column index.

$$\Omega_{1,1} = P_3^z P_4^z - P_3^x P_4^x - P_3^y P_4^y - iP_3^x P_4^y + iP_3^y P_4^x + E_3 E_4 \quad (\text{D.11})$$

$$\Omega_{2,2} = -P_3^x P_4^x - P_3^y P_4^y + iP_3^x P_4^y - iP_3^y P_4^x + P_3^z P_4^z + E_3 E_4 \quad (\text{D.12})$$

$$\Omega_{3,3} = E_3 E_4 + P_3^z P_4^z - P_3^x P_4^x - P_3^y P_4^y - iP_3^x P_4^y + iP_3^y P_4^x \quad (\text{D.13})$$

$$\Omega_{4,4} = E_3 E_4 - P_3^x P_4^x - P_3^y P_4^y + iP_3^x P_4^y - iP_3^y P_4^x + P_3^z P_4^z \quad (\text{D.14})$$

Therefore,

$$Tr(\gamma^3 p_3 \gamma^3 p_4) = 4E_3 E_4 + 4P_3^z P_4^z - 4P_3^x P_4^x - 4P_3^y P_4^y = 4(p_3 \cdot p_4 + 2P_3^z P_4^z). \quad (\text{D.15})$$

The remaining terms are easily calculated.

$$Tr(\gamma^3 \gamma^3 p_4) = Tr(-p_4) = 0 \quad (\text{D.16})$$

$$Tr(\gamma^3 \gamma^3) = Tr(-1) = -4 \quad (\text{D.17})$$

Adding the terms, we get

$$\langle |\mathcal{M}_{10}|^2 \rangle = \frac{4M_c^2 g_e^4}{9(p_1 + p_2)^4} [4(p_3 \cdot p_4 + 2p_3^z p_4^z) + 4M_\mu^2 c^2] \quad (\text{D.18})$$

$$= \frac{16M_c^2 g_e^4}{9(p_1 + p_2)^4} [p_3 \cdot p_4 + 2p_3^z p_4^z + M_\mu^2 c^2]. \quad (\text{D.19})$$

Using for the four-vectors

$$p_3 = \begin{pmatrix} \sqrt{M_\mu^2 c^2 + p^2} \\ p \sin \theta \\ 0 \\ p \cos \theta \end{pmatrix}, p_4 = \begin{pmatrix} \sqrt{M_\mu^2 c^2 + p^2} \\ -p \sin \theta \\ 0 \\ -p \cos \theta \end{pmatrix}, \quad (\text{D.20})$$

where p is the magnitude of the μ^+ momentum in the J/ψ rest frame and θ is the angle between the μ^+ and the \hat{z} -axis, we find

$$p_3 \cdot p_4 = M_\mu^2 + 2p^2, \quad (\text{D.21})$$

$$p_3^z p_4^z = -p^2 \cos \theta. \quad (\text{D.22})$$

$$\langle |\mathcal{M}_{10}|^2 \rangle = \frac{32M_c^2 g_e^4}{9(p_1 + p_2)^4} [M_\mu^2 c^2 + p^2(1 - \cos^2 \theta)] = \frac{32M_c^2 g_e^4}{9(p_1 + p_2)^4} [M_\mu^2 c^2 + p^2 \sin^2 \theta] \quad (\text{D.23})$$

$$\frac{d\Gamma}{d\cos\theta} \propto M_\mu^2 c^2 + p^2 \sin^2\theta \approx p^2 \sin^2\theta \quad (\text{D.24})$$

Therefore, we use the approximation

$$\frac{d\Gamma}{d\cos\theta} \propto \sin^2\theta. \quad (\text{D.25})$$

Bibliography

- [1] S. W. Herb *et al.*, Phys. Rev. Lett. **39**, 252 (1977).
- [2] W. R. Innes *et al.*, Phys. Rev. Lett. **39**, 1240 (1977).
- [3] Ch. Berger *et al.*, Phys. Lett. B **76**, 243 (1978).
- [4] C. W. Darden *et al.*, Phys. Lett. B **76**, 246 (1978).
- [5] J. K. Bienlein *et al.*, Phys. Lett. B **78**, 360 (1978).
- [6] C. W. Darden *et al.*, Phys. Lett. B **78**, 364 (1978).
- [7] D. Andrews *et al.*, Phys. Rev. Lett. **44**, 1108 (1980).
- [8] T. Böhringer *et al.*, Phys. Rev. Lett. **44**, 1111 (1980).
- [9] S. Behrends, *et al.*, Phys. Rev. Lett. **50**, 881 (1983).
- [10] J. C. Collins and R. K. Ellis, Nucl. Phys. B **360**, 3 (1991).
- [11] N. Cabibbo, Phys. Rev. Lett. **10**, 531 (1963).
- [12] M. Kobayashi and T. Maskawa, Prog. Theor. Phys. **49**, 652 (1972).

- [13] L.-L. Chau and W.-Y. Keung, Phys. Rev. Lett. **53**, 1802 (1984).
- [14] *Particle Data Group*, R. M. Barnett *et al.*, Phys. Rev. D **54** (1996).
- [15] M. Gourdin, Y.Y. Keum, X.Y. Pham, Preprint PAR/LPTHE/95-01, (1995).
- [16] F. Hussain and M. D. Scandron, Phys. Rev. D **30**, 1492 (1984).
- [17] Deandrea *et al.*, Phys. Lett. B **318**, 549 (1993).
- [18] J. P. Alexander *et al.*, Phys. Lett. B **341**, 435 (1995).
- [19] E. Eichten and C. Quigg, Fermilab-PUB-94/032-T.
- [20] E. Braaten, K. Cheung and T. C. Yuan, Phys. Rev. D **48**, R5049 (1996).
- [21] C. Chang and Y. Chen, Phys. Rev. D **49**, 3399 (1994).
- [22] C. Quigg, Fermilab-Conf-93/265-T.
- [23] F. Abe *et al.*, Nucl. Instrum. Methods, A **271**, 387 (1988).
- [24] F. Abe *et al.*, Nucl. Instrum. Methods, A **268**, 50 (1988).
- [25] F. Abe *et al.*, Phys. Rev. Lett. **74**, 2626 (1995).
- [26] “SVX’, The New CDF Silicon Vertex Detector”, Fermilab-CONF-94/205-E (1994).

- [27] "The Silicon Vertex Detector of the Collider Detector at Fermilab", CDF/SEC_VTX/DOC/PUBLIC/2398 (1994).
- [28] F. Abe *et al.*, Nucl. Instrum. Methods, A **268**, 33 (1988).
- [29] F. Abe *et al.*, Nucl. Instrum. Methods, A **268**, 46 (1988).
- [30] J. Lewis and S. Pappas, CDF/ANAL/TRIGGER/CDFR/3070 (1995).
- [31] P. Nason, S. Dawson, and R. K. Ellis, Nucl. Phys. B **303**, 607 (1988); B **327**, 49 (1989); B **335**, 260 (1990).
- [32] P. Avery, K. Read, and G. Trahern, Report No. CSN-212, 1985 (unpublished).
- [33] J. Gonzalez, CDF/ANAL/BOTTOM/CDFR/3010
- [34] D. Griffiths, "Introduction to Elementary Particles," John Wiley & Sons, Inc., New York, (1987).
- [35] G. Zech, Nucl. Instrum. Methods A **277**, 608 (1989).
- [36] M. Lusignoli and M. Masetti, Z. Phys. C **51**, 549 (1991).